
**Πανεπιστήμιο Ιωαννίνων**

**Σχολή Επιστημών Υγείας**

**Τμήμα Ιατρικής**

Μορφολογικός- Κλινικοεργαστηριακός Τομέας

Εργαστήριο Ιατρικής Φυσικής


# Μικροδοσιμετρικοί υπολογισμοί σε επίπεδο DNA για τον καθορισμό ασφαλών ορίων ακτινικών δόσεων σε επανδρωμένες αποστολές μακράς διάρκειας στο διάστημα

# Microdosimetric calculations for the determination of safe radiation dose limits for manned long-term space missions


ΠΑΠΑΔΟΠΟΥΛΟΣ ΑΛΕΞΗΣ, MSc


**ΔΙΔΑΚΤΟΡΙΚΗ ΔΙΑΤΡΙΒΗ**


Ιωάννινα 2025


**Πανεπιστήμιο Ιωαννίνων**

**Σχολή Επιστημών Υγείας**

**Τμήμα Ιατρικής**

Μορφολογικός- Κλινικοεργαστηριακός Τομέας

Εργαστήριο Ιατρικής Φυσικής


# Μικροδοσιμετρικοί υπολογισμοί σε επίπεδο DNA για τον καθορισμό ασφαλών ορίων ακτινικών δόσεων σε επανδρωμένες αποστολές μακράς διάρκειας στο διάστημα

# Microdosimetric calculations for the determination of safe radiation dose limits for manned long-term space missions


ΠΑΠΑΔΟΠΟΥΛΟΣ ΑΛΕΞΗΣ, MSc


**ΔΙΔΑΚΤΟΡΙΚΗ ΔΙΑΤΡΙΒΗ**


Ιωάννινα 2025

*Η έγκριση της διδακτορικής διατριβής από το Τμήμα Ιατρικής του Πανεπιστημίου Ιωαννίνων δεν υποδηλώνει αποδοχή των γνωμών του συγγραφέα Ν. 5343/32, άρθρο 202, παράγραφος 2 (νομική κατοχύρωση του Ιατρικού Τμήματος).*

**Ημερομηνία αίτησης του κ. Παπαδόπουλου Αλέξιου:** 14-11-2020

**Ημερομηνία ορισμού Τριμελούς Συμβουλευτικής Επιτροπής**: Γ.Σ. αριθμ. 960α/21-04-2021

**Μέλη Τριμελούς Συμβουλευτικής Επιτροπής**:

Επιβλέπων:

Εμφιετζόγλου Δημήτριος, Καθηγητής Ιατρικής Φυσικής – Ακτινοφυσικής του Τμήματος Ιατρικής του Πανεπιστημίου Ιωαννίνων

Μέλη:

Δαγκλής Ιωάννης, Καθηγητής Διαστημικής Φυσικής του Τμήματος Φυσικής του ΕΚΠΑ

Incerti Sebastien, Research Director, CNRS Γαλλίας

**Ημερομηνία ορισμού θέματος**: Γ.Σ. αριθμ. 960α/21-04-2021

«Μικροδοσιμετρικοί υπολογισμοί σε επίπεδο DNA για τον καθορισμό ασφαλών ορίων ακτινικών δόσεων σε επανδρωμένες αποστολές μακράς διάρκειας στο διάστημα»

«Microdosimetric calculations for the determination of safe radiation dose limits for manned long-term space missions»

**ΟΡΙΣΜΟΣ ΕΠΤΑΜΕΛΟΥΣ ΕΞΕΤΑΣΤΙΚΗΣ ΕΠΙΤΡΟΠΗΣ: 1123α/24-10-2024**

1. Εμφιετζόγλου Δημήτριος, Καθηγητής Ιατρικής Φυσικής-Ακτινοφυσικής του Τμήματος Ιατρικής του Πανεπιστημίου Ιωαννίνων
2. Δαγκλής Ιωάννης, Καθηγητής Διαστημικής Φυσικής του Τμήματος Φυσικής του ΕΚΠΑ
3. Incerti Sebastien, Research Director, CNRS Γαλλίας
4. Αστρακάς Λουκάς, Αναπληρωτής Καθηγητής Ιατρικής Φυσικής του Τμήματος Ιατρικής του Πανεπιστημίου Ιωαννίνων
5. Κυριακού Ιωάννα, Επίκουρη Καθηγήτρια Ιατρικής Φυσικής με έμφαση στη Μικροδοσιμετρία του Τμήματος Ιατρικής του Πανεπιστημίου Ιωαννίνων
6. Κόκκας Παναγιώτης, Καθηγητής Φυσικής του Τμήματος Φυσικής του Πανεπιστημίου Ιωαννίνων
7. Γεωργακίλας Αλέξανδρος, Καθηγητής στη Σχολή Εφαρμοσμένων Μαθηματικών και Φυσικών Επιστημών (ΣΕΜΦΕ) του ΕΜΠ

Έγκριση Διδακτορικής Διατριβής με βαθμό **«ΑΡΙΣΤΑ»** στις **22-11-2024**

**Ιωάννινα 14-05-2025**

**ΠΡΟΕΔΡΟΣ ΤΟΥ ΤΜΗΜΑΤΟΣ ΙΑΤΡΙΚΗΣ**

**Σπυρίδων Κονιτσιώτης**

Καθηγητής Νευρολογίας

**Η Γραμματέας του Τμήματος**

**Αικατερίνη Λαγού**

## Acknowledgements

The acknowledgments will be written in my native language, Greek, to convey as much understandable meaning as possible to those they are addressed to.

Κατά τη διάρκεια αυτών των τριών χρόνων, η σκληρή δουλειά που αποτυπώνεται στα αποτελέσματα της παρούσας εργασίας συνοδεύεται από προσωπικές κατακτήσεις και στηρίζεται στη βοήθεια που έλαβα από σημαντικούς ανθρώπους. Για όλα τα παραπάνω, θα έχετε όλοι μια θέση στην καρδιά μου, να είστε σίγουροι.

Αρχικά, θα ήθελα να ευχαριστήσω τον μέντορα και επιβλέποντα καθηγητή μου, καθηγητή Δημήτριο Εμφιετζόγλου, ο οποίος από την πρώτη κιόλας μέρα με στήριξε και με πίστεψε τόσο σε προσωπικό όσο και σε επιστημονικό επίπεδο. Μου παρείχε απλόχερα και χωρίς να το ζητήσω τα κατάλληλα εφόδια, για να βελτιωθώ ως επιστήμονας και να αντιμετωπίσω τις ανησυχίες μου. Ένα μεγάλο και ετεροχρονισμένο ‘ευχαριστώ’ για όλες τις στιγμές που δεν το εξέφρασα, γιατί χωρίς τη βοήθειά του δε θα υπήρχε project!

Ακολούθως, θα ήθελα να ευχαριστήσω τον επιβλέποντα καθηγητή μου στο μεταπτυχιακό πρόγραμμα της Αστροφυσικής και μέλος της διδακτορικής μου επιτροπής, καθηγητή Διαστημικής Φυσικής και πρόεδρο του Ελληνικού Κέντρου Διαστήματος, καθηγητή Ιωάννη Α. Δαγκλή. Ο καθηγητής Δαγκλής με πίστεψε από τα χρόνια του μεταπτυχιακού μου και συνέχισε να μου δίνει το απαραίτητο κουράγιο κατά τη διάρκεια του διδακτορικού μου. Επίσης, θα ήθελα να ευχαριστήσω το τρίτο μέλος της επιτροπής μου, τον κ. Sebastien Incerti, για τις χρήσιμες συμβουλές του και την ενθάρυνση του, στην διεκπεραίωση του project.

Επιπλέον, θα ήθελα να ευχαριστήσω και να εκφράσω την εκτίμησή μου προς την κ. Ιωάννα Κυριακού, επίκουρη καθηγήτρια στο Εργαστήριο Ιατρικής Φυσικής, για την αδιάκοπη βοήθειά της -τις πολλές φορές που τη χρειαζόμουν-, καθώς και για το χαμόγελο και την ευγένειά της.

Ευχαριστώ όλα τα μέλη του εργαστηρίου, παλιούς και νέους, γι’ αυτά τα τρία χρόνια.

Τους γονείς μου, Δημήτρη και Μαρία, οι οποίοι νιώθουν περήφανοι για μένα, θα ήθελα να ξέρουν πόσο περήφανος νιώθω κι εγώ για εκείνους.

Ευχαριστώ τους φίλους μου, Στέφανο, Μανώλη, Αντρέα, Κωνσταντίνο, Φίλιππο, Σωτήρη, Χρήστο, Γιώργο, Δημήτρη, οπου και να βρίσκονται, οι οποίοι θα μου πούνε πάντα την αλήθεια!

Τελος, θα ήθελα να ευχαριστήσω τη ξεχωριστή Μαρίνα, για τις πιο όμορφες στιγμές μου. Είμαι σίγουρος ότι το μέλλον επιφυλάσσει ακόμη περισσότερες αγαπημένες στιγμές μαζί.

## Abbreviations

| Symbol | Quantity |
|---|---|
| D | absorbed dose |
| VA | Van Allen |
| GCR | galactic cosmic rays |
| SPE | solar particle events |
| HZE | high Z and energy |
| CVD | cardiovascular disease |
| CNS | central nervous system |
| DDREF | dose and dose rate reduction factor |
| LEO | low Earth orbit |
| RBE | relative biological effectiveness |
| Q | quality factor |
| BLEO | beyond low Earth orbit |
| DNA | deoxyribonucleic acid |
| LET | linear energy transfer |
| TEPC | tissue equivalent proportional counter |
| TDRA | theory of dual radiation action |
| MKM | microdosimetric kinetic model |
| ICRU | international commission on radiation units and measurements |
| ICRP | international commission on radiological protection |
| NASA | national aeronautics and space administration |

| | |
|---|---|
| MCTS | monte carlo track structure |
| CME | coronal mass ejection |
| SAA | south Atlantic anomaly |
| EVA | extravehicular activity |
| ISS | international space station |
| ALARA | as low as reasonably achievable |
| ESA | European space agency |
| JAXA | Japan aerospace exploration agency |
| RSA | Russian space agency |
| CSA | Canadian space agency |
| NCRP | national council on radiation protection and measurements |
| REID | radiation exposure induced death from cancer |
| CL | confidence level |
| NAS | national academies of sciences |
| MC | monte carlo |
| LSS | life span study |
| X94 | Xapsos 1994 model |
| X96 | Xapsos 1996 model |
| Xcom | Combined Xapsos model |
| XO | Xapsos-Olko combined model |
| PDF | probability density function |

| | |
|---|---|
| RPWBA | relativistic plane wave born approximation |
| DICS | differential ionization cross section |
| DRF | dielectric response function |
| ELF | energy loss function |
| RADS | radiation attributed decrease of survival |
| SP | stopping power |
| RD | relative difference |
| ERR | excess relative risk |
| EAR | excess additive risk |
| CDC | centers for disease control |
| REIC | risk of exposure induced-cancer |
| RR | relative risk |
| RERF | radiation research effects foundation |
| YLL | years life lost |

# LIST OF FIGURES

**Figure 13.** Integral Flux (particles/cm$^2$/day) of GCR particles from protons up to Fe, obtained from the OLTARIS platform for 1977 Solar Minimum conditions. Red line represents the integral flux in deep space (1 AU) and blue line the flux in LEO (ISS ~400 km), both for no shielding conditions.

**Figure 14.** Integral Flux (particles/cm$^2$/day) of GCR particles from protons up to Fe for deep space, obtained from the OLTARIS platform for 1977 Solar Minimum conditions. The calculations were made for no shielding conditions, 10, 20 and 30 g/cm$^2$. The embedded Figure represents the integral flux for Z=1-2 for different aluminium shielding.

**Figure 15.** Cumulative Q value of GCR as a function of particle's charge (Z) (dot-lines), calculated by TDRA for (a) LEO (ISS ~400 km) and (b) deep space (1 AU), both calculated behind aluminium shielding of 10-30g/cm$^2$. Thick, solid lines are the mission Q values.

**Figure 16.** Contribution (%) of different GCR particles to the total (mission) Q value calculated with the TDRA methodology for (a) LEO (ISS ~400 km) and (b) deep space (1 AU), both behind aluminium shielding of 10-30 g/cm$^2$.

**Figure 17.** Reduction (%) of the TDRA-based mission Q-value, with increasing aluminium shielding (5-40 g/cm$^2$) for LEO (ISS ~400 km) and deep space (1 AU).

**Figure 18.** Schematic representation of the direct and indirect events considered by the microdosimetric models.

**Figure 19.** Schematic representation of the method followed by the microdosimetric models for the indirect events.

**Figure 20.** Proton stopping power (SP) for liquid water for the energy range 1 MeV – 1 GeV calculated in the present work by the RPWBA and the dielectric theory (red line) and compared against the data from ICRU Report 90 (green line). The blue line represents the relative difference (%) of the SP values using the ICRU data as a baseline.

**Figure 21.** Left panel: Present work $\delta_2$ values for various proton energies (2, 5, 10, 20, 50, 100, 400, 600, 800, 1000 MeV) and distinct cut-off energies $\Delta$ corresponding to the three-sphere diameters (10, 100, 1000 nm) obtained from Eq. (23). Right Panel: $\delta_2$ values as a function of cut off energy $\Delta$, calculated by the approaches of Kellerer, Xapsos and present work.

**Figure 22.** Energy-loss straggling distributions (Log-Normal, Erlang, Logistic) studied in this work, for 1, 10, 100 and 1000 MeV proton and three diameter spheres 1000 (panel a), 100 (panel b) and 10 nm (panel c).

**Figure 23.** Dose-mean lineal energy ($y_D$) values for liquid water and various sphere diameters (10, 100, and 1000 nm) as a function of proton energy (1 MeV – 1 GeV), calculated by the microdosimetric models ("Present work" and Xapsos models), the MCTS codes (Geant4-DNA, PHITS-KURBUC, PHITS t-sed, and RITRACKS), and the MCDS. The LET values calculated from the ICRU Report 90 are also presented.

**Figure 24.** Relative difference (%) of the $y_D$ values of the analytic models and the MCDS algorithm against the mean $y_D$ of the MCTS codes for each proton energy (see Figure 6 and Eq. (33)).

**Figure 25.** Mean percentage deviation (MPD) calculated by Eq. (34) for each $y_D$ dataset. The mean $y_D$ of the MCTS codes is used as baseline in the calculation of the MPD.

**Figure 26.** Contribution (%) of the indirect part of the dose-mean lineal energy ($y_{D,ind}$) relative to the total $y_D$ (see Eq. 6) for the three energy straggling distributions (Erlang/Log-Normal and Logistic) examined in the presented microdosimetric model and the three sphere diameters (1000, 100, and 10 nm). The results for the Erlang and Log-Normal distributions are practically identical.

## LIST OF TABLES

## Contents

# Chapter 1

## Introduction

After 66 years since the initial discovery of the Van Allen belts and the acknowledgment of space as a radioactive environment, coupled with the passage of 52 years since the last Apollo mission to the moon, our understanding of the biological consequences of space radiation on the human body remains limited. Despite the prospect of manned space missions to the Moon, the establishment of a permanent lunar base, forthcoming Mars expeditions, and the concept of space tourism, astronauts, who are classified as radiation workers, will encounter distinct and continuous radiation. This exposure poses substantial risks, including the development of malignant tumours, acute radiation-induced health effects, and other late health consequences such as cataracts, brain cognitive damage, and cardiovascular diseases (2–9).

The space radiation environment is quite different from that encountered on the surface of Earth, which are mostly *X* and $\gamma$ rays and a small component of alpha particles from (mainly) radon. The space radiation field is composed of highly energetic ions of a wide range of atomic numbers. It includes the constant and isotropic Galactic Cosmic Rays (GCR), the sporadic Solar Particle Events (SPE), and the Van Allen belts (VA) in the Earth's magnetosphere.

GCR consists of a baryon (98%) and an electron component (2%). Baryons include protons (~ 85%), alpha particles (~ 14%) and high-atomic number, and high-energy Ions (HZE) up to uranium (~ 1%), with energies peaking around GeV/amu, while reaching up to ~TeV/amu and beyond (4,8,10,11). The most probable source of these particles are high-energy phenomena from supernova blast waves ($<10^{15}$eV) or even neutron stars (12). The solar cycle can affect space mission planning, by decreasing (at solar maximum) or increasing (at solar minimum) the absorbed doses from GCR that astronauts receive. The GCR effective dose rates in deep space, although ~ 1000 times greater than on Earth, are considered relatively low and do not cause acute health effects. As a result, the biological concerns from GCRs are mostly carcinogenesis and the degenerative late effects of specific tissues, such as cardiovascular disease (CVD), damage to the Central Nervous System (CNS), and the induction of cataracts (3,5,13–15). In LEO orbit (such as on the International Space Station, ISS), the effective dose rates from GCR are lower than in deep space by a factor of about 2, due to the additional shielding from the Earth's magnetic field, although this is dependent on the inclination and the altitude of the mission(2,5,9).

Given that radiation-induced fatal cancers are the predominant health concern for space agencies and astronauts due to GCR low dose irradiation, assessing cancer risk becomes challenging due to significant uncertainties in heavy ion radiobiology (quality factor issues), tissue cancer risk transfer models, dose and dose rate reduction factor (DDREF) and cross sections in radiation transportation through shielding(11,15–17). The greatest uncertainty for cancer risk evaluation arises from the biological effects of heavier nuclei (HZE) (and neutrons), as human data for such exposures are lacking. Consequently, calculating the relative biological effectiveness (RBE) or/and the quality factor (Q) for several biological endpoints and space ions remains an ongoing challenge. There is also a lack of consensus among different space agencies regarding cancer risk evaluation and career dose limits for astronauts(2,18,19). Until

recently, all missions were on Low-Earth Orbit (LEO), so the differences among the cancer risk assessment of space agencies did not pose any serious mission planning problem. However, in Beyond-LEO (BLEO) missions, the uncertainties are notable and must be taken into consideration.

The analysis and characterization of the microscopic distribution of energy deposition following the interaction of ionizing radiation with the irradiated medium is of significant importance in studying radiation effects for a wide range of applications, including cancer therapy, space radiation protection, as well as single-event errors in electronic devices(20–23). For radiation protection purposes, the radiation quality is commonly linked to the small-scale microdosimetric distributions which are distinct for each type (and energy) of radiation. The dependence of biological effects upon radiation quality is formally quantified via the Relative Biological Effectiveness (RBE)(24,25). For stochastic, mainly carcinogenetic effects, the RBE is synonymous with the quality factor (Q). Stochastic carcinogenic effects are considered a late effect in radiation therapy for the treatment of cancer, although the putative carcinogenic effects of radiation therapy are not usually considered treatment-limiting in most scenarios. In addition, for clinical endpoints, the Q, which is an indicator of late stochastic effects of concern for radiation protection, is not representative of the RBE for tumor control or adverse effects on normal tissue clinical endpoints.

Studies of the physical basis of Q were initially focused on micrometer-sized spherical volumes (diameter ~1–10 μm) representative of the cell, cell nucleus and critical chromosomal targets within the cell nucleus(21,22). Currently, there is an increased interest in energy deposition events at the nanometer-scale because of the correspondence to the dimensions of the diameter of the deoxyribonucleic acid (DNA) helix, the nucleosome, or sections of chromosomes. Energy deposition to such structures is believed to correlate with the RBE for various molecular and cellular endpoints, especially when considering dimensions relevant to the local complexity of DNA damage in the range of 10-20 nm range(26–28).

To a first approximation, RBE is a function of the (unrestricted) Linear Energy Transfer (LET), which is defined as the mean electronic energy-loss by a primary charged particle per unit path length(4,29,30). LET may be conveniently calculated from Bethe's stopping-power theory. The official connection of LET with radiation quality (or RBE) has been made by the International Commission on Radiation Protection (ICRP) in a series of reports(24,25,29). According to the ICRP, the quality factor, Q, is defined as the low-dose RBE (or $RBE_{max}$) for stochastic effects and may be expressed as a continuous function of LET. More recently, LET has been used in several empirical RBE models for tissue reactions (or deterministic effects) in the context of hadron therapy(31–34).

Despite its simplicity and wide applicability, there are well-known physical limitations of the LET concept, which are more profound when the site of interest is reduced to cellular and subcellular structures (micrometres to nanometres)(20–22,29). The most notable limitation of LET is that it neglects the stochastic nature of energy deposition (energy-loss straggling) from the charged particle to the medium while no consideration is given to the finite range of secondary electrons (δ-rays). Although the restricted LET, $L_{\Delta}$, which excludes those δ-rays with energy above a cut-off value Δ, can be used to better approximate the energy retained in the site, it still refers to a mean value and does not account for straggling(29,30).

The above limitations of LET can be overcome using microdosimetric approaches. For example, classical (or regional) microdosimetry considers a fixed-size critical site in which energy deposition distributions are linked to radiobiological effects. More advanced

microdosimetric approaches (e.g., structural microdosimetry) are available with the cost of increased calculation complexity and computing time(21,22,35).

Lineal energy (y) is the stochastic analog of LET and has been widely exploited in radiation quality studies as a measurable physical quantity by tissue-equivalent proportional counters (TEPC), also called Rossi counters(21,22). The biophysical justification of connecting lineal energy and the dose-weighted lineal energy ($y_D$) with RBE (or Q) is provided by the Theory of Dual Radiation Action (TDRA)(22,35,36). The official connection of lineal energy with Q has been made by the International Commission on Radiation Units and Measurements (ICRU) in its Report 40(29). The lineal energy has also been used in RBE studies of cell toxicity in the context of hadron therapy through the Microdosimetric-Kinetic Model (MKM)(31). Other microdosimetric-based models of Q used by NASA for space radiation can be found in several published works(4,15,17,37). Q is used to determine the quantity effective dose which corresponds to the stochastic (mainly carcinogenic) risk of irradiated individuals. In turn, the effective dose is used to calculate the number of safe days in space, a vital quantity for manned missions such as those to the Moon and Mars, i.e., the maximum number of days that astronauts can spend in space without exceeding their radiation dose limits. In proton radiotherapy, the effective dose is used to quantify the secondary cancer risk in healthy tissues that are exposed to stray proton radiation.

NASA has developed its own approach for determining Q, which differs from both ICRP (Report 60) and ICRU (Report 40) recommendations(7,15,38). NASA's quality factor is a function not only of LET, but also of the atomic number (Z) and the velocity (β) of the particle via the track-structure parameter $(Z/\beta)^2$. The energy loss from an ion to an atomic electron depends on the square of the ion's charge ($Z^2$). However, the energy isn't always confined to the target. Some of it can be carried away by secondary electrons. The extent to which this energy spreads depends on the ion's -normalized- velocity (β).

Theoretical calculations of lineal energy often employ Monte-Carlo track structure (MCTS) codes, such as GEANT4-DNA(39–43), KURBUC(44–46), PARTRAC(47), RITRACKS(48) and PHITS(49,50), among others. Many such efforts for determining the microdosimetric spectra for protons and heavier ions are available in literature (51). MCTS codes simulate, collision-by-collision, all the interactions between the primary (and secondary) particles and the atoms/molecules of the medium (commonly liquid water) until all particles (primaries and secondaries) become non-ionizing (i.e., fall below about 10 eV). Thus, MCTS codes enable simulations with nanometre resolution, including the explicit simulation of radiation-induced DNA damage at various levels of sophistication(51). However, MCTS simulations are well known for being time-intensive while requiring a fair amount of computer expertise.
Analytical models for calculating lineal energy spectra can overcome many of the above difficulties as they are based on simple mathematical expressions that approximate the energy-loss process. Such models have been developed in a series of papers by Xapsos (52,53) and Olko (54,55). The main idea is to analytically calculate the dependence of lineal energy upon LET while adding suitable correction terms for the effect of energy-loss straggling and the finite range of δ-rays.

# Chapter 2

## Literature Review: Concepts and quantities necessary for space radiation protection

### 2.1 Space radiation environment

The space environment is fraught with challenges for future explorers and astronauts. The main components of space radiation can be summarized as galactic cosmic rays (GCR), solar particle events (SPE), and the Van Allen belts.

#### 2.1.1. Galactic Cosmic Rays (GCR) radiation

Galactic cosmic rays (GCR) are generated outside our solar system and consist of relativistic particles with high ionizing potential. They irradiate isotropically and continuously at very low fluxes, peaking around 500 MeV/u as shown in Figure 1. Their immense energy, approximately up to $10^{20}$ eV, indicates that they originate from both galactic and extragalactic sources(3,4,9,10,12,13). Specifically, particles with energies less than $10^{15}$ eV are believed to be produced by shock waves from supernovae and neutron stars within the Galaxy, while higher energy particles are thought to originate from extragalactic sources(12). The precise origins of GCR remain unknown due to the interference of interstellar magnetic fields, which complicates their deciphering.

The composition of GCR is primarily baryonic (~98%) and leptonic (~2%). The baryonic component mainly consists of protons (85%), alpha particles (5%), and heavier nuclei up to uranium (~1%)(4,10,13,56–58). Particles with atomic numbers $Z \geq 3$ are referred to as HZE (High Z and Energy) particles. For space radiation protection, the particles of interest range from protons to iron ions (Fe), as the flux of heavier particles up to Uranium is considered too low to be significant. However, flux is not the only criterion; for example, iron's contribution to the GCR flux is 1/100 that of carbon, but the dose it delivers is much higher, as it depends on $Z^2$. For radiation protection the energy range that is considered to be a threat (for a typical shielding) for astronauts is between 100 MeV/u-100 GeV/u(5,8).

In addition to GCR, there is also an anomalous component of these particles (anomalous GCR). They are originally neutral particles from interstellar gas. These particles are then interacting with solar radiation and are accelerated by regions with fast and slow solar wind inside the heliosphere. Their energy is around 50 MeV/u, peaking around at 10 MeV, so they have limited penetration capabilities. Besides, they lose all their electrons after penetrating after a thin shielding.

Galactic cosmic rays (GCR) do not have a constant flux over the years and are influenced by solar conditions and the Sun's magnetic field(59–61). During periods of solar maximum, when the Sun's magnetic activity is very intense, GCR interact with and are deflected by this field, resulting in a shift of their flux to higher energies, since GCR with energies below 10 GeV are affected. Thus, at solar maximum, the GCR flux is at its minimum. Conversely, during solar minimum, the magnetic field is weaker and has less impact on the GCR distribution, leading to a maximum flux at lower energies. The difference in GCR flux between solar maximum and

minimum is approximately tenfold at 100 MeV, whereas at higher energies, such as 4 GeV/u, the difference is about 20% (5,13).

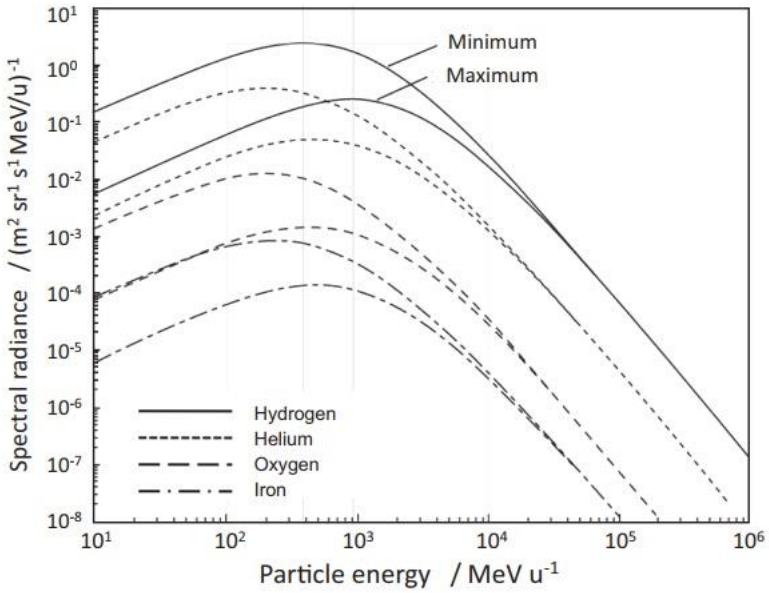


**Figure 1.** GCR differential flux as a function of particle energy (MeV/u) in solar minimum and maximum conditions for different ions (hydrogen, helium, oxygen and iron) [5].

### 2.1.2. Solar Particle Events (SPE)

Solar particle events (SPE) are generated by two primary solar explosive phenomena: solar flares and coronal mass ejections (CME). Solar flares are sudden explosions in the sun's corona near sunspots, releasing powerful amounts of magnetic energy and radiation across the electromagnetic spectrum, while CME are large clouds of magnetic mass (~$10^{14}$kg) ejected from the corona into the interplanetary medium(62–64). Previously, it was believed that only solar flares could produce SPE events. However, it is now understood that this is not always the case. Solar flares can produce an SPE, and the particles are accelerated impulsively. Around half of the SPE events are being accelerated through solar flares. The other type of an SPE events is caused by CME driven shocks in the interplanetary medium, where particles are being accelerated gradually(3,8,63,64). SPE events that are accelerated impulsively last several hours, have lower fluence and are less dangerous than the gradually accelerated events. SPE events vary significantly in flux, energy profile, and duration. They can last from several hours to several days and mainly consist of protons, with smaller amounts of heavier particles, reaching energies up to several GeV on some occasions, while the usual energy range is between the keV to several hundreds of MeV(65–67).

There are two potential distributions of SPE events: common events within a solar cycle and rare, large events that last several days, occur once per solar cycle or even less frequently, and have very high energy and fluence profiles. A significant SPE event can pose serious risks to astronauts, with particle fluxes exceeding $10^8$ particles per cm² for energies above 10 MeV. Predicting these events is challenging. SPE events from solar flares can reach Earth within 30 minutes to 1 day, while those from CME can take 1 to 4 days, depending on their kinetic energy(2,8,66). Since 1955, five high-energy SPE events have been recorded that would pose severe challenges to astronauts, as it shown in Figure 2. SPE events typically occur during the

solar maximum or its declining phase and are a major component of cosmic radiation. For space missions, it is crucial to probabilistically assess the likelihood of such large SPE events with extensive energy distributions. Despite the high energy and potential risk, protection against these SPE events is more manageable compared to other types of cosmic radiation(2–4,68).

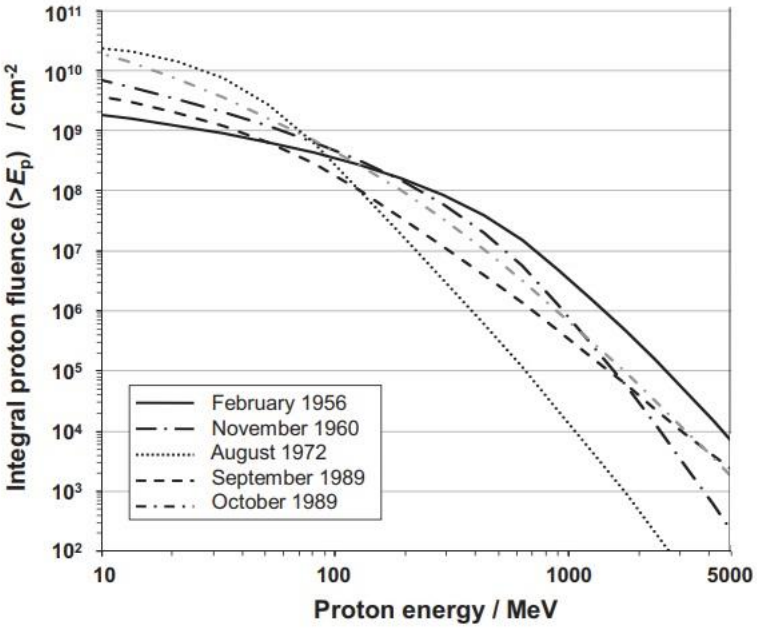


**Figure 2.** Integral fluence as a function of proton energy for the most intense solar particle events (SPE) in space era [5].

### 2.1.3. Van Allen Belts

Earth's magnetosphere consists of an inner dipolar magnetic field generated by the Earth and an outer region influenced by the solar wind, which carries the Sun's magnetic field. This solar wind can compress Earth's magnetic field. The magnetosphere forms two toroidal zones (inner and outer belts) containing temporarily trapped particles, resulting from interactions between galactic cosmic rays (GCR), the solar wind, and Earth's atmosphere and magnetic field. These zones, discovered by Van Allen in 1960, are composed mostly of electrons and protons with maximum energies of 7 MeV and 500 MeV, respectively(10,13,69). Heavier particles are fewer in number, with energies around 50 MeV, and thus do not pose a significant threat to manned missions since they cannot penetrate spacecraft shielding or reach deep into the magnetic field. The Van Allen belts extend from about 200 km to approximately 75,000 km above the Earth's surface.

Particles within magnetosphere exhibit three primary motions: helicating around magnetic field lines, moving and bouncing along field lines, which act as mirrors, confining the particles between two points, and drifting longitudinal around the Earth(10,12). Different processes contribute to the formation of trapped particles. In the inner zone, GCR interact with the upper atmosphere, producing neutrons that decay into protons and electrons. Heavier ions probably

originate from the anomalous component of the GCR. The outer zone mainly consists of electrons from the Sun.

A notable region of interest is the South Atlantic Anomaly (SAA), located near the coast of Brazil, where the inner Van Allen belt approaches the surface down to 200 km. This occurs because Earth's magnetic axis is tilted by 11.5 degrees and offset by about 500 km from the planet's center. The SAA presents a potential hazard to astronauts when passing through this region(10,69,70).

### 2.1.4. Radiation Fields in Low Earth Orbit (LEO) and deep space

For missions in Low Earth Orbit (LEO) extending in the region of 160 km to 2000 km, protons significantly contribute to the radiation dose received by astronauts, followed by electrons, less by helium and heavier particles. The radiation fields in LEO orbits depend much on the altitude and inclination of the mission, the solar cycle, the spacecraft shielding and the duration of the mission(71–74). Due to their higher energy and longer range compared to electrons, protons can often penetrate aluminium shielding of 0.3 g/cm². During extravehicular activities (EVAs), electrons also contribute, particularly affecting instruments and the skin organ. In LEO, radiation exposure mostly includes contributions from Galactic Cosmic Rays (GCR) and the South Atlantic Anomaly (SAA), an area encountered during orbital passes. Although the International Space Station (ISS) only spends about 15 minutes per pass in the SAA, it accounts for a significant portion of the radiation exposure(10,70,75,76).

Neutrons, produced by GCR interactions with Earth's upper atmosphere, also need to be addressed. There are two populations of neutrons: one with energies up to 10 MeV, created by highly excited nuclei, and another with high-energy neutrons around 100 MeV. However, their overall contribution to radiation in LEO is relatively low(3,10,70,73).

Earth's magnetosphere provides substantial protection against deep space radiation, as cosmic particles must penetrate this magnetic field to reach LEO. This penetrability depends on magnetic rigidity, the ratio of a particle's momentum to its charge. Earth's magnetic field is strongest at the equator and weakest at the poles, offering better protection for equatorial missions compared to polar ones. Therefore, high-energy particles are required to penetrate low-inclination orbits. During periods of intense geomagnetic activity, such as geomagnetic storms, the magnetosphere compresses, allowing lower-energy particles to penetrate deeper. On the ISS, Solar Particle Events (SPE) with energies above 100 MeV/u can pose a threat to astronauts(4,69,70,77,78).

In deep space, where Earth's magnetic field is absent, astronauts will encounter a new challenge since the Apollo era. They will face the full spectrum of particles from Galactic Cosmic Rays (GCR) and Solar Particle Events (SPE), without any modification by a magnetic field, relying solely on the shielding provided by their spacecraft. This means that the flux and intensity of particles will be higher than in Low Earth Orbit (LEO). Outside LEO orbit, in deep space, an astronaut's body will be penetrated by a proton every two days and by a heavier ion (e.g., carbon or iron) every month(4,79). The differences in particle fluence, from protons to iron, are illustrated in Figure 3, where the total particle fluences are depicted in two space radiation environments (ISS, deep space) and two solar conditions(5).

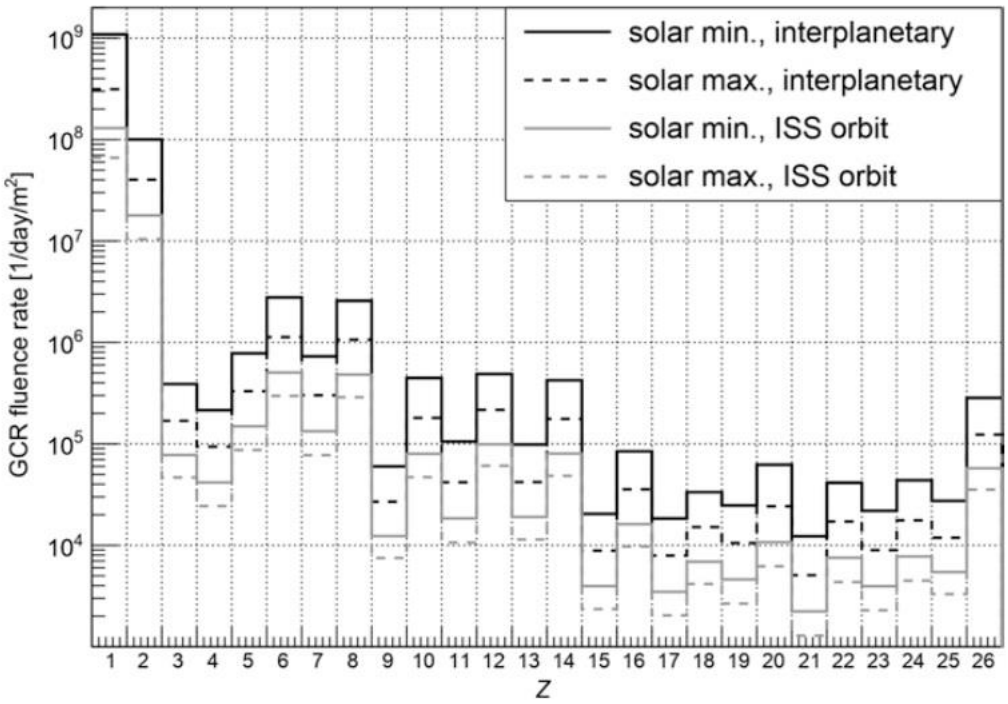


**Figure 3.** GCR fluence for each ion with atomic number Z, in solar minimum and maximum conditions and two space environments (ISS orbit, and interplanetary deep space) (5).

### 2.1.5. Radiation Fields on the surface of the Moon and Mars

Upcoming manned space missions to the Moon and Mars necessitate a thorough understanding of the radiation environment on these surfaces to ensure astronaut safety. Radiation fields on the surfaces of the planets depend on several factors, including the existence of a magnetosphere, atmosphere thickness and composition and materials of the soil. The exposure to astronauts in these surfaces is expected to be half of the exposure in deep space(80,80–84).

The Moon lacks a dipole magnetic field and has no substantial atmosphere, offering no protection against radiation. The only attenuation comes from lunar surface (radiation incident only in a $2\pi$ geometry) and the potential use of lunar regolith and bedrocks as shielding in future habitats. Additionally, secondary radiation, primarily neutrons, photons and secondary ion fragments, originates from the interaction of GCR with the lunar regolith, rocks and dust, whose chemical composition includes mostly $SiO_2$, FeO, $Al_2O_3$ and CaO(80–82,84–90).

Similarly, Mars does not possess a dipole magnetic field but has a thin atmosphere ($20 g/cm^2$) compared to Earth's ($1000 g/cm^2$). Consequently, astronauts are vulnerable to GCR, SPE, and secondary radiation from GCR or SPE interactions with the Martian soil. Mars dust storms can also scatter neutrons and secondary ions. Martian regolith can also be used as radiation shielding for future exploration missions. Understanding these environments is crucial for the development of effective protection strategies for astronauts(91–98).

### 2.1.6. Interaction of radiation with shielding

The radiation from GCR and SPE ions interacts with spacecraft shielding in two main ways: through Coulombic electrical forces and nuclear interactions. These interactions alter the original particle's energy and generate secondary radiation, which can pose risks to astronauts. The thickness and the material composition of the shielding can increase the difference between the external and internal radiation. Various types of radiation, including gamma rays, secondary electrons, neutrons, pions, muons, and secondary ions, can be produced(4,5,13). This secondary radiation significantly contributes to the primary components from SPE and GCR and can penetrate the human body, causing further alterations. Currently, there is not a highly effective shielding against GCR. Generally, materials with a low atomic number, such as hydrogen (in liquid form), are most effective in reducing the energy of the primary beam and do not significantly contribute to the creation of secondary neutrons. Aluminium, the most common material used for spacecraft shielding, balances cost-effectiveness, reduction of primary beam energy, and the generation of secondary neutrons and ions. High atomic number materials like lead or concrete are nearly prohibitive due to the high transportation costs to space and the substantial production of secondary neutrons and other ions(2,4,38).

### 2.2. Quantities used in Radiation Protection

The purpose of radioprotection is to safeguard the general population and radiation workers (whether on Earth or in space) from the biological effects of ionizing radiation, according to the circumstances. Two types of biological effects are of concern for radioprotection. The deterministic biological effects, which are responsible for the death of many cells, can manifest in humans shortly after a single exposure to high doses (0.5 Gy) within a few hours to several weeks and have specific dose thresholds. Therefore, radioprotection must set dose limits below the threshold for these biological effects, in order not to occur. Some acute (or deterministic) biological effects with varying dose thresholds include skin conditions, sterility, cataracts, and, in rare cases of nuclear accidents, acute radiation syndrome (following whole-body irradiation) with its prodromal symptoms (nausea, vomiting, fatigue, fever, etc.)(24,25,99).

Almost always, the general population will not be exposed to high doses of radiation unless a nuclear accident occurs or if exposed for radiotherapy purposes, where the highest dose targets the tumour(33). The general population and radiation workers are exposed to low dose rates/doses (mGy), leading to the primary biological concern being stochastic effects, which which may include mutations, with the most significant being the potential for carcinogenesis (and hereditary effects). For stochastic effects, there is no dose threshold as it is a probabilistic phenomenon, and radiation-induced carcinogenesis appears after at least 5-10 years(4,24). Thus, a dose threshold to prevent carcinogenesis cannot be established, only an upper allowable limit for the population and workers to reduce it. The upper limit aims to protect the population, while not restricting the beneficial applications of ionizing radiation. The applications of ionizing radiation include radio diagnostic and radiotherapeutic procedures, and their use in industries, nuclear reactors, etc.(24,100)

The quantities used for astronaut radiation protection follow the concepts and quantities proposed by the International Commission on Radiological Protection (ICRP) over the years for the stochastic effects(24,99). These measures were initially developed for the radiological protection of the general population and radiation workers on Earth. Space radiation is significantly different from terrestrial radiation, which is mostly limited to gamma rays, electrons, and, to a lesser extent, neutrons and alpha particles (for internal exposure). Additionally, the exposure astronauts face is much greater than that on Earth, and the radiation

fields in space are a combination of multiple beams rather than a single source. The commonly used quantities are as follows:

**Absorbed dose (D):** The most fundamental physical quantity used for radiation protection, radiobiology and radiology is the absorbed dose (D). It is the quotient of the mean energy ($\bar{\varepsilon}$) imparted to matter divided by the mass (m) of the target that we investigate. It is calculated by the following equation:

$$D = \frac{d\bar{\varepsilon}}{dm} . \quad (1)$$

Absorbed dose is measured in Gray (Gy). The S.I unit is Joule/kg.

**Linear Energy Transfer (LET):**

It is the mean energy lost ($d\bar{\varepsilon}$) by a charged particle due to electronic interactions per transversed distance dl inside a target(30,101):

$$LET = \frac{d\bar{\varepsilon}}{dl} . \quad (2)$$

To understand the biological effects of different types of ionizing radiation on human tissues, the absorbed dose (D) of organs is not a sufficient measure. This is because different types of IR can produce different biological effects for the same value of D. The main reason for this discrepancy is the varying way in which different types of ionizing radiation deposit their energy at a microscopic level (cellular and DNA level)(28,102). This observation is quantified through the Relative Biological Effectiveness (RBE). The RBE for a specific biological effect (e.g., cell death, double-strand breaks in DNA, chromosome aberrations) is defined as the ratio of the absorbed dose of a reference radiation, $D_{ref}$ (usually gamma radiation), to the absorbed dose of a test radiation, $D_{test}$. It is described by the following equation(103):

$$RBE = \frac{D_{ref}}{D_{test}} . \quad (3)$$

The **Relative Biological Effectiveness (RBE)** depends on several factors including the absorbed dose, dose rate, type of cell, and the quality of the radiation, which encompasses the type and energy of the radiation. For stochastic effects (low doses/dose rates), the RBE reaches its maximum value, referred to as $RBE_{max}$, which is also known as the **quality factor (Q)** or $w_R$. This maximum value indicates the highest potential for biological damage from the radiation under those specific conditions(24,99).

To account for the different biological effectiveness of different types of radiation, **equivalent dose (H)** must be addressed. It is calculated in individual organs (T), and it is based on absorbed dose (D), which is adjusted by a weighting factor for each radiation. Equivalent dose is expressed in Sieverts (Sv) and the SI unit is J/kg(99):

$$H_T = \sum_R D_T \times w_R , \quad (4)$$

where the summation is over the different types of radiation (R). Before ICRP Report 60 in 1990 and the weighting factor $w_R$, the mean quality factor ($Q_T$) of an organ was utilized for the adjustment of the absorbed dose for each radiation and it was termed **dose equivalent**, **($H_{T,Q}$)** (ICRP Report 26). It can be calculated by(24):

$$H_{T,Q} = D_T \times Q_T . \quad (5)$$

**Table 1.** Recommended radiation weighting factors ($w_R$) [97]

| Type of Radiation | $w_R$ |
|---|---|
| Photons | 1 |
| Electrons, muons | 1 |
| Proton, pions | 2 |
| Alpha particles, heavy ions, fragments | 20 |
| Neutrons | Continuous function of energy (ICRP 2007) |

Different organs/tissues have different radiosensitivity for the induction of stochastic effects, which are accounted by the tissue weighting factor $w_T$. The summation of dose equivalent for each organ over all organs is termed as **effective dose (E)** and refers to the whole-body irradiation. Effective dose is expressed in Sieverts (Sv) and the SI unit is in J/kg. It is calculated by the following expression(99):

$$E = \sum_T w_T \times H_T \ . \quad (6)$$

The summation of each organ/tissue must be equal to 1. Each weighting factor $w_T$ represents the contribution of each organ/tissue to the total whole-body detriment. Effective dose was introduced in ICRP Report 60 and refined in ICRP Report 103.

Likewise, if Q is used instead of $w_R$, then the effective dose is termed as **effective dose equivalent ($E_Q$)**(24):

$$E_Q = \sum_T w_T \times H_{T,Q} \ . \quad (7)$$

**Table 2.** Recommended tissue weighting factors ($w_T$) [99]

| Organ | $w_T$ | Organ | $w_T$ |
|---|---|---|---|
| **Gonads** | 0.20 | **Bladder** | 0.05 |
| **(red) Bone marrow** | 0.12 | **Breast** | 0.05 |
| **Colon** | 0.12 | **Liver** | 0.05 |
| **Lung** | 0.12 | **Oesophagus** | 0.05 |
| **Stomach** | 0.12 | **Thyroid** | 0.05 |
| **Skin** | 0.01 | **Bone surface** | 0.01 |
| - | - | **Remainder tissues** | 0.05 |

### 2.3. Biological effects of space radiation

During space travel, astronauts will be continuously exposed to whole body low doses and low dose rates of Galactic Cosmic Rays (GCR). Occasionally, they will also encounter Solar Particle Events (SPE), which expose them to high doses and high dose rates for a limited period.

#### 2.3.1. SPE

Solar particle events (SPE) exhibit a very high flux, exceeding $10^8$ particles/cm$^2$, with energies reaching up to several GeV, although the peak flux often occurs at energies below 100 MeV.

Due to the high flux and associated dose, the primary concern for radiation protection in space is the acute biological effects that SPE can cause(104,104–106). The typical shielding used in spacecraft is sufficient to reduce the dose from SPE to levels that prevent acute radiation syndrome and its early symptoms, which begin at approximately 0.5-1 Gy and above.

High doses from SPE can also cause reduced fertility (at about 0.15 Gy) or permanent sterility (at 0.5-4 Gy). The skin is a critical organ in radiation protection as it serves as the body's first line of defence against radiation and can be damaged at doses around 6 Gy. Other organs at potential risk from SPE radiation include the gastrointestinal system (stomach, small intestine), which can be affected by whole-body irradiation of 4-5 Gy(106–110).

The real danger though, arises when astronauts remain outside their spacecraft (e.g., during extravehicular activities or on the surface of a planet away from any shelter) for extended periods. However, the likelihood of developing acute radiation syndrome or its prodromal symptoms behind spacecraft shielding is rare(15,66).

### 2.3.2. GCR

Galactic Cosmic Rays (GCR) pose the greatest risk for biological effects in space due to the insufficient shielding available to protect against them. The biological effects of heavy ions (HZE particles) remain largely unknown due to a lack of experimental data. GCR, despite their relatively low flux—protons at 4 particles/cm$^2$/s, alpha particles at 0.4 particles/cm$^2$/s, and heavier ions at 0.04 particles/cm$^2$/s—pose a significant threat to astronauts due to continuous exposure.

GCR are the primary concern for inducing carcinogenesis(4,7,111–114) and other biological effects such as damage to the central nervous system (CNS)[104,106,113,114], cardiovascular disease (CVD) (such as coronary heart disease and stroke)(106,117–122), and cataracts(5,13). Carcinogenesis is considered the number one concern, influencing the establishment of dose limits for stochastic effects. The organs that are more susceptible to radiation-induced cancer are breast, colon, thyroid and lungs. Besides cancer, cataracts, cardiovascular effects, dysfunctions in the endocrine and immune systems, and damage to the central nervous system (CNS), such as deficits in orientation, memory, fatigue, reaction time, are also significant concerns for space agencies, especially for long-duration manned missions. Radiobiological data for these health outcomes are very sparse and the potential physical mechanism behind the induction of CNS and CVD damage is know yet fully understood(15).

Heritable effects, though lacking specific data related to GCR, is considered less of a concern compared to somatic biological effects, being ten times less likely to occur. Cataract formation is the only confirmed biological effect directly caused by space radiation, though no specific dose threshold has been associated with this biological effect(5,13).

For all these mentioned biological effects, the greatest uncertainty in determining the impact of GCR lies in the values of the Relative Biological Effectiveness (RBE) and Quality Factor (Q) for space radiation(15). As it will be mentioned in the next section, there are no definitive values for these parameters, because the cancer risk estimates rely mostly on the survivors of the atomic bombs, while the data for cancer incidence/mortality on the astronaut group are extremely limited(18).

### 2.3.3. Dose limits for manned space missions beyond LEO

The inevitable exposure of astronauts to space radiation classifies them as radiation workers. The dose limits that must be taken into account are based on acceptable risk following the ALARA (As Low As Reasonably Achievable) principle and vary depending on the circumstances. On Earth, dose limits differ between the general population and radiation workers, with the former having a maximum dose limit of 1 mSv/year and the latter set at 20 mSv/year, according to the ICRP(99,103). This is based on the calculation that 1 Sv causes an additional 5% risk of cancer. Dose limits for stochastic effects primarily concern the probability of cancer development, as it is the predominant biological effect of interest in both terrestrial and space radiation protection. For deterministic effects, which may result from potential solar particle events (SPE) in rare cases, space agencies such as NASA, ESA, JAXA, RSA, and CSA agree and follow ICRP and NCRP recommendations for various organs at risk (Blood Forming Organs, eye lens, skin) as presented in Table 3.

To date, there is no unified methodology for the assessment of cancer risk among the space agencies engaged in manned space missions, as well as established radiation limits for the astronauts(15,17,19). Until 2012, for LEO missions, NASA followed ICRP recommendations for the estimations of the quality factor. Until 2020 NASA has followed the US National Council on Radiation Protection and Measurements (NCRP) recommendations for dose limits and adopted the age- and sex-dependent risk of exposure induced death (REID) as the main risk metric(15,17,19). Previous career dose limits were defined as the 3% REID with 95% Confidence Level (CL), due to uncertainties mostly of the quality factor. This risk metric has been calculated from the NASA's cancer risk model (Nasa Space Cancer Risk Model, NSCR) which was developed in 2010, with additional updates over the years(15). Newly suggestions in 2021 by National Academies of Sciences (NAS)(123) supported the fact the NASA should use the value of 600 mSv as the effective dose career limit, calculated from the 3% REID of a 35-year-old female, and apply it to all astronauts regardless of gender and age. This new limit although more practical, it is free of uncertainties and concerns have been risen for the implementation to space missions.

JAXA follows a similar risk-based method with the same 3% limit. ESA and CSA adhere to ICRP Report 60 recommendations without having developed a concluded cancer risk model, setting the career dose limits for astronauts the value of 1Sv, resulting from a 20-year astronaut career and an upper limit of 50 mSv/year for radiation workers. Nevertheless, these dose limits need reassessment, as the ICRP recommendations established the limit of 20 mSv/year for radiation-exposed workers on Earth(124).

The RSA has developed its own model based on the concept of generalized dose, setting an upper limit at 10% for cancer risk and deterministic effects, corresponding to effective dose of 1 Sv(19).

No space agency among the aforementioned takes into account the late biological effects of Galactic Cosmic Rays (GCR) within these limits (REID 3% or 1 Sv). These effects include significant uncertainties related to the central nervous system and cardiovascular diseases, which are crucial considerations for radiation protection both on Earth and in space. NASA although, has proposed some preliminary limits for these biological effects, but much research must be done in order to obtain solid guidance.

**Table 3.** Dose limits for non-cancer effects for 30 days, 1 year and astronaut's career [15].

| Organ | 30-day limit | 1 year limit | Career limit |
|---|---|---|---|
| Lens | 1 Gy (RBE weighted) | 2 | 4 |
| Skin | 1.5 | 3 | 6 |
| Blood-Forming Organs | 0.250 | 0.5 | Not applicable |
| Heart | 0.250 | 0.5 | 1 |
| Central Nervous System (CNS) | 0.500 | 1 | 1.5 |

## 2.4. Introduction to Microdosimetry

Microdosimetry, a branch of dosimetry that studies the spatial distribution of energy deposition by ionizing radiation in microscopic targets, was pioneered by H.H. Rossi in the 1950s(125,126). Rossi introduced the use of tissue-equivalent proportional counters (TEPC), commonly known as Rossi counters, to measure the linear energy transfer (LET) of various ionizing radiations. At that time, LET was considered the most appropriate quantity to describe the radiation quality, encompassing both the type and energy of the radiation, and its observable biological effects.

Microdosimetry focuses on the interactions of ionizing radiation with matter and the spatial deposition of energy at microscopic scales (micrometers). Ionizing radiation interacts with matter in a unique and stochastic way and understanding the microscopic distribution of energy deposition is crucial for elucidating the physical mechanisms of radiation-matter interactions and their biological outcomes. This was the primary aim of microdosimetry: to determine how the stochastic nature of radiation-matter interactions affects our understanding of biological effects(23,125).

The theoretical framework of microdosimetry was formulated by Kellerer, who identified two primary concepts within the field(23,127). The classical approach, upon which Rossi detectors are based, is termed regional or site microdosimetry. This approach involves analysing regions of specified dimensions (sites) where the absorbed energy from ionizing radiation is considered without regard to its detailed microscopic distribution within the site.

In contrast, Kellerer introduced a more advanced form called structural microdosimetry. Structural microdosimetry provides a detailed description of the microscopic pattern of energy absorption, also known as the inchoate distribution. This approach is fundamentally important because the deterministic biological effects of radiation are essentially determined by the intersection of this energy absorption pattern with the sensitive components within the irradiated matter.

Microdosimetry is vital for applications in radiation science that needs precision and good knowledge of interactions between radiation-matter. These applications involve radiation protection, radiation therapy and radiobiology(21,22).

Deterministic quantities, such as D and LET, do not capture stochastic aspects of the interactions of charged particles with the medium in small (~nm-μm) volumes. The stochastic fluctuations of energy deposition and the finite range of secondary (delta) electrons in small target volumes of interest for assessments of molecular and cellular damage may be crucial and, in general, need to be considered(20,22,23,51,128).

In microdosimetry, the stochastic analogues of D and LET, are represented by the specific energy (z) and the lineal energy (y), respectively. Lineal energy is the quotient of the energy imparted by a single primary particle and/or its secondary particles (delta electrons and/or secondary ions), inside a target volume divided by the mean chord length ($\bar{l}$) of that volume (22):

$$y = \frac{\sum_i \varepsilon_i}{\bar{l}}, \tag{8}$$

where the summation is over all the individual stochastic energy deposits ($\varepsilon_i$). Lineal energy is usually expressed in units of $keV/\mu m$, while the mean chord length for a sphere is $\bar{l} = 2d/3$, where d is the sphere's diameter. This mean value of $\bar{l}$ results from the so-called μ-randomness, in which the target is isotropically and uniformly intersected by infinite straight lines (22,129). To a good approximation, this condition holds for experimental microdosimetry, external beam radiotherapy, and for space radiation.

Concerning radiation quality, it is of interest to define two average values of y, namely the frequency-mean ($y_F$) and the dose-mean ($y_D$) lineal energy which are described by the following equations(20,22,23):

$$y_F = \int y f(y)\, dy, \tag{9}$$

and

$$y_D = \frac{1}{y_F} \int y^2 f(y)\, dy. \tag{10}$$

Similarly, specific energy (z) is the energy deposited in a target per unit mass of the target under study:

$$z = \frac{\sum_i \varepsilon_i}{m}, \tag{11}$$

Correspondingly, the frequency-mean ($z_F$) and dose-mean specific energy ($z_D$) are defined. They can be calculated by the following integrals:

$$z_F = \int z f(z)\, dy, \tag{12}$$

and

$$z_D = \frac{1}{z_F} \int z^2 f(z)\, dy. \tag{13}$$

Monte-Carlo Track-Structure (MCTS) codes, such as GEANT4-DNA (40,130), KURBUC (44), RITRACKS (48), PARTRAC (47), among others(51), represent the state-of-the-art in the calculation of microdosimetric quantities. These codes typically simulate all the main interactions (i.e., ionizations, excitations, and elastic collisions) of particles within the

irradiated medium, thus, obtaining the spatial distribution of energy deposition with putative molecular resolution.

Such MCTS simulations incorporate microscopic (or discrete) physical models that may have increased, albeit unknown, levels of uncertainty for low-energy ions and delta-rays, i.e., so-called track-ends. Still, MCTS codes remain today the most accurate tool for obtaining estimates of microdosimetric quantities like $y_D$. General purpose Monte-Carlo codes, such as Geant4 (131–133), PHITS(49), MCNP (134), FLUKA (135,136), and PENELOPE (137), although more rigorously benchmarked than MCTS codes, are not suited for nanometer (or sub-micron) targets because of limitations of the condensed-history approach. For larger targets (diameter > 1 μm), condensed-history ion-transport methods are potentially useful with the selection of appropriate transport parameters(138).

The importance of microdosimetry in radiation quality problems has recently led several general-purpose MC codes to include track-structure functionality (45,50,139–141) and hybrid RBE/microdosimetry modelling(142) to be able to switch from a macroscopic (condensed-history) to a microscopic (track-structure) modelling of radiation transport. Published studies suggest a hybrid approach to practical calculations of $y_D$ values is possible by combining small-scale analytic models with larger-scale condensed history models to account for geometry and tissue heterogeneities(142). Hybrid microdosimetry models combine the specifics of the irradiation geometry with the smaller-scale transport physics necessary for the accurate accounting of energy-loss straggling and the finite range of secondary electrons in small volumes. There have been several microdosimetry-based analytic models for charged particles (53,54,143–146), each one developed and applied for a specific energy range, target medium and a specific or limited range of ion types.

### 2.5. The quality factor problem

The radiation quality factor represents a critical parameter in assessing the impact of space radiation on astronauts during manned space missions, as it is multiplied to the absorbed dose (D) for the calculation of the dose equivalent of an organ, which indicates the risk of a stochastic biological effect to occur. Astronauts' cells are regularly exposed to protons every 3 days, and encounters with heavier nuclei, denoted as High Atomic Number and Energy (HZE) particles, occur approximately once every few months(106).
For manned space exploration, the radiation quality factor stands out as a quantity characterized by considerable uncertainties, over 400-500%(15,147). This factor is crucial not only for refining cancer risk assessments but also for devising robust shielding and mission planning strategies. Notably, the primary challenge arises from the fact that most radiobiological data used for RBE/ Q estimations pertain to low Linear Energy Transfer (LET) and high-dose rate exposures, predominantly involving photons, while GCR continuously irradiate astronauts in a low-dose rate, with a broad spectrum of high-LET particles. The estimation of RBE for High-LET particles has primarily relied on data derived from the Life Span Study (LSS), neutron contribution and studies involving medical patients and miners exposed to alpha particles.

However, these estimations present limitations, including statistical constraints and issues related to dose range. Notable uncertainties also exist in the Low-LET epidemiological data from the Life Span Study (LSS)(148). Moreover, experimental data for fast protons and heavier ions within the dose range relevant to space exploration and biological effects, such as cancer induction, degenerative late effects in the CNS, and CVD are relatively scarce. These limited

experiments however, showed an increased effectiveness of heavier particles in tumour induction quantitively and qualitatively(15,16).
RBE/Q for energetic protons above 20-30 MeV, is generally considered close to 1, but the RBE/Q between the different calculation methodologies of lower energy protons (<20 MeV) are not in agreement(15,149). High energy protons (above 50 MeV), although their relatively low RBE/Q (~1), produce delta electrons that can travel several μm in tissue that need to be considered for further cell damage. Protons with energy levels below 20 MeV exhibit limited penetration capabilities and are particularly relevant to considerations for the skin organ, when generated internally within the human body after nuclear interactions, or when higher energy protons are mitigated through shielding or human body. In contrast, heavier ions display elevated RBE/Q values and are deviating among the theoretical calculation methods(15,16).
Radiation quality plays a major role in the radiobiological effects observed in living matter, and it is commonly described by relative biological effectiveness (RBE). To a first approximation, RBE is a function of the (unrestricted) Linear Energy Transfer (LET), which is defined as the mean electronic energy-loss by a primary charged particle per unit path length. LET may be conveniently calculated from Bethe's stopping-power theory(20). The official connection of LET with radiation quality (or RBE) has been made by the International Commission on Radiation Protection (ICRP) in a series of reports(24,25,99). According to the ICRP, **the quality factor, Q, is defined as the low-dose RBE (or $RBE_{max}$) for stochastic effects** and may be expressed as a continuous function of LET. More recently, LET has been used in several empirical RBE models for tissue reactions (or deterministic effects) in the context of hadron therapy(32–34). Despite its simplicity and wide applicability, there are well-known physical limitations of the LET concept(15,79,102,128), which are more profound when the site of interest is reduced to cellular and subcellular structures (micrometres to nanometres). The most notable limitation of LET is that it neglects the stochastic nature of energy deposition (energy-loss straggling) from the charged particle to the medium while no consideration is given to the finite range of secondary electrons (δ-rays). Although the restricted LET, $L_{\Delta}$, which excludes those δ-rays with energy above a cut-off value Δ, can be used to better approximate the energy retained in the site, it still refers to a mean value and does not account for energy straggling.
A suitable radiation quality descriptor is essential for accurately quantifying differences, other than Linear Energy Transfer (LET), especially to represent the densely concentrated energy depositions along HZE tracks. This necessity arises due to RBE/Q 's dependence on the particle's track structure and delta-rays range. The precision of the radiation quality descriptor is crucial for predicting RBE/Q for heavy ions in the absence of experimental data. Qualitatively, the distinctions between High-LET radiation and Low-LET radiation include the induction of more aggressive and lethal tumours, the involvement of non-target effects (NTE), alterations in gene expression, and variations in cell responses to radiation(15).

### 2.6. Methods for calculating the quality factor (Q)

#### 2.6.1. ICRP Report 60

The International Commission on Radiation Protection (ICRP) Report 60 (24) has defined Q as a continuous function of the unrestricted Linear Energy Transfer (L) in water. The simplicity of the Q(L) approach along with the availability of an analytic formula for calculating L (i.e., Bethe's stopping-power formula) for ions over a broad energy range is the main advantage of this method. According to ICRP the Q(L) values can be obtained from the following equations (24):

$$Q(L) = 1, \quad L < 10 \text{ keV/}\mu\text{m} \quad , \tag{14}$$

$$Q(L) = 0.32L - 2.2 , \quad 10 \text{ keV/}\mu\text{m} \leq L \leq 100 \text{ keV/}\mu\text{m} \quad , \tag{15}$$

$$Q(L) = \frac{300}{\sqrt{L}}, \quad L > 100 \text{ keV/}\mu\text{m} \quad . \tag{16}$$

The above Q(L) equations have been deduced from RBE data based on animal experiments and radiobiological studies at cellular level (24).

### 2.6.2. NASA model

NASA has developed a radiation cancer-risk model that distinguishes the RBE for solid cancers and leukaemia based on recent radiobiological and epidemiological data. It also accounts for the different ionization density contributions of particles using the track structure parameter $Z^2/\beta^2$ and separates between the low-LET component ($Q_{Low}$) and the high-LET ($Q_{High}$) component. Contrary to the LET approximation of ICRP, NASA characterizes Q with a fluence-based approximation of risk cross sections, $\Sigma(Z, E)$. Risk cross section is simply the probability per unit fluence of a biological effect (e.g., leukaemia) to occur for a specific ion with atomic number Z and energy E and it is based on the biophysical model of Katz (150). The NASA model for Q is described by the following equation (16):

$$Q_{NASA} = \left(1 - P(Z, E)\right) + \frac{6.24(\Sigma_o/\alpha_\gamma)}{LET} P(Z, E) , \tag{17}$$

where

$$P(Z, E) = \left(1 - e^{\frac{-(Z*/\beta)^2}{k}}\right)^m \left(1 - e^{-(E/0.2)}\right) . \tag{18}$$

The first term of the right-hand of Eq. (17), is the $Q_{Low}$, while the second term accounts for $Q_{High}$. The ratio $(\Sigma_o/\alpha_\gamma)$ is treated as a fitting parameter and $\alpha_\gamma$ is the linear slope of the dose-response curve of γ-rays (low-LET). $Z^*$ is the effective charge, $\beta$ is the velocity of the particle normalized to the speed of light and the term $(E/0.2)$ accounts for the reduced effectiveness (reduced radial dimensions) of the particles as they slow down. The experimental parameters k and m account for the maximum location of the RBE including the saturation effects, and the slope of the cross section, $\Sigma_o$, respectively. The central/standard values for the above parameters obtained from NASA's 2012 cancer risk model are shown in Table 4. Additional modifications of NASA's model and updates can be found in literature(15,148).

**Table 4.** Standard values of the fitting parameters used in the NASA model for Q.

| Fitting Parameters | Solid Cancer | Leukaemia |
|---|---|---|
| $(\Sigma_o/\alpha_\gamma)$ | 7000/6.24 | 1750/6.24 |
| k | 1000, Z≤4 | 1000, Z≤4 |
| | 500, Z >4 | 500, Z >4 |
| m | 3 | 3 |

An alternative approach for quality factor estimations, involves the utilization of microdosimetry. The distinctive advantage of microdosimetry is that it physical establishes the observed biological effects with the track-structure of ionizing particles and it is quantified using Tissue Equivalent Proportional Counters (TEPC). Microdosimetric quantity of lineal energy (y) contrary to LET, is closely associated with the actual energy imparted to a volume by an ionizing particle per unit path length, and considers not only energy-loss straggling, but also the finite range of secondary electrons (22). While lineal energy is a measurable quantity through experimental means using TEPC, its theoretical calculation presents a challenge. In addition, lineal energy values are subject to the irradiation conditions and the geometry, while there is no unanimous agreement regarding the optimal size for researching the biological effects(27,36). Nanometer-scale targets at the level of DNA (10-20 nm) or segments of chromosomes (100nm) may be deemed preferable in this context (26). These complexities pose an obstacle in accurately predicting the RBE/ Q for heavier nuclei based on microdosimetric considerations.
The TEPC are simulating the tissue in micron size volumes and register the stochastic energy depositions inside that volume. It has been implemented in LEO for ISS and space shuttle missions for quality factor estimations. Although TEPC measure the lineal energy spectrum, calculations often employ the quality factor as a function of LET (Q(L)) guided by ICRP Report 60, due to its simplicity, because the fluence of heavier particles inside the Earth's magnetic field is much lower than in deep space and that the maximum stay of astronauts in LEO missions is around 1 year, with most typical stay around 4-6 months. In the above LEO missions, a 2-micrometer TEPC was installed and the observed differences between Linear Energy Transfer (LET) and the average particle spectrum of lineal energy (y) were found to be modest to be of concern. Consequently, the utilization of Q (L) for calculations yielded small discrepancies in the average quality factor estimations(75,78,151–154). However, if astronauts travel in deep space Beyond LEO (BLEO), and precision and reduction in the simulation size of TEPC (to hundreds of nanometers) is needed, then it introduces the necessity for calculating a microdosimetric quality factor. This quality factor can be guided by established frameworks such as the International Commission on Radiation Units and Measurements (ICRU) Reports 36(20) and 40(29), the mechanistic model of TDRA(22), or other practical approaches(155).

### 2.6.3. Theory of Dual Radiation Action (TDRA)

The most practical (and used) formulation of the Theory of Dual Radiation Action is the so-called "site model" which assumes that cellular biological effects are caused by the pair-wise interaction of sub-lesions produced within a fixed-size target. Importantly, the probability of two sublesions to interact is independent of their geometric distribution within the site. It follows from TDRA that sublesions are produced either in the same track (for high-LET radiation) or in two separate tracks (for low-LET radiation). The general expression of RBE of the site version of TDRA takes the following form (22,35):

$$\mathrm{RBE_{TDRA}} = \frac{\sqrt{(c \times y_{D,L})^2 + 4D_H(c \times y_{D,H} + D_H)} - (c \times y_{D,L})}{2D_H}, \quad (19)$$

where c is a normalization constant (36), $D_H$ is the dose from the high-LET radiation and $y_{D,L}$, $y_{D,H}$ are the low- and high- LET dose-mean lineal energy, respectively. Then, in the **low-dose regime** ($D_H \ll c \times y_{D,L}$) where $Q = \mathrm{RBE}_{D\to 0}$, Eq. (19) reduces to:

$$Q_{TDRA} = \frac{y_{D,test}}{y_{D,ref}}, \quad (20)$$

where $y_{D,test}$ and $y_{D,ref}$ are the dose-mean lineal energy of the test and the reference radiation, respectively. For many radiobiological effects (including cancer-related effects), the RBE (or Q) increases with LET up to a certain value, beyond which any additional increase of LET causes a reduction of the biological effect (the so-called overkill effect). This is relevant to the **high-LET particles of GCR**. As a result $y_D$ is replaced by the dose-weighted saturated lineal energy ($y_D^*$) (29). Hence, Equation (20) becomes (22,29):

$$Q_{TDRA} = \frac{y_{D,test}^*}{y_{D,ref}^*} \ . \tag{21}$$

### 2.6.4. The ICRU Report 40 Recommendations

The International Commission on Radiation Units and Measurements (ICRU) Report 40 was the first to officially link the quality factor Q with the microdosimetric quantity lineal energy (*y*) using the following analytic expression(29):

$$Q_{ICRU40} = \frac{5510}{y}[1 - Exp(-5 \times 10^{-5} y^2 - 2 \times 10^{-7} y^3)] \ . \tag{22}$$

As a result, for a specific ion energy, the mean quality factor Q can be calculated from:

$$\overline{Q} = \frac{\int Q_{ICRU40}(y_{test}) \ d(y_{test}) dy}{\int Q_{ICRU40}(y_{ref}) \ d(y_{ref}) dy} \ , \tag{23}$$

where d(y) is the dose-weighted distribution of lineal energy defined by $d(y) = (y/y_F)f(y)$. The difficulties in understanding the effects of high-LET radiation, and thus in the calculation of Q, were compensated by the choice of a quantity that can be measured and at the same time be physically appropriate. Therefore, lineal energy was to be determined in a tissue-equivalent sphere with a diameter equal to 1 μm, which is experimentally feasible using TEPC.

# Chapter 3

**Summary**[1]

In this work, various generalized analytical models were utilized and combined to determine the proton lineal energy spectra in liquid water spheres of various sizes (i.e., 10-3000 nm diameter) over the proton energy range of 1–250 MeV. The calculated spectra were subsequently used within the Theory of Dual Radiation Action (TDRA) and the ICRU Report 40 microdosimetric methodologies to determine the variation of Q with proton energy. The results revealed that the LET-based Q values underestimated the microdosimetric-based Q values for protons with energy below ~100 MeV. At energies relevant to the Bragg peak region (<20–30 MeV), the differences were larger than 20–50%, while reaching 200–500% at ~5 MeV. It was further shown that the microdosimetric-based Q values for protons below ~100 MeV were sensitive to the sphere size. Finally, condensed-phase effects had a very small (<5%) influence on the calculated microdosimetric-based Q over the proton energy range considered here.

[1] Chapter 3 is based on the published paper of Papadopoulos et al. Microdosimetry Study of Proton Quality Factor Using Analytic Model Calculations. ***Applied Sciences*** 12:8950, 19pp (2022).

## Generalized Analytic Microdosimetric Models

## The Xapsos et al. 1994 model

In this model (hereafter denoted as "X94")(144), the energy deposition inside the target volume is classified as either "direct or "indirect." The former is related to the energy deposition by a primary ion crossing the target, whereas the latter is related to the energy deposition by δ-rays produced by an ion passing outside the target(54,144). The contribution of direct (ion) and indirect (δ-rays) energy deposition events varies with the kinetic energy of the ion and the diameter of the target volume. For example, with increasing ion energy and/or volume size, the indirect contribution is enhanced by δ-rays become more energetic and/or have a higher probability to reach the target volume.

To a first approximation, when an ion crosses a volume, the energy deposited is proportional to the product of LET and the mean chord length $\bar{l}$. However, for insufficient (e.g., approaching the nanometer scale), energy loss-straggling, path length fluctuations and energy carried out of the volume by δ-rays may become pronounced. It can be shown that the $y_D$ can be calculated as a function of distributions of LET, path length and single-collision energy-transfer(52). The corresponding expressions for the direct (ion, $y_{D,dir}$), indirect (δ-ray, $y_{D,ind}$) and total events are(144):

$$y_{D,dir} = \frac{1}{\bar{l}}\left(f_{ion} L_{D,ion} l_{D,ion} + \delta_{2,ion}\right), \tag{24}$$

$$y_{D,ind} = \frac{1}{\bar{l}}\left(L_{D,el} l_{D,el} + \delta_{2,el}\right), \tag{25}$$

$$y_D = f_{ion} y_{D,dir} + (1 - f_{ion}) y_{D,ind}, \tag{26}$$

where $f_{ion}$ is the fraction of energy deposited in the site by the primary ion, the index 'D' refers to the dose weighted average for the LET (L) and chord length (l) quantities. The calculation of each parameter ($f_{ion}$, $\delta_{2,ion}$, $\delta_{2,el}$, $L_{D,ion}$, $L_{D,el}$, $l_{D,ion}$, $l_{D,el}$) entering the above expressions, Eqs. (24)– (26), is discussed below.

When an ion traverses a site, it deposits energy and generates δ-rays (i.e., secondary electrons) that, subsequently, may deposit only a fraction (or all) of their energy inside the site. The fraction of ion energy that is retained inside the site may be described analytically by the spatially restricted LET. Then, it may be shown that(156):

$$f_{ion} = \frac{\ln\left[\frac{T_{el,max}(\Delta + \Delta 1 + \Delta 2)}{I^2}\right]}{2\ln\left[\frac{T_{el,max}}{I}\right]}, \tag{27}$$

where I is the mean excitation energy of the stopping-power of the medium(101), and $T_{el,max}$ is the maximum energy that an ion can transfer to a secondary electron (δ-ray):

$$T_{el,max} = 2.179\, T_{ion}, \tag{28}$$

with $T_{ion}$ expressed in (MeV/amu) and $T_{el,max}$ in keV. Δ is the energy of an electron with range equal to the mean chord length of the site, Δ1 accounts for the energy transferred by escaping secondary electrons to the site and Δ2 is the electronic excitation or ionization energy present

in the atoms after the interaction with the ion (i.e., binding effects) when secondary electrons migrate outside the volume. It holds that(156):

$$(\Delta 1 + \Delta 2) = \left(1 - \frac{\Delta}{T_{el,max}}\right)(I + \Delta). \quad (29)$$

The dose-weighted mean-energy deposited in the site by ions in a single inelastic collision ($\delta_{2,ion}$) is obtained from(144):

$$\delta_{2,ion} = \frac{Min[\,\Delta, T_{el,max}]}{2\ln[\frac{Min[\Delta, T_{el,max}]}{I}]}, Min[\Delta, T_{el,max}] \leq 1keV, \quad (30)$$

$$\delta_{2,ion} = A\Delta^B, \quad Min[\Delta, T_{el,max}] \geq 1keV, \quad (31)$$

with $\delta_{2,ion}$ in units of keV. For protons in water vapor, the values A = 0.190 and B = 0.621 have been suggested. The corresponding expressions for electrons are(52):

$$\delta_{2,el} = \frac{0.2105\bar{T}_{el}}{\ln[\frac{\bar{T}_{el}}{2I}] - 0.193}, \qquad \bar{T}_{el} \geq 2\ keV, \quad (32)$$

$$\delta_{2,el} = A\bar{T}_{el}^{\ B}, \qquad \bar{T}_{el} \leq 2\ keV, \quad (33)$$

with parameters A = 0.114 and B = 0.591 for water vapor. Note that the condition Min[Δ, $T_{el,max}$] for the ion case, Eq. (32), is now replaced by $T_{el}/2$, which is the maximum energy transfer in an electron-electron collision. $T_{el}$ is the average energy of secondary electrons, which may be represented by the fitted expression(52):

$$\bar{T}_{el} = 1.25T_{ion}^{0.229}\Delta^{0.778+0.00142T_{ion}}, \quad (34)$$

With $\bar{T}_{el}$ and Δ in keV and $T_{ion}$ in MeV/amu. The dose-averaged LET ($L_{D,ion}$ and $L_{D,el}$) in Eqs. (24) and (25) equal the ratio $L^2/L$. For the case of monoenergetic ions that cross the volume with almost constant LET, the ratio $L^2/L$ reduces to LET, i.e., $L_{D,ion} = LET_{ion}$. For electrons, the dose-averaged LET can differ significantly for different volumes and energies. It can be shown that(144):

$$\bar{L}_{D,el} = \begin{cases} 0.985\ LET_{el}(\Delta + 0.02), & \Delta \leq I \\ 0.925 LET_{el}(\Delta + 0.05), & \Delta \geq I \end{cases}. \quad (35)$$

Finally, the path length moment ratio ($l_{D,ion}$, $l_{D,el}$) for a sphere is equal to 3d/4 for both ion and electron.
Eqs. (27)–(35) can then be implemented into Equations (24) and (25) to calculate $y_D$ from Eq. (26).

## Xapsos et al. 1996 model

This model (hereafter denoted as "X96") treats only direct events but uses an explicit description of ion's energy-loss straggling. Specifically, the probability density function, $p_{x,l}$, for energy deposition *x* along an ion's path length l (for a single traversal), is approximated by a log-normal distribution(53):

$$p_{x,l} = \frac{1}{\sqrt{2\pi}\sigma_l x} \mathrm{Exp}[-\left((\ln x - \mu_l)/\sqrt{2}\sigma_l\right)^2], \quad (36)$$

where $\mu_l$ and $\sigma_l$ are the mean and variance of the distribution, respectively. They can be calculated from(53):

$$\mu_l = \ln(\bar{x}_{ion}) - 0.5\sigma_l^2, \quad (37)$$

$$\sigma_l = \sqrt{\ln(1+V)}, \quad (38)$$

where $\bar{x}_{ion}$ is the mean energy deposited in the site for $l$ equal to the path length of the ion and $V$is obtained as a sum of various contributing terms(23,53):

$$V = V_{str} + V_l + V_L + V_F + V_L V_s. \quad (39)$$

The terms in Eq. (39) are as follows: $V_{str} = \delta_{2,ion}/\bar{\varepsilon}_{ion}$is the relative variance of energy-loss straggling where $\delta_{2,ion}$ is taken from Eqs. (30-31) and $\bar{x}_{ion} = f_{ion}\ LET_{ion} l$ is the mean energy deposited in the target volume as a function of ion's path length (l), $V_l$ is the relative variance of ion's path length distribution, $V_L$ is the relative variance of ion's LET distribution, and $V_F$ is the relative variance of Fano fluctuations. For monoenergetic ions and neglecting the Fano fluctuations, Eq. (39) reduces to

$$V = V_{str} + V_s. \quad (40)$$

Then, the total probability density function, $f_x$ for energy deposition x, is the convolution of the straggling distribution $p_{x,s}$ and the probability density function of the particle's path length inside the site, $c_s(53)$:

$$f_x = \int p_{x,l} c_l \, ds. \quad (41)$$

For a sphere, and assuming that ions travel in straight lines, $c_s = 2s/d^2(129)$.

## The Combined Xapsos Models

The extension of the X96 model to the indirect (electron) events may be developed following the X94 model (the combined model is hereafter denoted as "Xcom"). The relative variance of electron events may be calculated from Equation (40), with the addition of a term related to the relative variance of LET ($V_L$), with $V_{str} = \delta_{2,el}/\bar{\varepsilon}_{el}$, where $\delta_{2,el}$ is obtained from Eqs. (32) and (33) and $\bar{\varepsilon}_{el} = LET_{el} \times \bar{l}$, where $LET_{el}$ is the mean slowed-down electron LET and $\bar{l}$ is the mean chord length of the electrons. Then, the combined probability density for energy distribution is given by(55,151):

$$f_x = P f_{x,ion} + (1-P) f_{x,el}, \quad (42)$$

where P is the fraction of direct events. The fraction of indirect events $(1-P)$ is given by(146,151):

$$(1-\mathrm{P}) = \frac{(1-f_{ion})\bar{x}_{ion}}{f_{ion}\bar{x}_{el}+(1-f_{ion})\bar{x}_{ion}}, \quad (43)$$

where $x_{el}$ is the mean energy deposited in the site, in an analogous interpretation as $x_{ion}$.

## The Combined Xapsos-Olko Model

In this model (hereafter denoted as "XO"), Xcom is used for the calculation of energy deposition and the microdosimetric spectra of the ion (direct) and electron (indirect) events. Specifically, to calculate the ion (direct events) energy deposition, one uses the Eqs. (27)–(31) and (17)–(24) from the 'X96' model. For the electron energy deposition (indirect events), one uses Eqs. (32) and (33) and Eqs. (36)–(43) for energy-loss straggling, relative variance, and the log-normal process of energy deposition, respectively. However, contrary to the Xcom model, in the XO model one uses the full secondary electron spectrum which is calculated using the following expressions(146):

$$\bar{L}_{el} = \frac{\int_{3W}^{T_{el,max}} L_{el}(K)\varphi(K)dK}{\int_{3W}^{T_{emax}} \varphi(K)dK}, \quad (44)$$

where W is the energy required for an ion-electron hole. φ(K) is the degraded electron spectra given by(146):

$$\varphi(T) = \frac{\int_{T}^{T_{el,max}} T'^{-2}dT'}{L_{el}(T)}. \quad (45)$$

### Modifications of Model Parameters

To calculate the microdosimetric parameter $y_D$ using the above models (X94, Xcom, XO), we must first establish the needed material parameters, namely the mean excitation energy of stopping-power theory (I) (entering Eqs. (27), (29) and (30)), the constants A and B (of Eqs. (30) and (32)) and the cut-off energy Δ. The choice of the cut off energy Δ is defined by the electron energy that corresponds to a penetration depth equal to the mean chord length l = 2/3d of the target size. For reasons of availability, the original implementation of X94 and X96 models used data for condensed water vapor. Vapor water refers to the so-called gas phase approximation, whereby interaction cross sections for water vapor are extrapolated to unit density medium. Therefore, vapor and liquid water share the same density (and also both temperature and pressure values) but differ upon the underlying physics of their interaction cross sections. Specifically, vapor water cross sections do not account for intermolecular effects (screening, etc.) which are considered (according to the theoretical model adopted) in the case of liquid water. To examine the degree of which the results are sensitive to the parameters of the water medium, we here deduced the corresponding parameters for liquid water. Table 5 summarizes the values of the model parameters used in the present work. The cut-off energy Δ for the different sphere diameters was estimated from electron penetration-depth values for liquid water obtained from Geant4-DNA MC simulations using the latest electron physics list (Option 4) for liquid water(157). The corresponding values for condensed water vapour were determined from the analytic fitting formulas for the electron penetration-depth obtained by the MC4 code(158). For the calculation of the material constants, A and B, for electrons and protons, we followed the method described in Xapsos et al. (1994), whereby Eqs. (11) and (12) and their derivatives, with respect to Min[Δ, $T_{el,max}$] = Δ, are continuous at a Δ value that equals twice the K-shell binding energy of water (2 × 540 eV = 1.08 keV).

**Table 5.** Physical model parameters used in the present work for liquid and vapor water (both at unit density).

| Physical Parameters | Liquid Water | Vapor Water | Reference |
|---|---|---|---|
| **I-value (keV)** | 0.078 | 0.0716 | Liquid: ICRU Report 90(101)<br>Vapor: ICRU Report16(159) |
| **Δ-cut off electron energy (keV)** | 11.0 (d=3μm)<br>5.62 (d=1 μm)<br>1.37 (d=0.1 μm)<br>0.184 (d=0.01 μm) | 11.1 (d=3μm)<br>5.93 (d=1μm)<br>1.50 (d=0.1 μm)<br>0.288 (d=0.01 μm) | Liquid: Kyriakou et al. (2016)(157)<br>Vapor: Emfietzoglou et al. (2008)(158) |
| **δ2-energy-weighted mean energy deposited inside the target per collision (keV)** | Protons: A=0.195, B=0.610 | Protons: A=0.190, B=0.620 | Liquid: Our fit<br>Vapor : Xapsos et al. (1994)(144) |
| | Electrons: A=0.121, B=0.577 | Electrons: A=0.114, B=0.591 | |

**Results**

The quality factor (Q) is a relative parameter that quantifies the risk of stochastic effects (e.g., carcinogenesis) of different ionizing radiations in comparison to a predefined "reference" radiation. For convenience, we used the proton energy of 100 MeV here as the reference radiation (i.e., the quality factor of 100 MeV proton was set to unity). This choice is convenient for the direct comparison of Q calculated by analytic models and Monte-Carlo data, since the latter data used in this work are only available up to 100 MeV. None of the conclusions of the work would have changed if another proton energy was chosen.

Figure 4 presents $y_D$ values for a liquid water sphere of 1 μm diameter over the proton energy range of 1–250 MeV. Proton beams with initial energy between 50 and 250 MeV are increasingly used in cancer radiotherapy. For space applications, protons in the Van Allen belts reach up to 400 MeV. After these protons interact with spacecraft shielding, they slow down. Those capable of penetrating within the spacecraft reach the astronauts with energies well below 300 MeV. Moreover, protons in the energy range below 30 MeV make up the Bragg peak region where the Q (and the carcinogenic risk) becomes maximum. The calculated values are from the different analytical models examined in the present work (X94, Xcom, XO), as well as published MC data by Geant4-DNA(1) and TEPC simulations by the PITS99-KURBUC codes(28). For better visualisation, the $y_D$ values in the energy range of 1–100 MeV are also presented logarithmically in the inset of Figure 4. Note that the available Geant4-DNA and TEPC simulation data are limited up to 100 MeV.

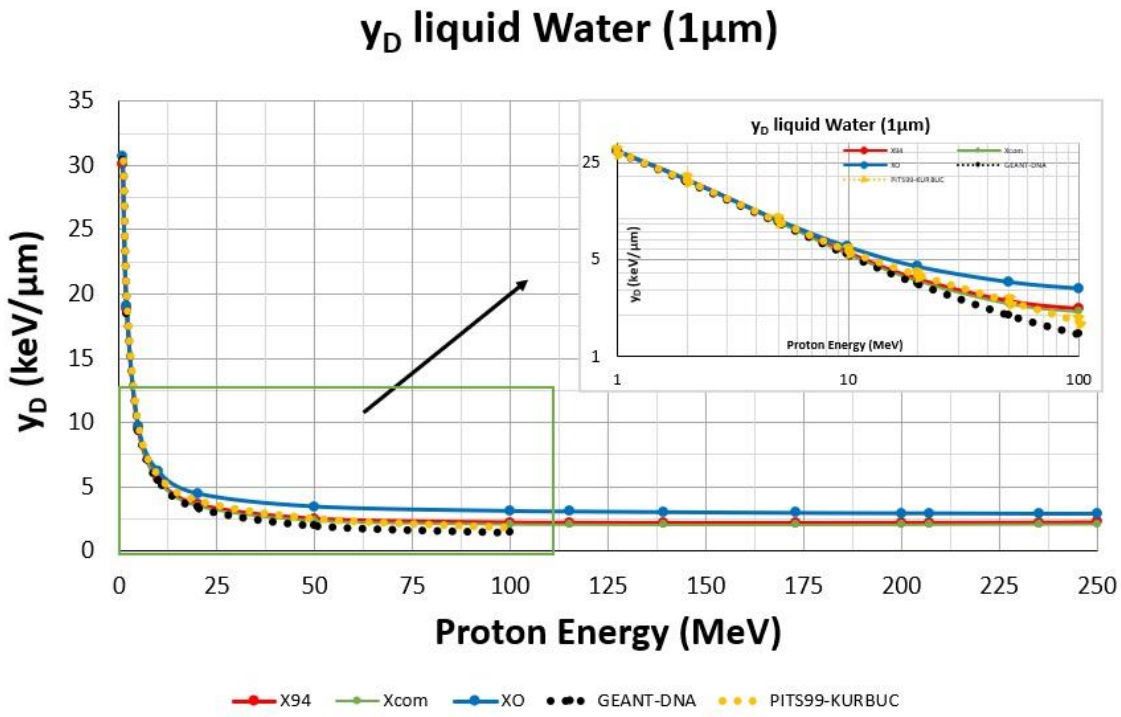


**Figure 4.** $y_D$ values for a liquid water sphere of 1 µm diameter as a function of proton energy calculated by the different analytic models examined (X94, Xcom, XO), and Monte Carlo data by the Geant4-DNA code and TEPC simulations with PITS99-KURBUC. Inset: Logarithmical presentation of the $y_D$ values for the energy range 1-100 MeV.

Subsequently, the $y_D$ values depicted in Figure 4 along with the full microdosimetric spectra *f* (*y*) and d(y) were used to determine the corresponding proton Q based on the TDRA and ICRU Report 40 expressions Equations (20) and (23), respectively. Figure 5 presents the calculated Q values for the different analytic models (X94, XO, Xcom) and MC data from the Geant4-DNA and TEPC simulation. The LET-based Q values recommended by ICRP Report 60 are also presented for comparison. Figure 6 presents the differences of the microdosimetric-based Q values (TDRA, ICRU Report 40) against the LET-based ICRP Report 60 recommendations.

Figure 7 presents $y_D$ values for liquid water spheres of different diameters (10, 100, 1000 nm). The calculated values were from the Xcom analytical model (combination of Xapsos et al. 1994 and Xapsos et al. 1996 models) and the MC data for the different spheres were taken from Geant4-DNA. The Xcom model represents the best available analytic model for calculations of *y* spectra. It combines both the energy deposition and its fluctuations from ion (direct) and electron (indirect) events in the target site, as well as the effects of the finite range of δ-rays. A form of this model has been utilised for determining *y* spectra in TEPC measurements. Similar to Figure 4, the available Geant4-DNA data for these spheres are limited up to 100 MeV.

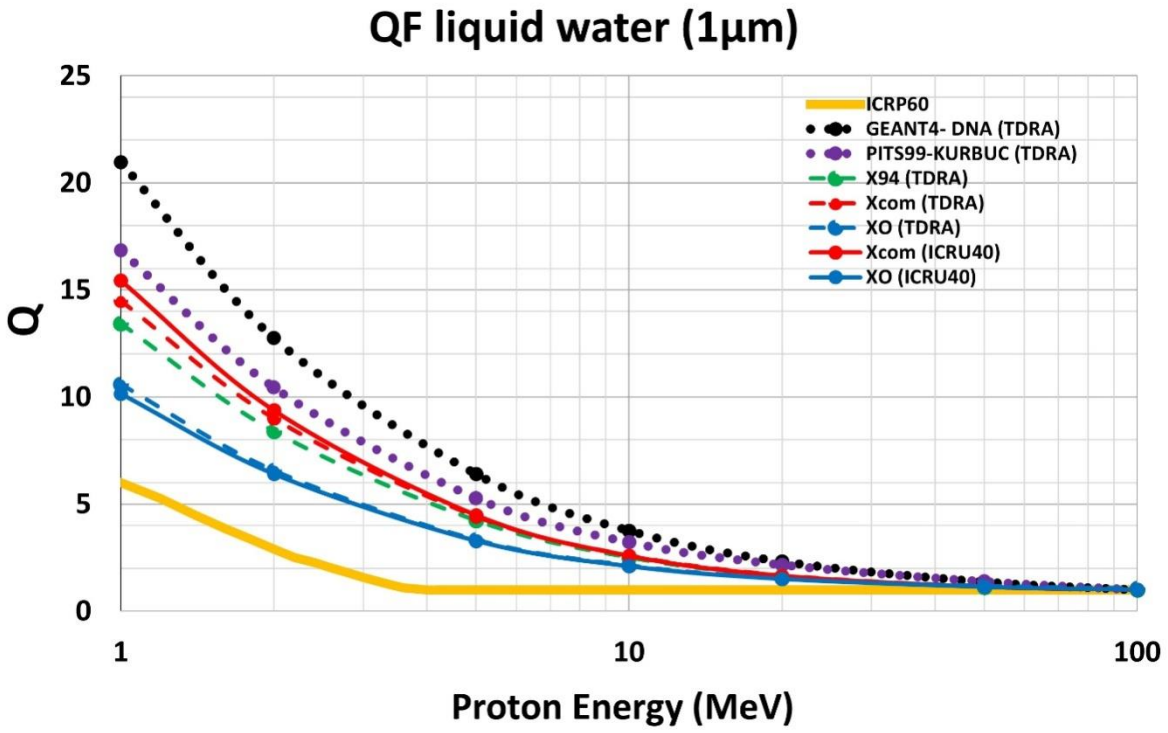


**Figure 5.** Energy variation of the proton quality factor (Q) based on different microdosimetric approaches (TDRA, ICRU Report 40) with input data from both analytic models (X94, XO, Xcom) and Monte Carlo codes (Geant4-DNA, TEPC simulations by PITS99-KURBUC). The microdosimetric data pertain to a liquid water sphere of 1 µm diameter. The LET-based Q values recommended by the ICRP Report 60 are also shown for comparison.

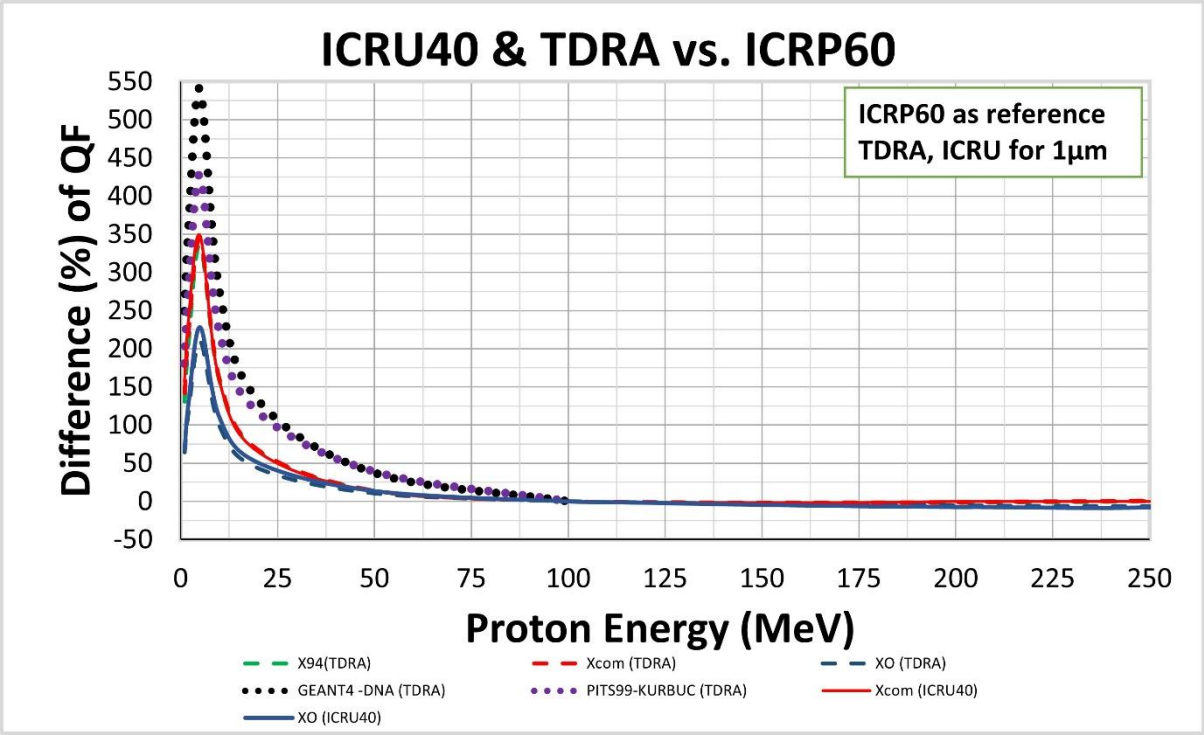


**Figure 6.** Difference (%) of TDRA and ICRU Report 40 predictions for the proton Quality Factor (Q) with input data calculated by different analytic models (X94, XO, Xcom) and Monte-Carlo codes (Geant4-DNA, TEPC simulations by PITS99-KURBUC). All microdosimetric calculations pertain to

liquid water sphere of 1 μm diameter. The LET-based Q values recommended by ICRP Report 60 were used as baseline for the comparison.

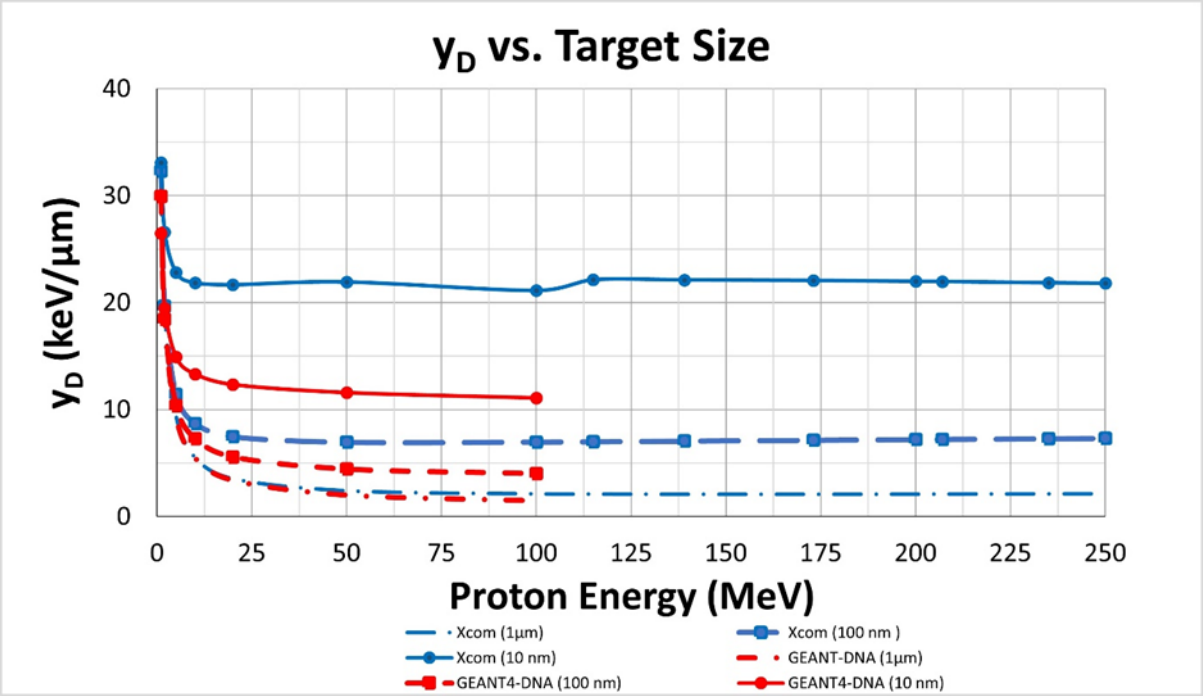


**Figure 7.** $y_D$ values as a function of proton energy for liquid water spherical volumes of 10, 100 and 1000 nm diameter calculated by the Xcom analytic model (blue lines) and the Monte-Carlo data of Geant4-DNA (red lines).

Using the $y_D$ values of Figure 7, we present in Figure 8 the corresponding quality factor (Q) for sphere diameters of 100 nm and 10 nm using the TDRA approach, Eq. (20), over the proton energy range of 1–100 MeV. The LET-based Q values from the ICRP Report 60 recommendations are also shown for comparison. In Fig. 9, the differences (%) of the TDRA-based quality factor (Q) for 100 nm and 10 nm calculated by the Xcom analytic model and the Geant4-DNA MC data are presented with the LET-based Q values of ICRP Report 60 recommendations used as baseline.

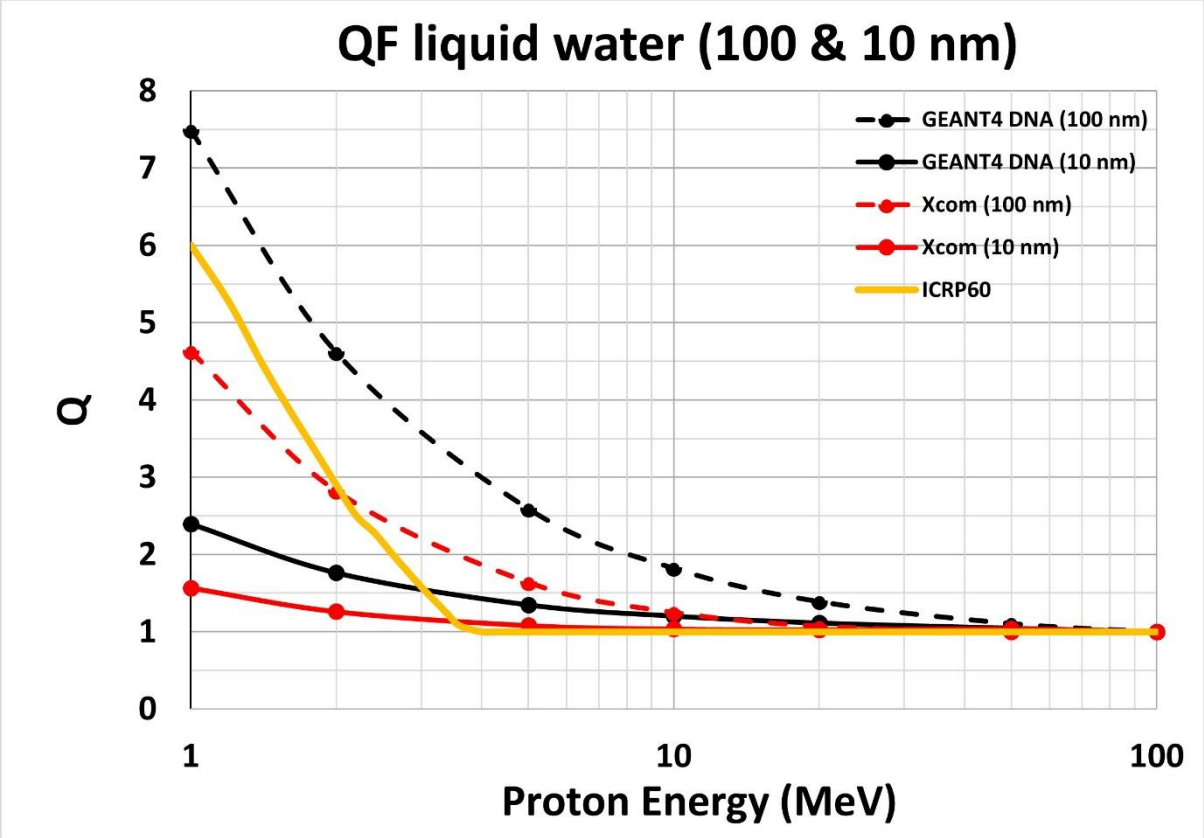


**Figure 8.** Energy variation of the proton quality factor (Q) based on the TDRA approach with input data from the Xcom analytic model (red colour) and the Geant4-DNA Monte Carlo code(1) (black colour). The microdosimetric data pertain to liquid water spheres of 0.1 and 0.01 μm diameter. The LET-based Q values recommended by ICRP Report 60 are also shown for comparison (dark yellow colour).

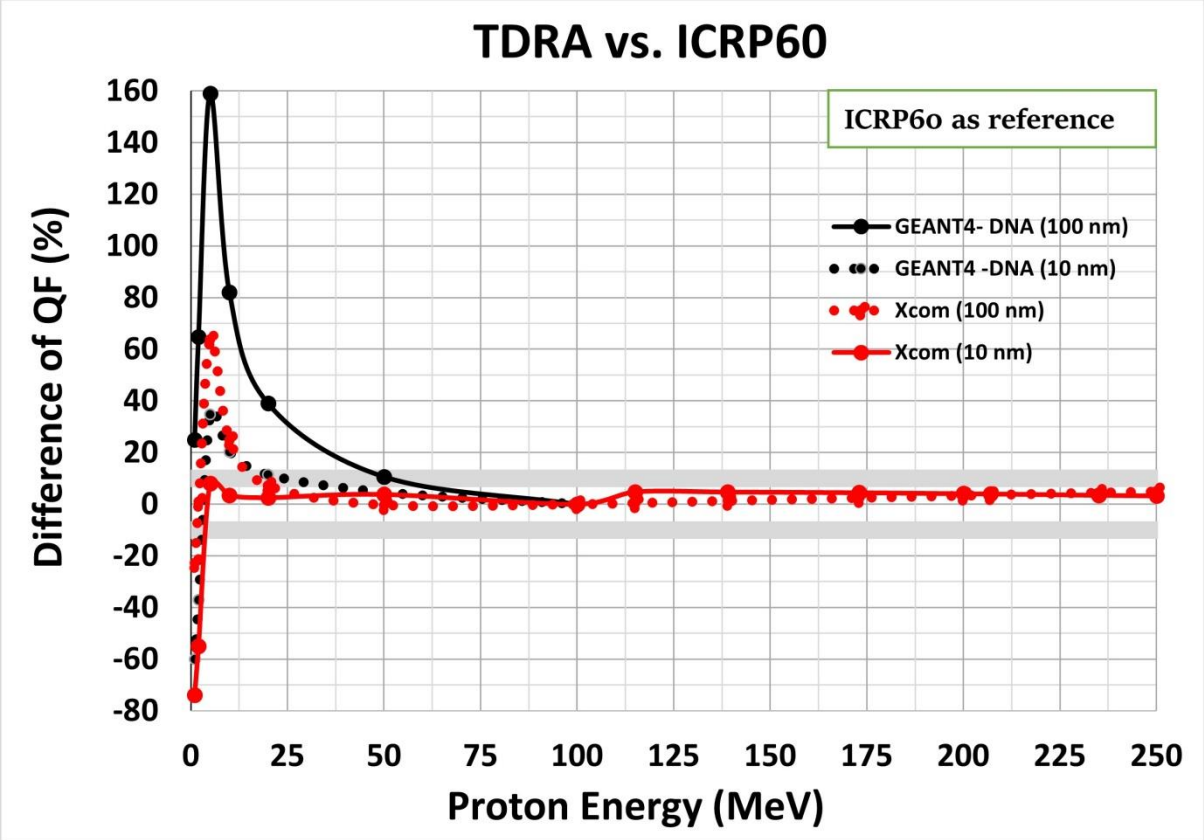


**Figure 9.** Difference (%) of the TDRA-based Q calculated by the Xcom analytic model and the Geant4-DNA Monte-Carlo data for 0.1 and 0.01 µm liquid water spheres. The LET-based Q values recommended by ICRP Report 60 were used as baseline for comparison.

Based on the results of Figures 5 and 8, the sensitivity of proton Q with respect to sphere diameter is depicted in Figure 9 with the Q value at 1 µm diameter used as baseline for the comparison

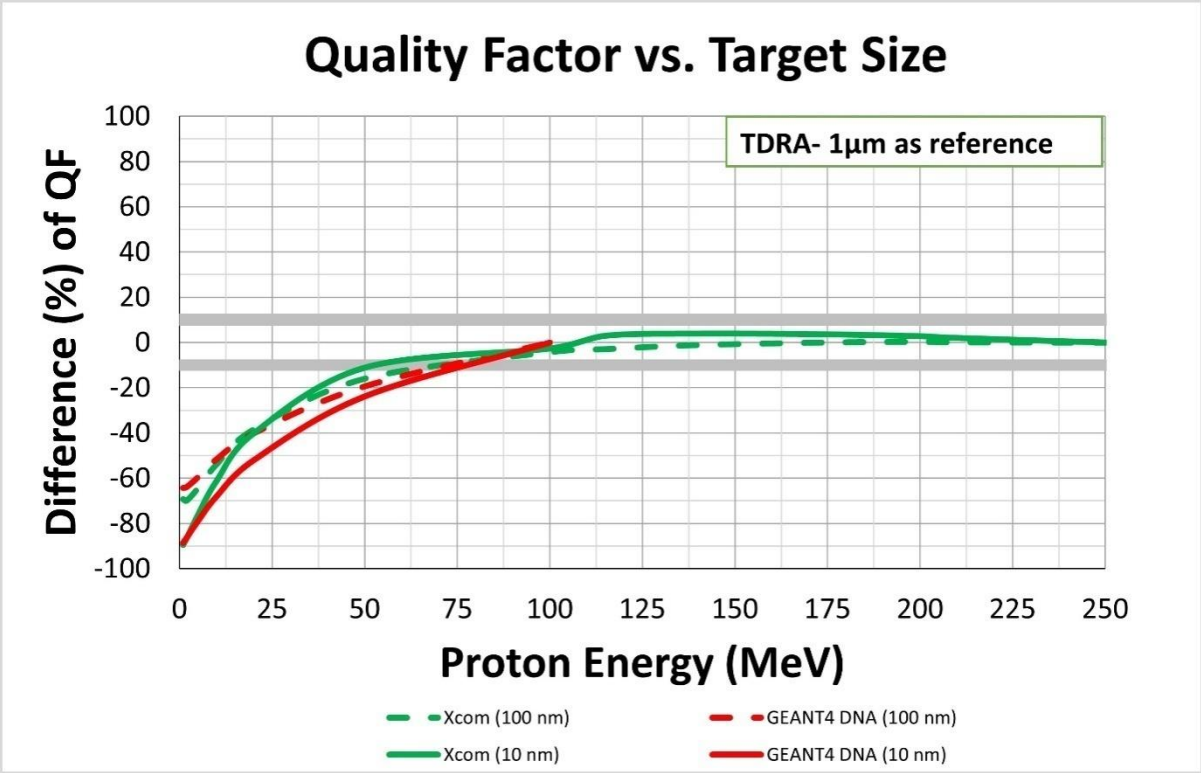


**Figure 10.** Difference (%) of TDRA-based proton Quality Factor (Q) calculated by the Xcom analytic model (*green colour*) and the Geant4-DNA Monte Carlo data (*red colour*). The corresponding results for 1 μm were used as baseline for the comparison.

Figures 11 and 12 show the differences of $y_D$ and corresponding Q, respectively, between gaseous and liquid water (both at unit density) based on the examined analytic models (X94, Xcom and XO) with input parameters according to Table 5. Results are shown for spherical volumes with 3000, 1000, 100 and 10 nm diameter and for proton energies from 1 to 250 MeV. At each sphere size, the results of liquid water were used as baseline for the comparison.

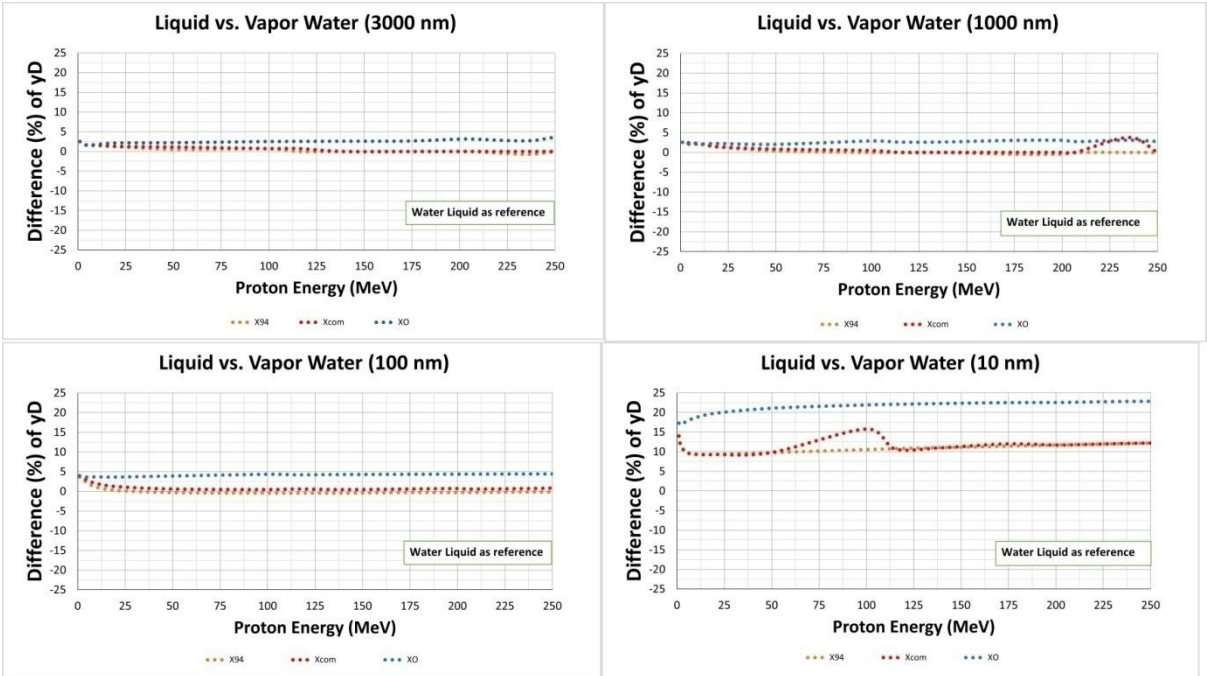


**Figure 11.** Difference (%) of $y_D$ for unit-density gaseous and liquid water spherical volumes of

different diameter (10, 100, 1000, 3000 nm) calculated by the different analytic models. The liquid water values were used as baseline for the comparison.

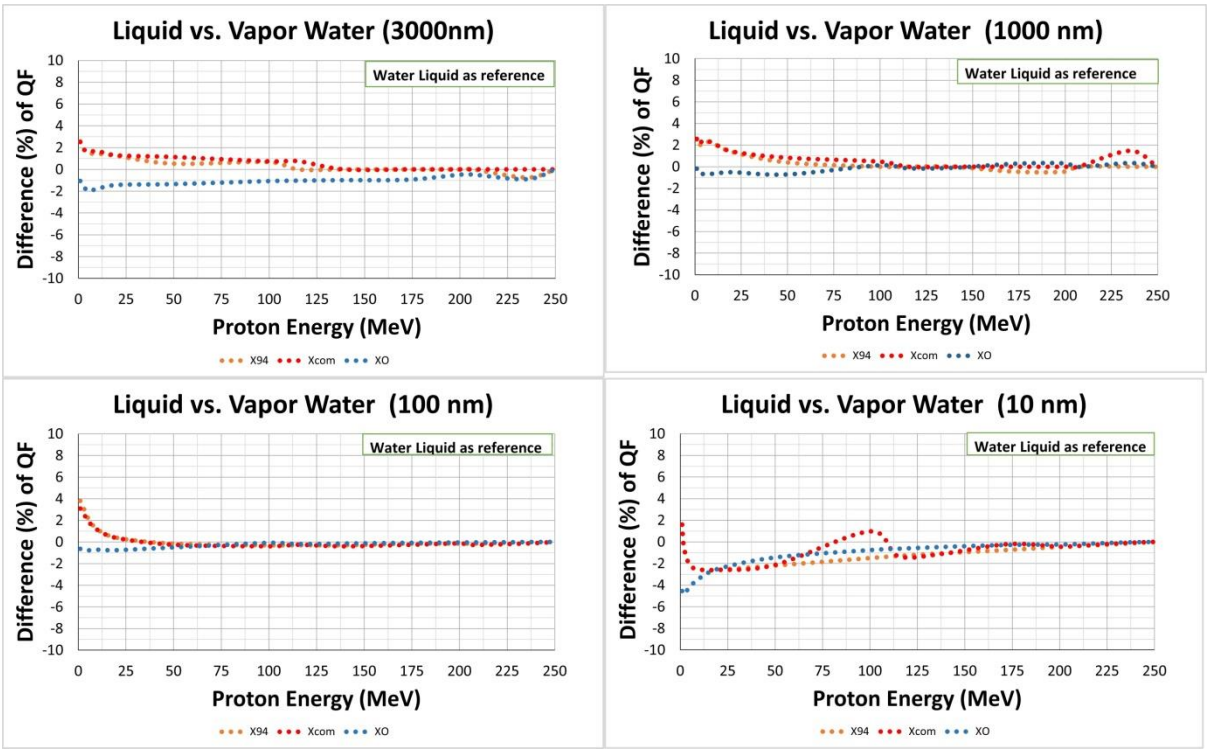


**Figure 12.** Difference (%) of TDRA-based proton Q between unit density gaseous and liquid water spheres of varying diameter calculated by the different analytic models. The liquid water values were used as baseline for comparison.

## Discussion

As it can be seen from Figure 4, the calculated $y_D$ values for 1μm target size and for proton energies 1–250 MeV calculated by the different analytical models (X94, Xcom, XO) followed the same trend over the whole energy range. The difference between the X94 and Xcom models reached up to 10%, while the XO model was consistently higher by up to 40–50% in the energy range of 50–250 MeV. This is due to the different calculation of the deposited energy of secondary electrons that affects both the indirect (electron) events and the δ-ray escape from the volume. The secondary electron spectrum is treated differently in the XO and Xcom models; specifically, in the XO model, the full slowing-down spectrum is used. For the 1 μm sphere, the mean LET of the secondary electrons calculated by the XO model inside the sphere target is larger than the mean LET calculated by the Xcom model. Higher LET means more energy deposited inside the sphere, so there was a slight increase in the total $y_D$ value for the XO model. The proton energy deposition is treated similarly in both models. Unfortunately, there are no updated references for these discrepancies among the models except the one already cited in out text(53,144,146,160). To our knowledge, the present work represents the first time that all models were combined and compared with Q calculations. Importantly, the MC literature data (Geant4-DNA, PITS99-KURBUC) on proton lineal energy has followed similar trends with the analytic calculations. Specifically, the differences between the analytical models (X94 and Xcom) and the MC data (Geant4-DNA, PITS99-KURBUC) did not exceed 10% up to 50 MeV, increasing up to 15–30% in the energy range of 50–100 MeV. The magnitude of this difference is comparable to the difference among the MC data (i.e., Geant4-DNA vs. PITS99-KURBUC), which is up to 10% for proton energies 1–50 MeV and up to

25% for the 50–100 MeV range. Extensive information about the physical models and assumptions made in the MC simulations by Geant4-DNA and PITS99-KURBUC codes can be found in the literature(1,28).

The comparison of the microdosimetric-based proton Q values (using TDRA and ICRU Report 40 methodologies, both at 1 μm sphere) against the LET-based ICRP Report 60 recommendations showed noticeable differences (>10–20%) below about 50–75 MeV, reaching a factor of 2–3 at ~5 MeV (see Figures 5 and 6). It is noteworthy that these differences increased further when MC literature data from Geant4-DNA and TEPC simulations from PITS99-KURBUC were used to calculate Q by the TDRA. In particular, at energies relevant to the Bragg peak region (<20–30 MeV), the deviations of both the analytic and MC microdosimetric-based Q values from ICRP Report 60 agreed above 20–50%.
It follows from Figure 7 that, as the sphere diameter decreased to 100 and 10 nm, the differences in the $y_D$ values between the analytical model calculations and the Geant4-DNA MC data became more pronounced at lower energies (~5–10 MeV). This is expected given that at smaller volumes, the details of how the energy-loss processes (including the effect of straggling and δ-ray production and transport) are considered in each approach (analytical models vs. MC simulations) become more important for the energy imparted to the site. The present models (Xcom, X94, XO) are generally recommended for diameters greater than several nanometers, specifically for diameters much larger than the penetration range of electrons with energy equal to the mean excitation energy of the medium (I) which, in this case, translates to $d > 2$ nm. In general, for space applications, diameters in the range of 1000–3000 nm are most relevant to experimental TEPC measurements (e.g., ISS). In addition, several studies of proton (and carbon) RBE in hadron therapy have suggested that $y_D$ should be determined in spheres with 10–15 nm diameter(27). The present work reveals that the results of analytic models (and MC simulations) already diverge below 100 nm. Therefore, even larger discrepancies are expected for spheres with $d < 10$ nm. The influence of sphere size on the TDRA Q values seem to be significant (>10%) only below ~50 MeV (see Figures 8–10). The $y_D$ values of high-energy protons were found to be sensitive to the choice of the sphere size due to the contribution of the energetic secondary electrons (δ-rays). Specifically, for high-energy protons, there are more indirect events (Eq. (43)), and the mean LET of these electrons is often equal to or even larger than that of the high-energy proton, resulting in a strong increase in $y_D$. Therefore, when calculating the TDRA quality factor for the low-energy protons, by normalizing to a reference radiation (Eq. (20))—which, in this study, is a high-energy proton (100 MeV)—it results in a large variation of Q. Calculations of the Q based on ICRU Report 40 have also been performed for nanometer targets (10–100 nm). However, only the values for 1 μm are shown since Eq. (23) is deduced for this particular sphere size. It is somewhat surprising that with decreasing sphere size (from 1 μm to 100 and 10 nm), the Q values by TDRA are in better agreement with the ICRP Report 60 recommendations than the Q values by TDRA based on the conventional 1 μm sphere. On the other hand, larger sphere diameters (>1 μm) were found to yield even higher deviations from ICRP Report 60 (not presented).

The present work is, to our knowledge, the first study that systematically combines and compares the most established analytical microdosimetric models for proton Q calculations. Proton quality factors are continuously used by various space organizations and the radiotherapy community to assess the carcinogenic risk of irradiated individuals, e.g., for long-duration manned missions and/or in the context of the organs at risks (OAR) in proton therapy, respectively. Although LET-based calculations of Q are generally preferred in practical applications due to the availability of LET values for various ions over a wide energy range, it is recognized that microdosimetric-based calculations offer a scientifically sounder approach (ICRU Report 40). However, the difficulties of working with microdosimetric quantities,

which are stochastic in nature, has led to a situation where experimental microdosimetric measurements with TEPC are often approximated by some average LET values before their practical implementation. The combination of available analytic models discussed in the present work further supports the use of microdosimetric-based approaches to proton quality factor problems as a viable alternative to LET-based approaches. An important finding of the present study is the energy range over which LET-based and y-based proton Q values may differ substantially. Specifically, the low-energy range (1–50 MeV) corresponds to protons that comprise the Bragg peak region, where the absorbed dose becomes maximum, and variation of Q are expected to have a major impact in absolute terms. It is also relevant to protons that penetrate a typical astronaut spacesuit (>10 MeV) during an Extra Vehicular Activity (EVA) or those generated (as secondary radiation) inside the astronaut's body during a deep space mission. It should be noted that both the European Space Agency (ESA) and the Canadian Space Agency (CSA) presently adopt the LET-based ICRP Report 60 recommendations for Q. A common concern in microdosimetric calculations at sub-micron volumes is the influence of the condensed phase, i.e., the difference of microdosimetric spectra between gaseous and liquid water (at the same density). The results of Figures 11 and 12 clearly show that, although such effects may influence the analytical model calculations of $y_D$ by up to 20% for the smallest sphere examined (10 nm diameter), the end effect on Q is negligible (<5%).

## Conclusions

Different analytical microdosimetric models have been used and combined for calculating the microdosimetric quantity $y_D$ for target spheres of various sizes. The lineal energy spectra were subsequently used to study the variation of the proton Q over the energy range of 1–250 MeV based on the TDRA and ICRU Report 40 microdosimetric methodologies. The microdosimetric-based Q values reveal that the LET-based ICRP Report 60 recommendations may significantly underestimate Q for proton energies below ~50–100 MeV. Similar trends were found when MC track-structure literature data were used as input to the calculations. The microdosimetric-based Q values for low-energy protons were also found to be sensitive to the choice of the sphere size. Finally, condensed-phase effects in the analytic model parameters had only a weak influence on Q in the examined range of proton energies and sphere sizes. Although the general trend of the variation of Q with proton energy revealed by the present analytic model calculations is supported by the MC literature data used in this work, future research will include a systematic comparison and validation of lineal energy spectra and subsequent calculations of Q based on new MC data with the latest versions of Geant4-DNA and PHITS track structure codes which make use of different and updated physics models.

# Chapter 4

**Summary**[2]

In the present work, the average Q of GCR for different mission scenarios is calculated using a modified version of the microdosimetric Theory of Dual Radiation Action (TDRA). NASA's OLTARIS platform is utilized to generate the radiation environment behind different aluminium shielding (0-30 g/cm$^2$) for a typical mission scenario in low-earth orbit (LEO) and in deep space. The microdosimetric lineal energy spectra of ions ($Z \geq 1$) in 1 μm liquid water spheres are calculated by a generalised analytical model which considers energy-loss fluctuations and δ-ray transport inside the irradiated medium. The present TDRA-based Q values for the LEO and deep space missions were found to differ by up to 10% and 14% from the corresponding ICRP-based Q-values and up to 3% and 6% from NASA's Q-model. In addition, they are in good agreement with the Q values measured in the International Space Station (ISS) and by the Mars Science Laboratory (MSL) Radiation Assessment Detector (RAD) which represent, respectively, a LEO and deep space orbit.

[2] Chapter 4 is based on the published paper of Papadopoulos et al. Space radiation quality factor for Galactic Cosmic Rays and typical space mission scenarios using a microdosimetric approach. ***Radiation and Environmental Biophysics*** 62:221-234 (2023).

**OLTARIS software**

For the assessment of the radiation environment in space and the calculation of the average Q for specific missions, NASA has developed the online platform OLTARIS (161). Two space environments have been examined in the present work. The first was studied inside Earth's magnetic field, in a circular LEO with altitude 400 km and inclination 51.6°, simulating the orbit of the International Space Station (ISS). The second was an orbit at deep space (1 AU). The GCR spectrum in an extended energy range of 1 MeV/amu-1 GeV/amu has been calculated in this work using the Badhwar-O'Neill 2020 model(162) (incorporated to OLTARIS), using 1977 Solar Minimum conditions. The initial spectrum of the GCR both for LEO (ISS) and deep space that was transported through aluminium shielding was 1 MeV/amu-1000 GeV/amu, which is the default energy range of the OLTARIS platform. After transportation and for the estimation of the Q-values, we used the energy range of 1MeV-1GeV since the analytical microdosimetric model used for calculating the $y_D$ values does not extend to energies greater than 1 GeV. This limitation affects our calculations by less than 2-3%. This was deduced by extending our calculations to ion energies beyond 1 GeV assuming a constant $y_D$ value equal to that at 1 GeV (since this assumption overestimates the true $y_D$ beyond 1 GeV, it offers an upper limit to the error made in our Q values by cutting the spectrum at 1 GeV). The Q values have been calculated for each ion without its isotopes in order to be consistent with our LET calculations. GCR flux from 1 MeV-1 GeV has been obtained behind aluminium thicknesses of 0 g/cm$^2$ to 30 g/cm$^2$ – both for LEO (ISS orbit) and deep space (1 AU). Table 6 shows the orbital characteristics of the specific mission scenarios considered in this work.

**Table 6.** Orbital parameters for the two different space scenarios used in OLTARIS

| Orbital Parameters | Low Earth Orbit (ISS) | Deep Space |
|---|---|---|
| **Altitude** | ~400 km | ~1 AU |
| **Inclination** | ~51.6° | - |
| **Solar Cycle** | 1977 Solar Minimum | 1977 Solar Minimum |
| **Model** | GCR Badhwar-O Neil 2020 | GCR Badhwar-O Neil 2020 |
| **Shielding** | Aluminium 0-30 g/cm$^2$ | Aluminium 0-30 g/cm$^2$ |

**Mission Quality Factor**

The mission Q value (GCR contribution) was determined from the integration of each ion $Q_Z(E)$ over the entire energy spectrum and weighted by their contribution to the total dose. It was then summed for all ion charges from Z=1 to Z=26. It is calculated according to the following equation:

$$\overline{Q}_{GCR} = \frac{\sum_Z \int_{Emin}^{Emax} Q_Z(E)\, D_Z(E)\, dE}{\sum_Z \int_{Emin}^{Emax} D_Z(E)\, dE}, \quad (46)$$

where $Q_Z(E)$ is the quality factor of an ion with charge Z and energy E calculated by one of the three methodologies examined in this work (namely, ICRP Report 60 Eqs. (14)-(16)), TDRA Equations (20-21), and NASA model Equations (16-17)), $D_Z(E)$ is the corresponding absorbed dose ($\approx$ flux $\times$ LET) of each ion with energy E, and the limits of integration are set at $Emin = 1$ MeV and $Emax = 1$ GeV.

**Results**

We calculated the average quality factor of GCR for the mission using a modified version of the TDRA methodology (Eq. (21)), including all ions from protons up to Argon (Ar) and Iron (Fe). The saturated dose-mean lineal energy ($y_D^*$) values were calculated from a combined version of the microdosimetric models of Xapsos et al. 1994, 1996 with updated physical parameters (163). The $y_D^*$ and subsequently Q values have been determined for 1 μm sphere diameter of liquid water which is the sphere size of relevance to experimental measurements with TEPC (e.g., in ISS). As reference radiation (Q≡1), we used protons at 100 MeV since they can be safely considered as a low-LET radiation (LET $\approx$ 0.73 keV/μm). The GCR spectrum is obtained from the web-based OLTARIS platform for a deep space (1 AU) and LEO orbit (ISS) in the energy range of 1 MeV/amu - 1 GeV/amu. Figure 1 depicts the integral fluxes (particles/cm$^2$/day) of particles from protons up to Ar and Fe, with no-shielding conditions. The integral flux (par/cm$^2$-day) for deep space and Z=1-26 particles is depicted in Figure 14. The integral fluxes were calculated for no shielding conditions, as well as for 10, 20 and 30 g/cm$^2$ aluminium shielding using the OLTARIS platform (HZETRN transport code). The inset figure shows the integral fluxes of Z=1-2, in order to observe the rise of Z=1 particles with increasing shielding. Figure 15 shows the cumulative Q(Z) value ($Q_H, Q_H + Q_{He}, \ldots$) (dot-lines) for (a) LEO (ISS) and (b) deep space missions as a function of particle's charge ($1 \leq Z \leq 26$), as well as the mission (total) Q value (thick, solid lines), both calculated by the modified TDRA approach, behind different aluminium shielding (10-30g/cm$^2$) and 1977 solar minimum conditions. Aluminium shielding of this range covers most of the nominal shielding values used in spacecrafts for space missions (STS, ISS).

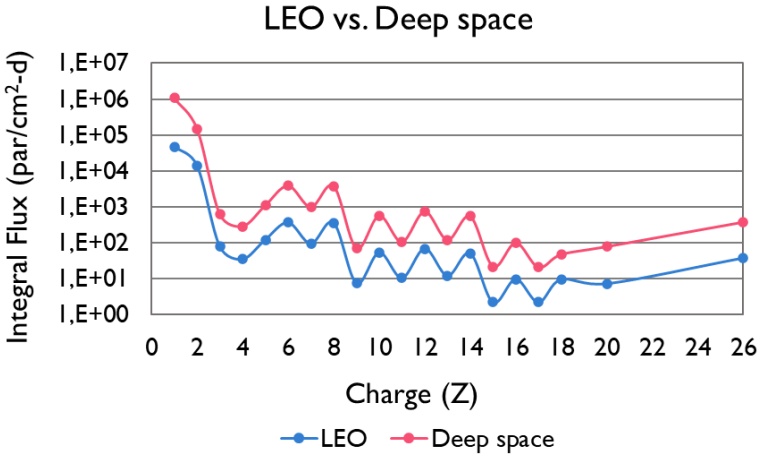


**Figure 13.** Integral Flux (particles/cm$^2$/day) of GCR particles from protons up to Fe, obtained from the OLTARIS platform for 1977 Solar Minimum conditions. Red line represents the integral flux in deep space (1 AU) and blue line the flux in LEO (ISS ~400 km), both for no shielding conditions.

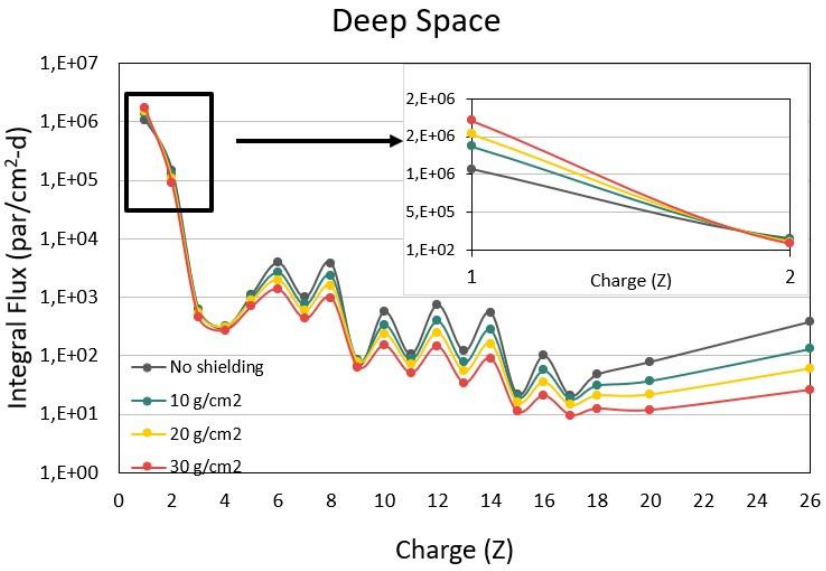


**Figure 14.** Integral Flux (particles/cm$^2$/day) of GCR particles from protons up to Fe for deep space, obtained from the OLTARIS platform for 1977 Solar Minimum conditions. The calculations were made for no shielding conditions, 10, 20 and 30 g/cm$^2$. The embedded Figure represents the integral flux for Z=1-2 for different aluminium shielding.

In addition to mission Q values, it is also useful to investigate the contribution of each particle relative to the total Q value, in order to further understand the impact of the space radiation environment to the carcinogenic risk to astronauts. Figure 16, depicts the cumulative contribution (in %) of the different GCR particles, relative to the total (mission) Q (i.e., $Q_H/Q_{total}$, $(Q_H + Q_{He})/Q_{total}$, ...), for (a) LEO (ISS) and (b) deep space mission scenarios, both calculated behind different aluminium shieldings ($10 - 30$ g/cm$^2$). For better insight, the results are grouped into GCR particles of different atomic number ($Z$=1, $Z$=1-2, $Z$=1-26).

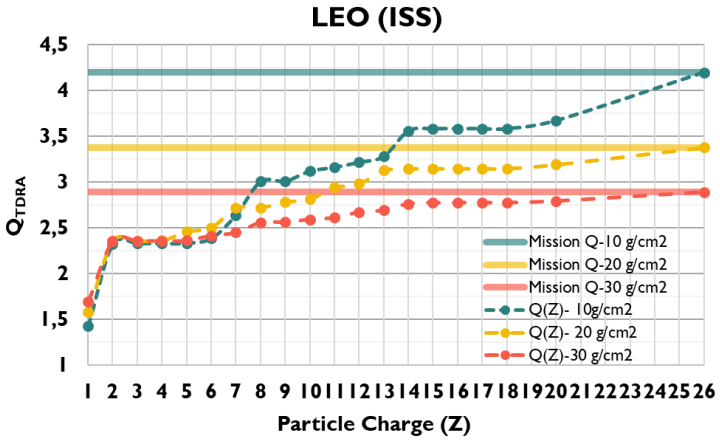


(a)

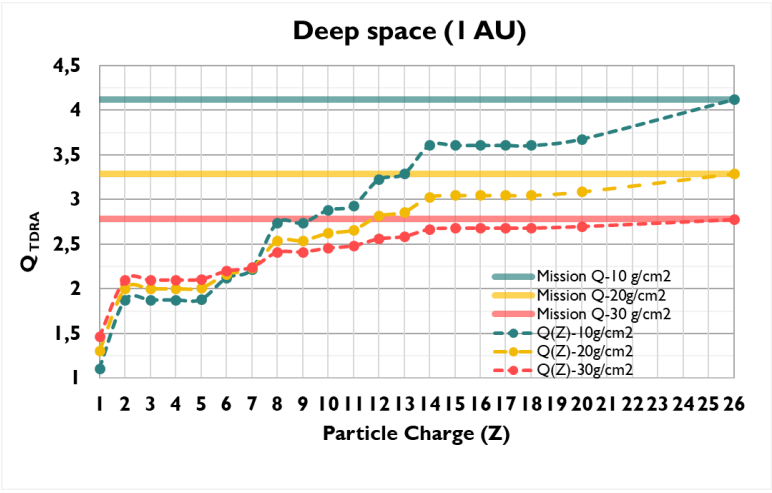


(b)

**Figure 15.** Cumulative Q value of GCR as a function of particle's charge ($Z$) (dot-lines), calculated by TDRA for (a) LEO (ISS ~400 km) and (b) deep space (1 AU), both calculated behind aluminium shielding of 10-30g/cm$^2$. Thick, solid lines are the mission Q values

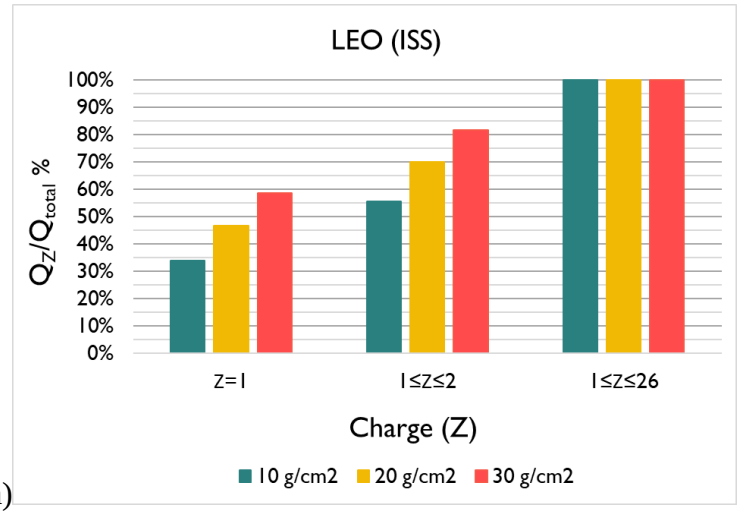


(a)

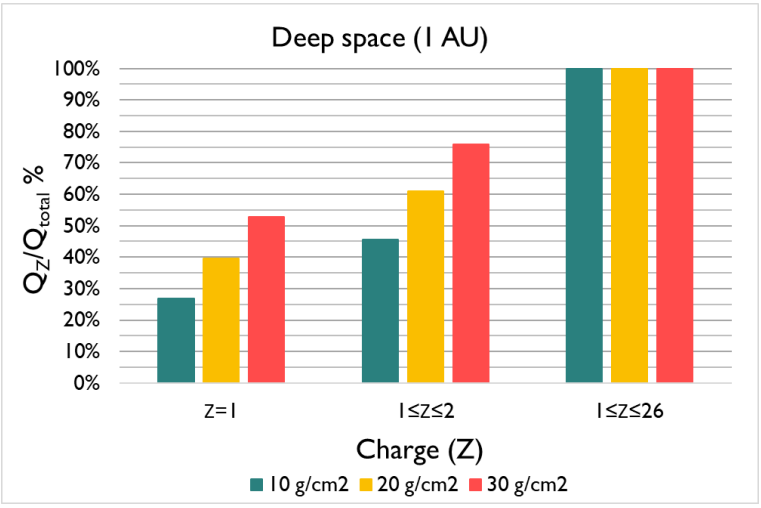


(b)

**Figure 16.** Contribution (%) of different GCR particles to the total (mission) Q value calculated with the TDRA methodology for (a) LEO (ISS ~400 km) and (b) deep space (1 AU), both behind aluminium shielding of 10-30 g/cm$^2$

The influence of shielding on the mission quality factor is depicted in Figure 17 for both LEO and deep space.

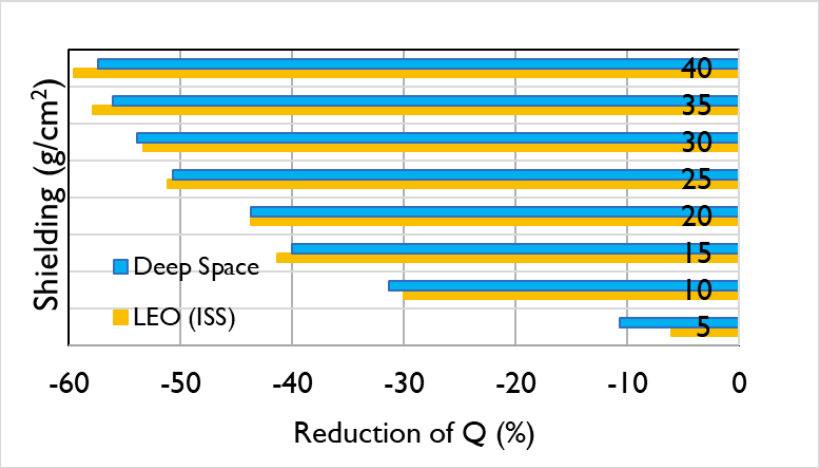


**Figure 17.** Reduction (%) of the TDRA-based mission Q-value, with increasing aluminium shielding (5-40 g/cm$^2$) for LEO (ISS ~400 km) and deep space (1 AU).

In Tables 7 and 8, the present mission Q values calculated by the TDRA approach (using a 1 μm liquid water target sphere), were compared against NASA's model ($Q_{NASA}$) and the ICRP Report 60, Q(L). Comparisons were made for LEO (ISS ~400 km) and deep space (1 AU), for different aluminium shielding thickness in the range of $10 - 30$ g/cm$^2$.

**Table 7.** LEO (ISS ~400 km) mission Q values calculated by the present TDRA approach are compared against Q values calculated according to ICRP Report 60 and the NASA model

| **LEO (ISS)** **Al (g/cm$^2$)** | **This work ($Q$-values from TDRA)** | **ICRP Report 60 ($Q$-values from OLTARIS)** | **Difference (%) ICRP as baseline** |
|---|---|---|---|
| **10** | 4.2 | 4.6 | −8.7 |
| **20** | 3.38 | 3.14 | 5.79 |
| **30** | 2.89 | 2.64 | 9.47 |
| **LEO (ISS) Al (g/cm$^2$)** | **This work ($Q$-values from TDRA)** | **NASA model ($Q$-values from OLTARIS)** | **Difference (%) NASA as baseline** |
| **10** | 4.2 | 4.2 | 0 |
| **20** | 3.38 | 3.27 | 3.37 |
| **30** | 2.89 | 2.91 | −0.68 |

**Table 8.** Deep space (1 AU) mission Q values calculated by the present TDRA approach are compared against Q values calculated according to ICRP Report 60 and the NASA model

| Deep space (1 AU) Al (g/cm$^2$) | This work (Q-values from TDRA) | ICRP Report 60 (Q-values from OLTARIS) | Difference (%) ICRP as baseline |
|---|---|---|---|
| **0** | 5.95 | 6.22 | −4.3 |
| **10** | 4.12 | 3.9 | 5.64 |
| **20** | 3.29 | 2.89 | 13.84 |
| **30** | 2.78 | 2.51 | 10.76 |
| **Deep space (1 AU) Al (g/cm$^2$)** | **This work (Q-values from TDRA)** | **NASA model (Q-values from OLTARIS)** | **Difference (%) NASA as baseline** |
| **0** | 5.95 | 6.32 | −5.85 |
| **10** | 4.12 | 4.19 | −1.67 |
| **20** | 3.29 | 3.2 | 2.81 |
| **30** | 2.78 | 2.86 | −2.8 |

Additionally, in Tables 9 and 10, we compared the present mission Q values calculated by the TDRA approach (using a 1 μm liquid water target sphere), against measurements from active detectors (TEPC) that have flown in ISS and Space Shuttle (Table 9) as well as aboard the MSL-RAD during the period of its transit to Mars with Curiosity (Table 10).

**Table 9.** LEO (ISS ~400 km) mission Q values calculated by the present TDRA approach are compared against measured Q values by TEPC aboard ISS and Space Shuttle missions. Shielding values presented are the nominal values

| LEO (ISS) Al (g/cm$^2$) | This work (Q-values from TDRA) | Space Shuttle (ISS orbits) (72,152,164,165) | ISS (69,166) |
|---|---|---|---|
| **~10** | 4.2 | $2.97 \leq Q \leq 4.33$ | – |
| **~20** | 3.38 | – | $2.8 \leq Q \leq 3.7$ |

**Table 10.** Deep space (1 AU) mission Q values calculated by the present TDRA approach are compared against measured Q values by TEPC aboard the MSL-RAD

| **Deep space (1 AU)** | **This work (Q values from TDRA)** | **MSL RAD (Cruise to Mars)** (167) |
|---|---|---|
| **Al (g/cm$^2$)** | | |
| **10-30** | $2.78 \leq Q \leq 4.12$ | $3.84 \pm 0.25$ |

**Discussion**

It is clear from Figure 13 that even-numbered high-Z particles (such as $C, O, Mg, Si, Fe$) are more abundant than odd-numbered particles The elemental composition of GCR provides useful insight into their origin. The propagation of elements into the interstellar gas, the nuclear interactions, the acceleration mechanisms and first ionization potential, are the key effects of their abundance. The reason lighter elements from Li to B (Z=3-5) are relatively more abundant is due to the interaction of the heavier source particles, such as carbon, oxygen, or nitrogen with the interstellar gas as they propagate into the heliosphere and break into these lighter charged particles. For 5<Z<26 the pairing effect (greater binding energies) is the underlying reason for the abundances of the even-numbered charged particles(168,169). Furthermore, the absorbed doses are much higher in deep space (1 AU) than in LEO (ISS ~400 km), since the GCR flux is significantly higher for all Z (Figure 13). Figure 15 shows that mission Q values for the GCR spectrum in both LEO and deep space missions are very similar and vary between 2.9 and 4.2 depending on shielding. The details of the cumulative distribution of Q as a function of Z reflects the higher contribution of even-numbered Z particles relative to the odd-numbered particles, while it is slightly more pronounced for deep space than for LEO. As expected, the effect of shielding is significant for both LEO and deep space; specifically, within the range of aluminium shielding encountered in space missions (10–30 g/cm$^2$) Q varies by a factor of ~1.5, i.e., from Q=2.9 (10 g/cm$^2$) to Q=4.2 (30 g/cm$^2$). An interesting observation is that with increasing shielding, the contribution of low-Z particles ($1 \leq Z \leq 2$) is increased compared to the high-Z particles (Figure 4), from 55% to 80% for LEO and from 45% to 75% for deep space. This stems from the fact that, with increasing shielding, more high-Z particles are stopped in the shielding, if their energy is relatively small, or undergo nuclear fragmentation. The latter interactions produce low-Z ions capable of penetrating the shielding material (Figure 14).

Another interesting observation is that, as shown in Figure 17, an increase of shielding from 10 to 30 g/cm$^2$ (i.e., by a factor of 3) results in only a moderate reduction of Q by 30% (10 g/cm$^2$) to 50% (30 g/cm$^2$), and this is true for both LEO and deep space. This may be explained by the increased production of low-Z fragments with increasing shielding (as also discussed above) which somewhat compensates for the higher absorption of the high-Z particles. For aluminium values greater than 30 g/cm$^2$, the mission Q values do not decrease significantly. For this reason, a shielding between $25-30$ g/cm$^2$ (especially for deep space missions) seems adequate if we consider the trade-off between increased shielding (weight, cost) and relative reduction of Q. The cost of aluminium shielding depends on several factors (market, mission, method of production, geometry configuration of spacecraft) and the decision on the shielding material and value would also include the reduction of absorbed doses and other engineering issues(170–172). It should also be noted that hydrogen-rich materials (polyethylene, Lithium Hydride, water) may be more suitable than aluminium for radiation

mitigation(11,114,173,174). The present, TDRA-based Q values are in good agreement with both the ICRP Report 60 Recommendations and NASA's model (Table 7 and 8) despite the quite different methodologies. Specifically, the TDRA-based Q values are within ~14% (deep space) and ~10% (LEO) of the ICRP LET-based Q values. Even better agreement was found between the TDRA-based Q values and NASA's model with differences up to 3% for both missions. In hadron therapy, it is generally assumed that differences in RBE calculations for deterministic effects should not exceed ~5%, due to the need of precise treatment planning in the tumour volume and organs at risk. However, in space radiation protection, the lack of suitable data for heavy-ions regarding their low-dose RBE for stochastic effects, causes much larger uncertainties which, inevitably, affect the effective dose calculations for planned missions. As a result, differences between TDRA and Report 60 methodologies of 10-14% in mission Q values may be considered modest. Nevertheless, Q(Z) values averaged over the spectrum of the individual ions may deviate substantially among the different methodologies (TDRA, ICRP Report 60, NASA), which may be important when considering cancer risk evaluation of astronauts for specific ions. The differences in Q-values among the different methodologies of NASA, ICRP Report 60 and microdosimetry approaches, for protons and heavier ions have been further discussed in literature(2,4,16,163).

The present, TDRA-based Q values are also within the range of measured Q values (Tables 9 and 10). For LEO, measurements were obtained from TEPC and other active detectors that have flown onboard the Space Shuttle missions and ISS (~400 km). For $10-20$ g/cm$^2$ aluminium shielding, which is representative of the Space Shuttle and ISS average or median values for the locations of the detectors, the TDRA-based Q values are between 3.4-4.2 which is well within the measured range (Table 9). However, thickness distributions have to be applied in order to estimate more realistic Q values, since there are parts of spacecrafts that are less or heavier shielded. Various passive and active detectors are available for space missions towards radiation quality (e.g., LET spectra) measurements. Active detectors such as the TEPC, besides providing real-time read-out, are generally considered tissue-equivalent and, therefore, suitable for simulating energy deposition spectra in the human tissue. However, TEPC measurements for simulated tissue volumes at the nanometer scale (diameter <100 nm) are difficult and less reliable. As a result, Monte-Carlo simulation techniques offer a valuable theoretical tool for obtaining microdosimetry spectra (e.g., y-spectra) at the cellular and DNA scale, towards understanding the biological effects of ions relevant to the space radiation environment(26,36,175).For deep space calculations with aluminium shielding in the range $10-30$ g/cm$^2$, the TDRA-based Q value vary between 2.8 to 4.1 which is close to the values of 3.8 measured by MSL-RAD in deep space (Table 10).

An advantage of the present microdosimetric approach is that it overcomes the physical shortcomings of LET-based approaches, which does not accurately account for the energy deposition process since it neglects its stochastic nature (i.e., energy-loss straggling) as well as the finite range of secondary electrons (δ-rays), both of which may be crucial for HZE particles (e.g., ICRP). The central physical quantity of lineal energy is directly measurable by the active dosimeters (e.g., TEPC) used in space missions (e.g., ISS, MSL-RAD). It is also worth emphasizing that the fully analytic form of the present approach facilitates predictive calculations of the average Q-values in different mission scenarios.

## Conclusion

A generalized analytical microdosimetric model that considers energy-loss straggling and δ-rays transport was utilized in order to calculate lineal energy spectra in 1μm liquid water sphere that were subsequently used to determine the average GCR quality factor (Q) based on the TDRA methodology for two mission scenarios, namely, an ISS orbit (LEO) and a deep space

orbit (1 AU). The GCR spectra behind aluminum shielding in the range of $0-30$ g/cm$^2$ for the above radiation environments were obtained from NASA's online platform OLTARIS. These results were compared against the LET-based Q values of ICRP and NASA's Q model. It is shown that the present results for the average Q value of the GCR spectrum are in good agreement with both the ICRP and NASA model predictions for both mission scenarios. The present results are also within the range of values measured by TEPC in both LEO (ISS, Space Shuttle) and deep space (MSL-RAD). An advantage of the present microdosimetric approach is that it overcomes the physical shortcomings of LET-based approaches (e.g., ICRP) while its central physical quantity (lineal energy) is directly measurable by the well-established active dosimeters (e.g., TEPC) that are widely used in space missions (e.g., ISS, MSL-RAD). Finally, it is worth emphasizing that the present approach is fully analytic and robust, thus, facilitating its practical use for predictive calculations of the average Q values of different mission scenarios.

# Chapter 5

**Summary**[3]

Analytic models for calculating proton $y_D$ values in liquid water over a broad proton energy range (1 MeV – 1 GeV) of relevance to radiotherapeutic and space applications are compared against MCTS simulations by PHITS, RITRACKS, and Geant4-DNA. A new model is proposed that exhibits improved agreement with the MCTS data compared to the existing analytic models. The variation of the radiation protection quality factor (Q) with proton energy is calculated and its sensitivity to the estimates of $y_D$ from the various datasets is examined.

The original analytic model of Xapsos (Xcom) is modified and model parameters are updated. Direct proton energy deposition is described by implementing alternative energy-loss straggling distributions while the contribution of secondary electrons is calculated based on the dielectric formulation of the relativistic Born approximation. MCTS simulations of proton $y_D$ values using the latest versions of the PHITS (PHITS-KURBUC and PHITS t-sed), RITRACKS, and Geant4-DNA are reported. Proton $y_D$ values from the Monte Carlo Damage Simulation (MCDS) quasi-deterministic algorithm are also presented as an additional benchmark of LET-based estimates of $y_D$. The $y_D$ datasets generated by the above methods are used within the Theory of Dual Radiation Action (TDRA) to illustrate variations in Q with proton energy and uncertainties associated with the method of $y_D$ calculation.

[3] Chapter 5 is based on the paper (*submitted*) of Papadopoulos et al. Comparison of analytic and Mote Carlo calculations of proton dose-mean lineal energy from 1 MeV to 1 GeV: its impact on radiation protection quality factor. ***Medical Physics*** (2024).

**New microdosimetry-based analytic model**

Following Xapsos and co-workers(53) the present microdosimetric model considers both direct and indirect events. Direct events (or crossers) occur when a charged particle crosses through the volume of interest(51,54,144). Charged particles may also pass outside the target and ionize the surrounding material so that delta-ray electrons can reach the target and dissipate their energy inside it. This is termed an indirect event or toucher(20,144), as is shown in Figure 1.

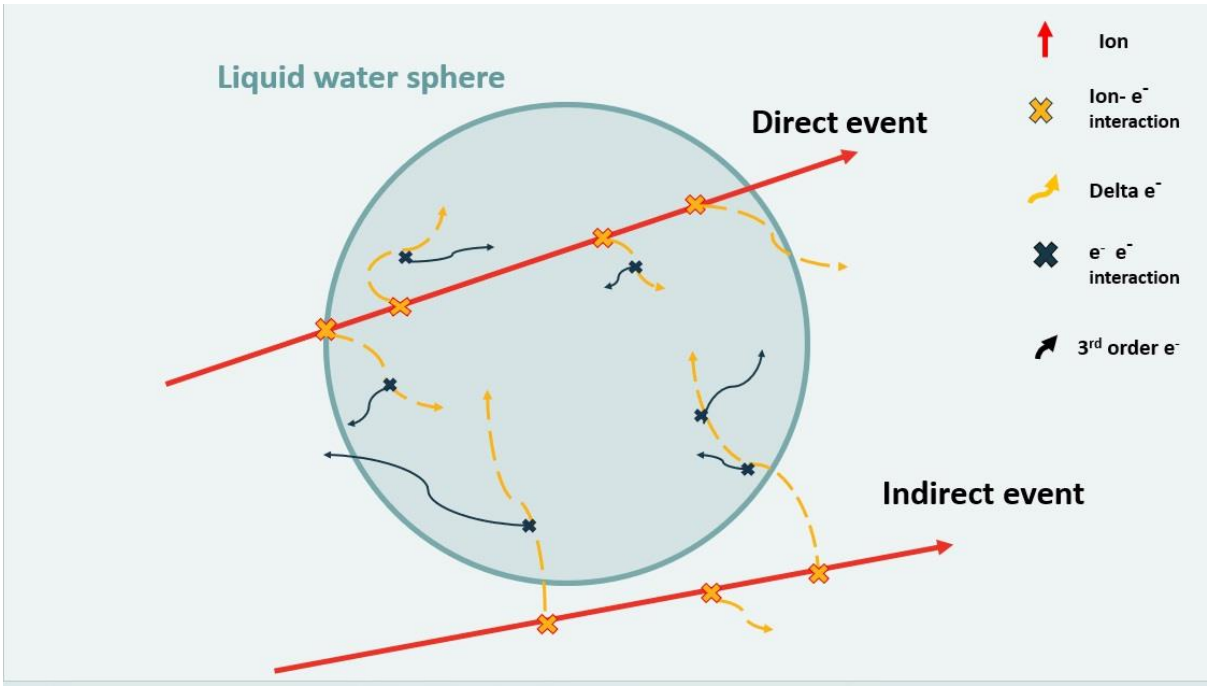


**Figure 17.** Schematic representation of the direct and indirect events considered by the microdosimetric models.

According to the above scheme illustrated in Figure 1, the total $y_D$ from direct and indirect events can be expressed by Eq. (26): $y_D = f_{ion} \times y_{D,dir} + (1 - f_{ion}) \times y_{D,ind}$ (144).

The above equation indicates that the total $y_D$ arises from both direct ($y_{D,dir}$) and indirect ($y_{D,ind}$) contributions which are combined with an appropriate weighting factor, $f_{ion}$ (156). The calculation of the various terms of Eq. (26) is discussed below.

**Direct Events**

The main physical inputs are the average deposited energy by protons in the target, the relative variance of the energy-loss straggling distribution, and the path length and LET fluctuations (23). In this work, we investigate alternative energy-loss straggling distributions guided from the MCTS simulation data obtained by Geant4-DNA, RITRACKS and PHITS, while the so-called straggling factor ($\delta_2$) is calculated from first principles within the Relativistic Plane Wave Born Approximation using a dielectric response function for liquid water(157). The spatially restricted LET and the weighting factors for direct (and indirect) are determined by the approach of Xapsos (144,176). Specifically, to determine the average energy deposited from direct events, it is assumed that a spherical target of 10-1000 nm is randomly crossed by a proton in the energy range of 1 MeV – 1 GeV. The proton dissipates energy to the target in a discrete manner, mainly through inelastic Coulomb interactions with the atomic electrons of

the medium. The ionized atomic electrons (called secondary electrons) can, in turn, lose their energies inside or outside the target, depending on their kinetic energy. To a first approximation, the average energy deposited by protons inside a target volume can be described by the product of the proton's LET and the mean chord length of that volume ($\bar{l}$) (22,23). However, as the proton's energy increases and the target dimension becomes smaller (μm–nm), the number of inelastic collisions with atomic electrons decreases and, in addition, more delta electrons may escape the target. Consequently, a restricted form of LET ($LET_{\Delta}$) and an energy-loss straggling distribution (δ) must be considered. For the average energy imparted to the target, we can utilize the equation (53):

$$\bar{\varepsilon} = f_{ion} \times LET \times \bar{l} \ , \tag{47}$$

$E_{max}$ is the maximum energy of a delta electron following a single proton collision:

$$E_{max} = \frac{2mc^2\beta^2\gamma^2}{1 + 2\gamma\left(\frac{m}{M}\right) + (\frac{m}{M})^2} \approx 2mc^2\beta^2\gamma^2 \ . \tag{48}$$

Where $f_{ion}$ is calculated by equation (27).

Concerning the energy-loss straggling, there are several analytical distributions for ions. However, most of them apply only to the limited range of ion energy and target dimensions. Olko and Booz (54) assume a Fermi-like function ($1/(e^x + 1)$) for direct events and an exponentially decreasing function for indirect events that was fitted to MC simulation data for proton and alpha particles in the energy range of 0.5–3 MeV and dimensions of 1-1000 nm. A more extensive analytic representation for protons with energy 0.3–20 MeV was made by Wilson (143) and Wilson and Paretzke (145), suggesting a two-parameter log-normal distribution for direct events and an exponential function for indirect events applicable to spheres with diameter from 2-100 nm. The log-normal parameters of the mean and the variance were considered as free parameters fitted to their MC simulations. The microdosimetric model of Xapsos (53,144,151,160) has been extensively applied to Tissue Equivalent Proportional Counter (TEPC) measurements for space radiation environments. For this application, a log-normal energy-loss straggling distribution has been utilized and applied to spheres with diameters in the range ~2–1000 nm. This distribution had been selected since some early $^{60}Co$ experiments and proton MC data in the energy range of 0.3–20 MeV were well represented by a log-normal distribution. Recently, an updated Xapsos model with a log-normal energy-loss straggling distribution was presented and applied to protons up to 250 MeV in water liquid spheres of 10–1000 nm (163). The resulting microdosimetry calculations ($y_D$) showed good agreement with recent MCTS simulation data, although at higher energies (>50–100 MeV) and nanometer dimensions (10–100 nm) larger discrepancies were observed.

Despite the above developments, microdosimetric calculations for particle radiotherapy and radiation in outer space environments require comprehensive proton and ion $y_D$ values, over a wide spectrum of energies and target dimensions. For example, proton data for energies at least up to 250 MeV (radiotherapy) or 10 GeV (space radiation protection) are needed (4,7,11,13,14,22,177). Towards extending the applicability of the present model to a wide range of proton energies (from MeV to GeV) and target dimensions (from μm down to nm), we have examined the implementation of various statistical distributions (Log-normal, Erlang, and Logistic) for representing the proton's energy-loss straggling.

The probability density function (PDF) of the Log-normal distribution for the energy straggling (x), with parameters $\mu_{lgn}$ and $\sigma_{lgn}$ is given by Eqs. (36), (37) and (38).

The PDF of the Erlang distribution for the energy-loss straggling (x), with shape parameter κ and rate parameter λ, reads:

$$p(x;\lambda,\kappa)_{Erl} = \frac{\lambda^{\kappa}}{(\kappa-1)!}x^{\kappa-1}e^{-\lambda x}\,. \tag{49}$$

The parameters λ and κ relate to the mean and the variance of the Erlang distribution which, in turn, are related to the mean energy deposited to the site ($\bar{\varepsilon}$) and the relative variance (V) of the random processes. The equations for the parameters λ and κ can be obtained from:

$$\lambda = \frac{1}{V \times \bar{\varepsilon}}\,, \tag{50}$$

$$\kappa = \frac{1}{V}\,. \tag{51}$$

The PDF of the logistic distribution for the energy-loss straggling (x), with mean parameter $\mu_{log}$ and scale parameter s is:

$$p(x;\mu_{log},s)_{Log} = \frac{1}{4s}\mathrm{sech}^2\left(\frac{x-\mu_{log}}{2s}\right). \tag{52}$$

In a manner analogous to the Log-normal and Erlang distributions, the parameters $\mu_{log}$ and s are associated with the mean energy deposited to the target ($\bar{\varepsilon}$) and the relative variance (V) through the following expressions:

$$\mu_{log} = \bar{\varepsilon}\,, \tag{53}$$

$$s = \frac{\sqrt{3}}{\pi}\bar{\varepsilon} \times \sqrt{V}\,. \tag{54}$$

The relative variance V needed in Eqs. (50-51) and (54) is calculated by the equation (39), $V = V_s + V_s \times V_{LET} + V_\delta + V_{LET} \approx V_\delta + V_s$.

$V_{LET}$ is the relative variance of the particle's LET as it crosses the volume under study. For the energy range of protons (1 MeV-1 GeV) and the sphere diameters (10–1000 nm) considered in this work, the proton energy loss is small compared to its kinetic energy. Therefore, the LET value for each proton energy does not change significantly across the target volume, so there are no LET fluctuations for monoenergetic proton beams, i.e., $V_{LET} \approx 0$ (144).

$V_s$ represents the fluctuations of the ion's path length. Protons in the present energy range (1 MeV – 1 GeV) have a much larger range than the target dimensions, so it may be assumed that they cross the target in straight lines (23,128). As a result, the fluctuations in the proton's track length distribution can be determined if their path line equation is known. Assuming a track length distribution for a sphere, $c(l) = 2l/d^2$, it follows that $V_s$ is constant and equal to $0.125$ (23).

$V_\delta$ represents the relative variance of the energy-loss straggling of delta electrons. This parameter depends upon the delta influx and efflux since not all secondary electrons would deposit their energy locally and some may escape the target, especially for nanometer dimensions (22,23,144). In general, for energies much larger than the binding energies, the secondary electron spectrum is assumed to follow a $1/E^2$ pattern. However, this does not hold for very low-energy electrons which have energies comparable to atomic binding energies(178). So, the difficulty for an accurate consideration of the energy-loss straggling distribution of delta electrons lies in determining the single-collision spectrum, especially for

low-energy transfers. $V_\delta$ is commonly represented by the dose-weighted energy that is deposited in the target in a single collision ($\delta_2$)(23,144) :

$$V_\delta = {}^{\delta_2}/_{\bar{\varepsilon}}, \tag{55}$$

In the present work, $\delta_2$ is calculated from first principles according to the expression (23):

$$\delta_2 = \frac{\sum_n^{\text{ioniz.}} \int_0^\Delta (E + B_n)^2 \frac{d\sigma_{RPWBA}^{(n)}}{dE}\, dE}{\sum_n^{\text{ioniz.}} \int_0^\Delta (E + B_n) \frac{d\sigma_{RPWBA}^{(n)}}{dE}\, dE}, \tag{56}$$

where $d\sigma_{RPWBA}^{(n)}/dE$ is the differential ionization cross section (DICS) in secondary electron energy for the *n*-th ionization shell calculated within the relativistic plane wave Born approximation (RPWBA) (see below), $B_n$ is the binding energy of the *n*-th ionization shell, and the upper limit of the integrals includes the cut-off energy $\Delta$ to account only for energy losses that remain to the target (53). The $\Delta$ values were obtained for each sphere diameter by Geant4-DNA simulations for electron penetration depths with the condition that $\Delta$ equals the mean chord length of the target volume (163,179). The following values were obtained: $\Delta$=5.56 keV for d= 1000 nm, $\Delta$=1.37 keV for d=100 nm, and $\Delta$=0.180 keV for d=10 nm.

The total probability density function for the energy loss ($x$) in the target is the convolution of the energy-loss straggling distribution ($p(x;\lambda,\kappa)$) of each proton energy and path length l, with the chord length distribution, $c(l)$ (53):

$$f(x,l) = \int p(x)c(l)dl\,. \tag{57}$$

Then, Eq. (57) with the appropriate energy-loss straggling distribution (Log-normal, Erlang, Logistic), may be used in Eqs. (9) and (10) to calculate the $y_D$ for direct events.

**Indirect Events**

In the case of indirect events, delta electrons created from ions that pass outside the target, may reach and deposit energy inside the target. For sufficient small targets, there is also a chance that energetic secondary electrons escape the volume. Describing the secondary electron spectrum analytically is a difficult theoretical task. Xapsos and co-workers (144) suggested an approach that is analogous to that of the direct events by calculating the average energy deposited by electrons in the target and the fluctuations of the three random factors ($LET, l, \delta$). In that approach, the mean electron LET is determined by assuming a $1/E^2$ initial electron energy spectrum (produced by the ion) and $1/LET_e(E)$ average LET slowing down electron spectrum.

In the present work for each proton energy, the mean $y_D$ of indirect events is calculated as follows:

As a monoenergetic proton ionizes the medium (outside the target), there is a probability $\{P_1, P_2, \ldots\}$ of ejecting electrons with energies $\{E_1, E_2, \ldots\}$. This probability is determined by the DICS (see next section). Then, each electron with energy $E_i$, will ionize other electrons of the target, resulting in a value of $y_{D,i}$. According to this approach, secondary electrons can be characterized by the triplet $\{P_i, E_i, y_{D,i}\}$ associated with their probability of ejection ($P_i$), kinetic

energy ($E_i$) and the corresponding $y_{D,i}$ values, respectively, as shown schematically in Figure 18. In the present work, the $y_D$ values for each electron energy and sphere diameter were pre-calculated via Geant4-DNA simulations for monoenergetic electrons with initial energy covering the whole secondary electron spectrum. Then, the mean $y_{D,ind}$ for indirect events for each proton energy (1 MeV – 1 GeV) and target dimension (10 nm, 100 nm, and 1000 nm), can be calculated from the following integral:

$$y_{D,ind} = \frac{\sum_n^{ioniz.} \int_{\Delta}^{E_{max,n}} y_D(E,d) \times \frac{d\sigma_{RPWBA}^{(n)}}{dE} dE}{\sum_n^{ioniz.} \int_{\Delta}^{E_{max,n}} \frac{d\sigma_{RPWBA}^{(n)}}{dE} dE}, \quad (58)$$

where $E_{max,n} = \frac{E+B_n}{2}$ and $d\sigma_{RPWBA}^{(n)}/dE$ is the differential ionization cross section (DICS) in secondary electron energy for the *n*-th ionization shell (see below). The denominator in Eq. (58) is used for normalization purposes. The lower integration limit Δ of the above equation is the appropriate geometrical cut-off energy for electrons, based on the Spencer-Attix considerations (144,180). Note that the same Δ values employed in Eq. (56) are utilized in Eq. (58) for the sphere diameters of 10, 100, and 1000 nm.

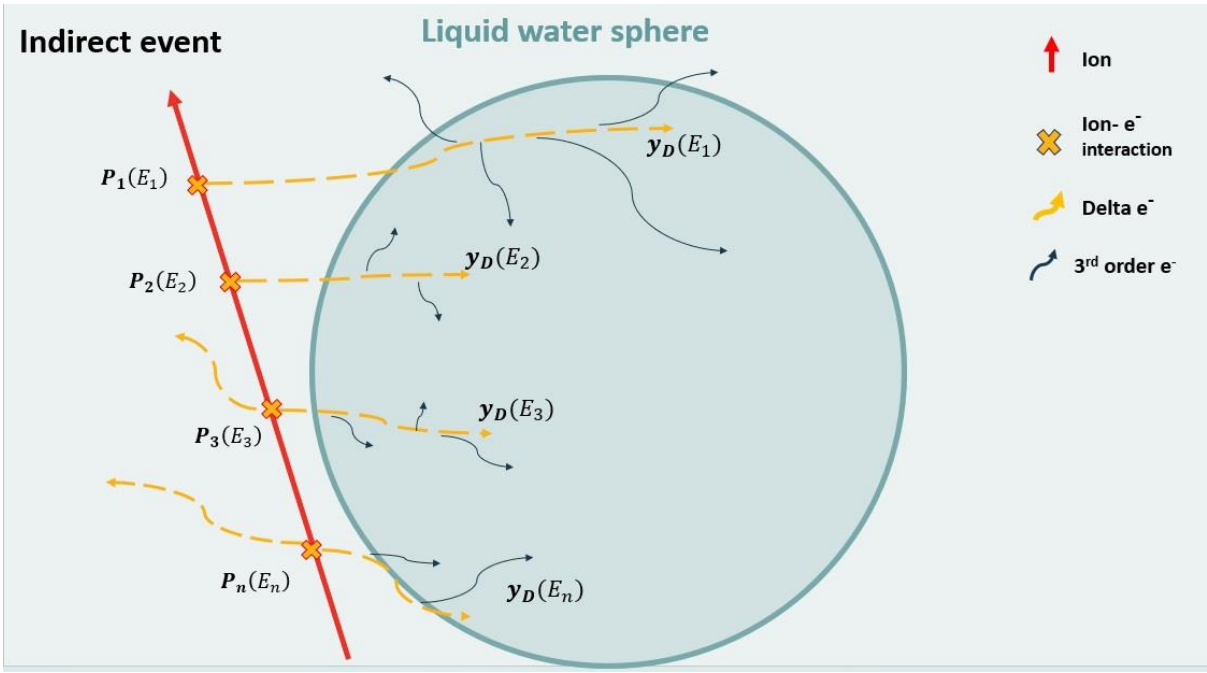


**Figure 18.** Schematic representation of the method followed by the microdosimetric models for the indirect events.

### Proton inelastic cross sections

To address the interaction between energetic protons and atomic electrons in liquid water, the dielectric formulation of the Relativistic Plane Wave Born Approximation (RPWBA) are considered the state-of-the-art in the field(181). This approach is used to calculate the DICS which is needed to calculate important physical parameters of the model as described above (e.g., proton LET, $\delta_2$, and $y_{D,ind}$). As mentioned above, the main energy-loss mechanism of protons in the energy domain considered here, is the inelastic interaction with the atomic electrons. For condensed phase (liquid or solid) water, the bare Coulomb interactions between protons and atomic electrons are affected by the long-range polarization and screening effects of the medium. These effects are known to (strongly) influence the electronic excitation spectrum, especially the low energy-loss part of the spectrum. The above effects are commonly

considered via the complex dielectric response function (DRF), $\varepsilon(W,q) = \varepsilon_1(W,q) + i\varepsilon_2(W,q)$ of the medium with W and q being the energy transfer and recoil energy (or momentum transfer), respectively. Note that $W$ equals $W \equiv E + B_n$ in the case of ionizations and $W \equiv B_k$ in the case of excitation with $B_n$ and $B_k$ being the binding energy of the $n$-th shell and the excitation energy of the k-th discrete transition, respectively. In the context of the RPWBA, the only non-trivial part in the calculation of DICS is the energy-loss -function (ELF) defined as (182–186):

$$ELF \equiv Im\left[-\frac{1}{\varepsilon(W,q)}\right] = \frac{\varepsilon_2(W,q)}{|\varepsilon(W,q)|^2}. \quad (59)$$

Many different approaches have been presented in the literature for calculating the ELF of liquid water(179,183,184,187,188). In the present work we adopt the latest model implemented in Geant4-DNA. In this approach, the real part of the DRF is decomposed to the individual ionization shells (n) and excitation levels (k) of liquid water yielding the following expression for the ELF:

$$ELF = ELF_{ioniz} + ELF_{excit} = \sum_{n}^{ioniz.} \frac{\varepsilon_2^{(n)}(W,q)}{|\varepsilon(W,q)|^2} + \sum_{k}^{excit.} \frac{\varepsilon_2^{(k)}(W,q)}{|\varepsilon W,q|^2}. \quad (60)$$

To obtain the dependence of the ELF upon both W and q, a Drude-type parameterization of experimental optical data ($q = 0$) is extended to non-zero momentum transfers ($q > 0$) by analytic dispersion relations. The details of the parametrization algorithm and dispersion relations is given elsewhere (186). Although the above dielectric model is already implemented into the Geant4-DNA for electron transport(186), it is the first time that it is applied to proton inelastic collisions up to relativistic energies.

In RPWBA, the DICS is the sum of two terms (181):

$$\frac{d\sigma}{dE} = \frac{d\sigma_L}{dE} + \frac{d\sigma_T}{dE}, \quad (61)$$

where the subscript "L" and "T" refer to the longitudinal and transverse interaction terms, respectively, which relate to the momentum transfer along or perpendicular to the ion's motion. The are given by the following expressions (186):

$$\frac{d\sigma_L}{dE} = \frac{2}{\pi \alpha_0 N m c^2 \beta^2} \sum_n^{ioniz.} \int_{q_{min,n}}^{q_{max,n}} \frac{\varepsilon_2^{(n)}(W,q)}{|\varepsilon(W,q)|^2} \frac{(q+mc^2)}{q(q+2mc^2)} dq, \quad (62)$$

and

$$\frac{d\sigma_T}{dE} = \frac{1}{\pi \alpha_0 N m c^2 \beta^2} \sum_n^{ioniz.} \frac{\varepsilon_2^{(n)}(W,0)}{|\varepsilon(W,0)|^2} \left\{ \ln\left(\frac{1}{1-\beta^2}\right) - \beta^2 \right\}, \quad (63)$$

where $\alpha_0$ is the Bohr radius, N is the density of water molecules in unit density of water, $\beta$ is the scaled proton velocity, $\beta = u/c$, with u the incident proton velocity. Note that, for the transverse term, we adopt the small-angle scattering approximation and consider only collisions with (nearly) zero-momentum transfer (189). The limiting values of the recoil energy are (181):

$$q_{max,n/min,n} = \sqrt{\sqrt{T(T+2Mc^2)} \pm \sqrt{(T-E-B_n)(T-E-B_n+2Mc^2)}]^2 + (mc^2)^2} - mc^2, \quad (64)$$

where $M, T$ is the proton mass and kinetic energy, respectively. The stopping power (SP) (or unrestricted LET) of protons can be calculated within the RPWBA using the expression(101):

$$SP = \sum_n^{ioniz.} \left( \int_0^{E_{max}^{(n)}} (E + B_n) \frac{d\sigma_{RPWBA}^{(n)}}{dE} dE \right) + \sum_k^{excit.} \left( B_k \sigma_{RPWBA}^{(k)} \right). \quad (65)$$

Note that $\sigma_{RPWBA}^{(k)}$ is simply the integral of Eqs. (61) and (62), whereby the summation over the ionization shells is replaced by a summation over the discrete excitation transitions (k).

**Monte Carlo calculation of $y_D$**

**Geant4-DNA**

The Geant4 toolkit(131–133) is a general-purpose Monte Carlo code for the simulation of the passage of particles through matter. It was initially released in 1998 for simulating high energy physics experiments; however, thanks to its flexibility and the work of the Geant4 collaboration, nowadays it can be used in many fields like space physics and medical physics, among others. Within Geant4, Geant4-DNA was developed as an extension to model biological damage induced by ionizing radiation at cellular and subcellular scale (39–41,190); with this purpose, Geant4-DNA incorporates discrete interaction models of ionizing radiation with liquid water molecules to carry out MCTS simulations.

For this work, the microdosimetric quantities were calculated using the code described in (191), compiled with version 11.1.2 (June 2023). A pencil beam of protons was produced at the central point of a side of a box-shaped volume made of water ("world volume"), pointing towards the opposing side. The lateral dimensions of the box were large enough to ensure that all secondary electrons were stopped within the simulated volume. For each proton energy considered, the maximum energy transferred to a secondary electron was calculated and the maximum range $R_{\delta,max}$ was estimated (192). Then, the lateral dimensions of the box, measured from the center, were set slightly larger than $R_{\delta,max} + d_{site}$, with $d_{site}$ being the site diameter; this was done to ensure that the furthest possible random placement of the site lied within the volume(191) . As examples, the transversal dimensions were 2.8 mm for 300 MeV protons and 1.3 μm for 1 MeV protons.

Sites were placed on the proton track following the "weighted" random sampling approach(191,193), which consists in selecting an energy transfer point, then placing the spherical site randomly around it and finally scoring the energy imparted by adding all the energy deposits encountered within it. To ensure that any secondary electron which would potentially irradiate the site (i.e., those produced a distance smaller than $R_{\delta,max}$ upstream or downstream), we considered for the random placement of the site only the energy transfer points located within a central slab region oriented normally with respect to the proton track. The slab transversal dimensions were equal to those of the world volume. Longitudinally, the slab thickness varied from 0.1 μm (protons at 1 MeV) to 1.0 μm (protons at 300 MeV) to ensure a large enough number of energy transfer points within it and a sufficiently small proton energy loss; further, each boundary was at a distance $R_{\delta,max}$ from the nearest boundary of the world volume. Therefore, the total size of the world volume along the proton initial direction was twice $R_{\delta,max} + d_{site}$, plus the slab thickness. To minimize the impact of the small variation of the proton energy along the slab, the initial energy of the protons was such that the mean value between the proton energy at the entrance and exit of the slab equalled the energy under study.

The physics list used in these simulations was “G4EmDNAPhysics_option2”, the accelerated default physics constructor. This option allows the simulation of proton interactions up to 300 MeV (194) and electron interactions from 7.4 eV up to 1 MeV. As for proton transport, three approaches are considered, depending on its kinetic energy: Drude theory (up to 500 keV), non-relativistic Born approximation (0.5-100 MeV), and RPWBA (100-300 MeV)(190,194). As for electron interactions, Champion model was used for elastic scattering, and Born model was used for electronic excitation and ionization(190).

**PHITS-KURBUC**

The PHITS track-structure model for protons based on the algorithms of KURBUC code, so-called the PHITS-KURBUC model(141), was used to calculate the $y_F$ and $y_D$ values. The PHITS-KURBUC model considers elastic scattering, ionizations ($1b_1$, $3a_1$, $1b_2$, $2a_1$, and $1a_1$), excitations ($A^1B_1$, $B^1A_1$, Ryd A+B, Ryd C+D, diffuse band, and collective), dissociative electron attachments (OH(−), O (−), and H(−) productions), molecular excitations (vibrational (bending and stretching), phonon (librational and translational), and rotational excitations (normal and fast components), electron loss, and electron capture. In this calculation, we used the PHITS version 3.31, and set the cut-off energies of protons and electrons as 1 keV and 1 eV, respectively.

When calculating the $y$ distribution, a 10, 100, or 1000 nm diameter water target (i.e., $H_2O$ at a density of 1.0 g/cm$^3$) was placed at the origin surrounded by a 1 cm diameter water which can sufficiently provide secondary electron equilibrium. Because of the available energy range of the PHITS-KURBUC model, the protons with 1-300 MeV were incident on the target. In this simulation, we also calculated the indirect events (the energy deposited in the target by secondary electrons) by considering the protons passing outside the target as they slow down. Note that considering the radial dose distribution (141), we set the radius of the circle plane proton source as 2000 nm. The energy deposition in the water $\varepsilon$ was scored by using the t-deposit tally that allows us to obtain deposition energies in certain regions. After that, the probability densities of lineal energy were obtained using Eq. (1), and the $y_F$ and $y_D$ values were calculated by using Eqs. (2) and (3). The $y_F$ and $y_D$ values were calculated with sufficient numbers of particles to make the statistical uncertainty less than 5%.

**PHITS t-sed**

The PHITS code also enables the calculation of the microscopic probability densities of lineal energy and specific energy using an analytical function (microdosimetric function) based on the track-structure simulations, which is named t-sed tally(195,196). In 2006, the t-sed tally was first developed by using a Monte Carlo track-structure code of TRACEL(197). Recently, PHITS-original track-structure models, i.e., PHITS electron track-structure (PHITS-ETS) and PHITS ion track-structure model for arbitrary materials (PHITS-ITSART) were developed. From such a development background, the microdosimetric function in the t-sed tally was updated based on the PHITS-ETS and PHITS-ITSART models(49). We simulated the protons with 1–1000 MeV and scored the probability densities of lineal energy to calculate the $y_F$ and $y_D$ values of a 10, 100, or 1000 nm diameter water sphere. Note that the nuclear reaction models were inactivated in this PHITS calculation. After calculating the lineal-energy distribution, we calculated the $y_F$ and $y_D$ values with sufficient numbers of particles to make the statistical uncertainty less than 1%.

**RITRACKS**

The code RITRACKS simulates the detailed track structure of ions, electrons, and photons in liquid water. The transport algorithms and cross sections used are described in Plante and Cucinotta 2011(48) and references therein. RITRACKS has been used for the calculation of dose in targets(198,199), radiation chemistry(200), and chromosome damage(201,202). In RITRACKS, an irradiated volume is defined, and targets are placed within it. For this work, the spherical targets were placed at the center of an irradiated volume of the shape of a cylinder, with a radius equal to the radius of the sphere (and length equal to 5 microns). The cylinder was irradiated uniformly by ions impacting the bottom surface. Proton energy is kept constant as they are transported across the cylinder. Periodic boundary conditions were not implemented on the volume, so that delta electrons leaving the irradiated volume were not contributing to the dose, except possibly for the rare cases where an electron trajectory could go back and impact the target(198). On the other hand, secondary electrons generated inside the irradiated volume, but outside the target, are still allowed to deposit energy to the target. The number of simulation histories varied from 1,200 to 60,000, depending on the size of the target and proton energy, to minimize uncertainty on the results. One track and one target were simulated per Monte-Carlo history. For each simulation history, the energy deposited in the target was recorded. The corresponding lineal energy (y) for each target was calculated using equation (1). Using the data for all targets, histograms of the quantities $y$ and $y^2$ were obtained. The average lineal energy $y_F$ was obtained as the mean of the histogram of $y$. For $y_D$, the mean of the histogram of $y^2$ was used and divided by $y_F$, as in equation (3).

**MCDS**

The MCDS was originally developed to estimate the clustering of DNA lesions to form SSB, DSB and other complex types of DNA damage(203,204). In 2011, the MCDS was extended to predict DNA damage for a wider range of ions, ion energies and oxygen conditions, i.e., from a $pO_2$ value in the range from 0–100% (205). Of note, the MCDS does not rely on any information related to stopping powers, LET, target size or estimates of microdosimetric quantities to estimate the yield of clusters of DNA damage(142,203–205).

The 2011 version of the MCDS (version 3.10A) introduced a deterministic algorithm to estimate microdosimetric quantities (specific energy, lineal energy), CSDA range and related information for ions passing through a pure water, or water equivalent, medium. The MCDS accounts for ion stopping power changes in water for $(Z_{eff}/b)^2$ in the range from 1 to ~ $10^4$ to $10^5$, which corresponds to $^1H^+$ kinetic energies from at least ~ 1 keV to 1 GeV. Microdosimetric quantities can be calculated for a spherical target surrounded by a vacuum or for a monodirectional beam of ions emitted from a plane that passes through a water-equivalent material before reaching a spherical target. The latter geometry is intended to simulate monolayer cells attached to the bottom of a cell culture dish. The reported MCDS results in this paper are based on the former irradiation geometry.

In the MCDS, ions travel in a straight line until they have zero kinetic energy. The deterministic algorithm used in the MCDS accounts for stoppers within the treatment volume and for changes in ion stopping power within the target volume. It does not account for delta-ray escape from the target (all energy deposition events are considered local) nor does it account for delta-rays associated with ions passing near the target site that enter the site and deposit energy. For irradiation geometries other than the ones described above, the microdosimetry model included in the MCDS should be combined with a larger-scale, Monte Carlo transport simulations to account for secondary radiations(142). Such a hybrid Monte Carlo approach is especially important for indirectly ionizing photons and neutrons.

## Results

Since the RPWBA calculations provide important physical inputs to the present microdosimetric model, we first examine the reliability of these calculations, by comparing the present calculations for the proton stopping power and the energy-loss straggling factor ($\delta_2$) against other studies.

Figure 19 shows the proton stopping power (or unrestricted LET) of liquid water calculated from Eq. (34) using the present DRF model combined with the RPWBA for the energy range of 1 MeV−1 GeV. The calculations are compared against the SP data of the ICRU Report 90(101). The relative difference (%) is also presented in the same graph (solid blue line, right $y$-axis) using the ICRU Report 90 as the baseline for comparison.

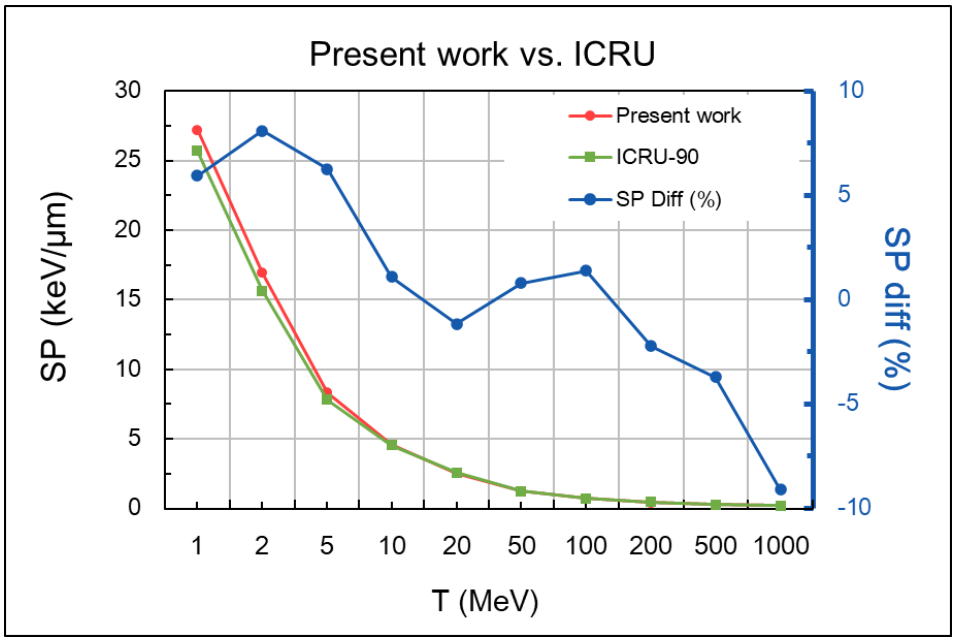


**Figure 19.** Proton stopping power (SP) for liquid water for the energy range 1 MeV – 1 GeV calculated in the present work by the RPWBA and the dielectric theory (red line) and compared against the data from ICRU Report 90 (green line). The blue line represents the relative difference (%) of the SP values using the ICRU data as a baseline.

Figure 20 (left panel) shows the dose-weighted energy that is deposited in the target in a single proton-electron collision ($\delta_2$) calculated by Eq. (56) for various proton energies (2, 5, 10, 20, 50, 100, 400, 600, 800, and 1000 MeV) in the domain of 1 MeV – 1 GeV and three target dimensions (10, 100, and 1000 nm) which correspond to distinct cut-off energies $\Delta$ $(0.18, 1.37, \text{and } 5.56 \text{ keV})$. The comparison of the present $\delta_2$ values against the Kellerer(129) and Xapsos (144) approaches is also presented in Figure 20 (right panel). A fitted equation for our results is presented as a function of the cut-off energy $\Delta$. The equation is represented as $\delta_2 = 0.0074 + 0.174\Delta^{0.651}$ (keV), which is valid for $\Delta \leq E_{max}$. The Xapsos results are obtained from $\delta_2 = 0195\Delta^{0.610}(149)$. Kellerer's approach assumes a $1/E^2$ secondary electron spectrum which yields $\delta_2 = \frac{\Delta}{2\ln(\Delta/I)}$, with $I = 0.078$ keV(101).

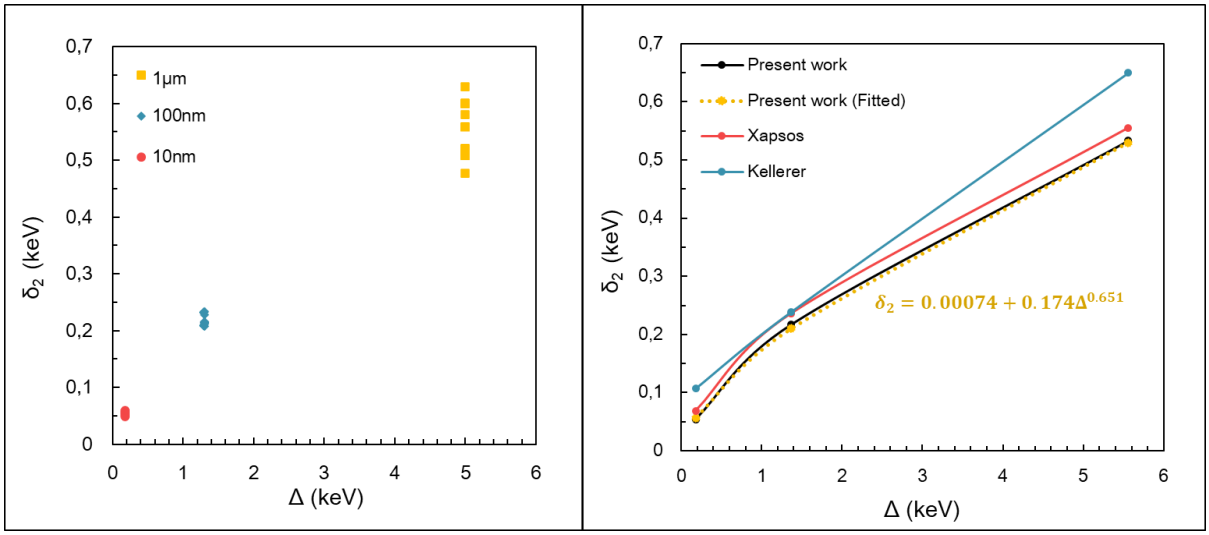


**Figure 20.** Left panel: Present work $\delta_2$ values for various proton energies (2, 5, 10, 20, 50, 100, 400, 600, 800, 1000 MeV) and distinct cut-off energies $\Delta$ corresponding to the three-sphere diameters (10, 100, 1000 nm) obtained from Eq. (56). Right Panel: $\delta_2$ values as a function of cut off energy $\Delta$, calculated by the approaches of Kellerer(127), Xapsos(144,163) and present work.

Figure 21 depicts the energy-loss straggling distributions for protons (of 1, 10, 100, and 1000 MeV) crossing a liquid water target sphere (diameter equal to 10, 100, and 1000 nm), as implemented into our microdosimetric model for determining $y_{D,dir}$ (i.e., the contribution of direct events in $y_D$).

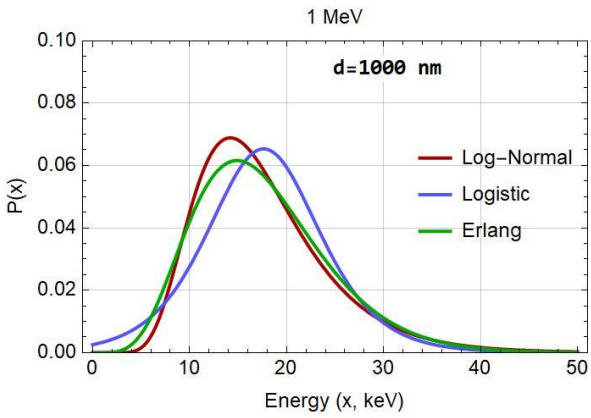
1 MeV
d=1000 nm
Log–Normal
Logistic
Erlang
P(x)
Energy (x, keV)

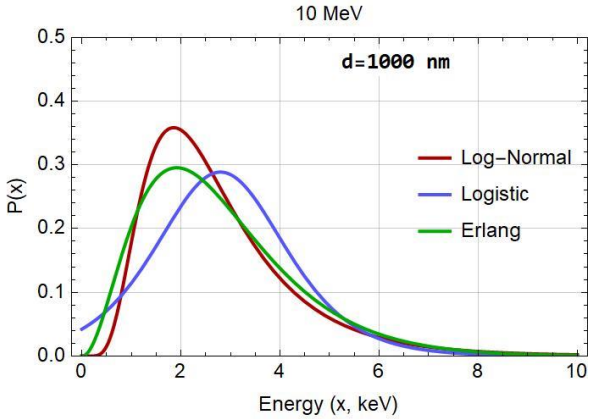
10 MeV
d=1000 nm
Log–Normal
Logistic
Erlang
P(x)
Energy (x, keV)

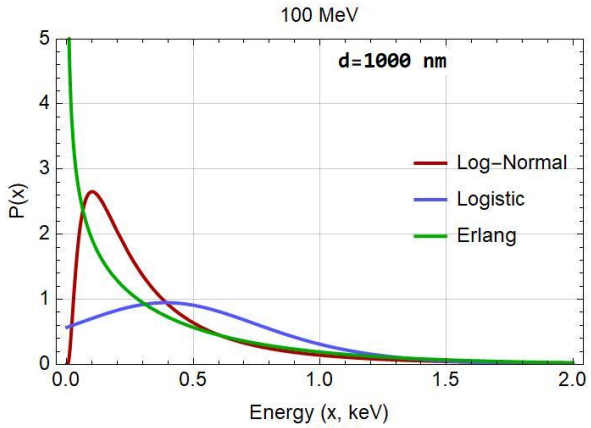
100 MeV
d=1000 nm
Log–Normal
Logistic
Erlang
P(x)
Energy (x, keV)

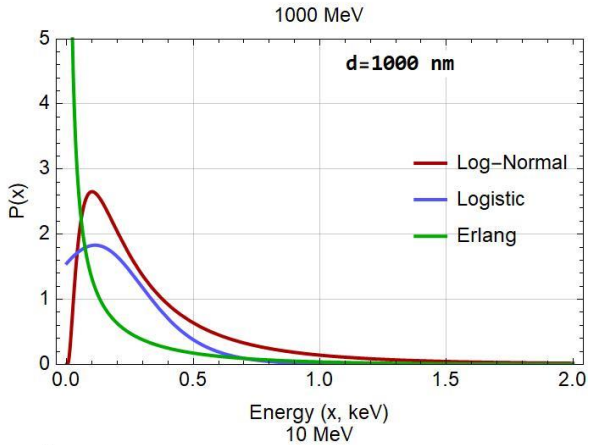
1000 MeV
d=1000 nm
Log–Normal
Logistic
Erlang
P(x)
Energy (x, keV)

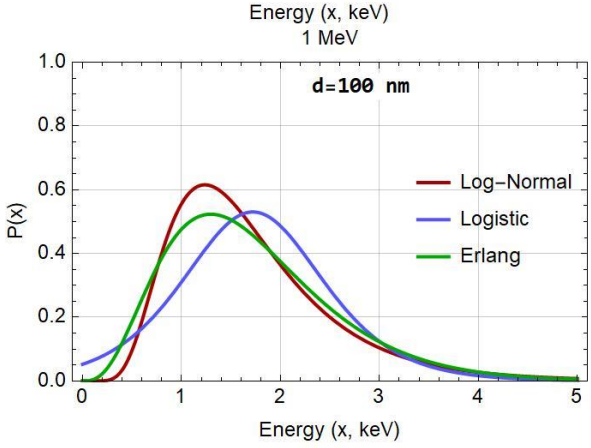
1 MeV
d=100 nm
Log–Normal
Logistic
Erlang
P(x)
Energy (x, keV)

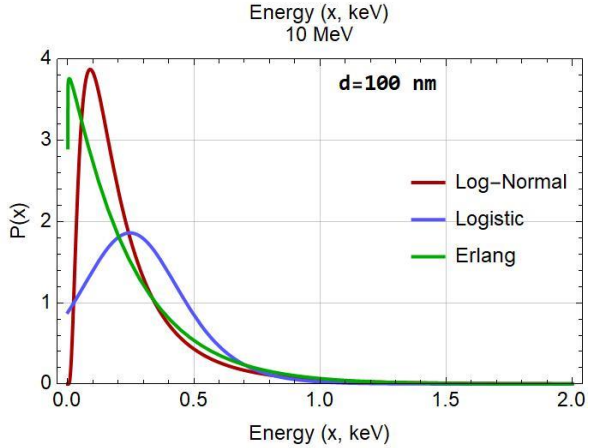
10 MeV
d=100 nm
Log–Normal
Logistic
Erlang
P(x)
Energy (x, keV)

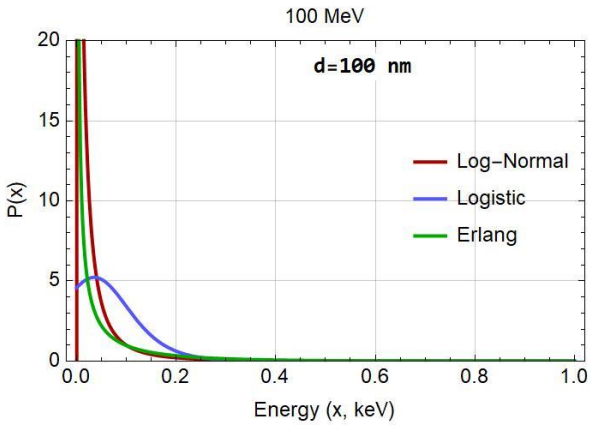
100 MeV
d=100 nm
Log–Normal
Logistic
Erlang
P(x)
Energy (x, keV)

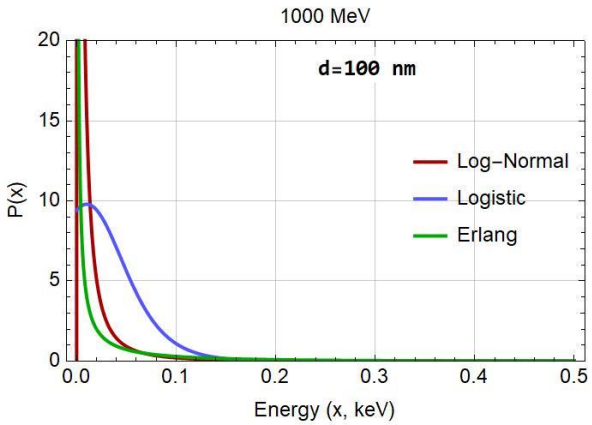
1000 MeV
d=100 nm
Log–Normal
Logistic
Erlang
P(x)
Energy (x, keV)

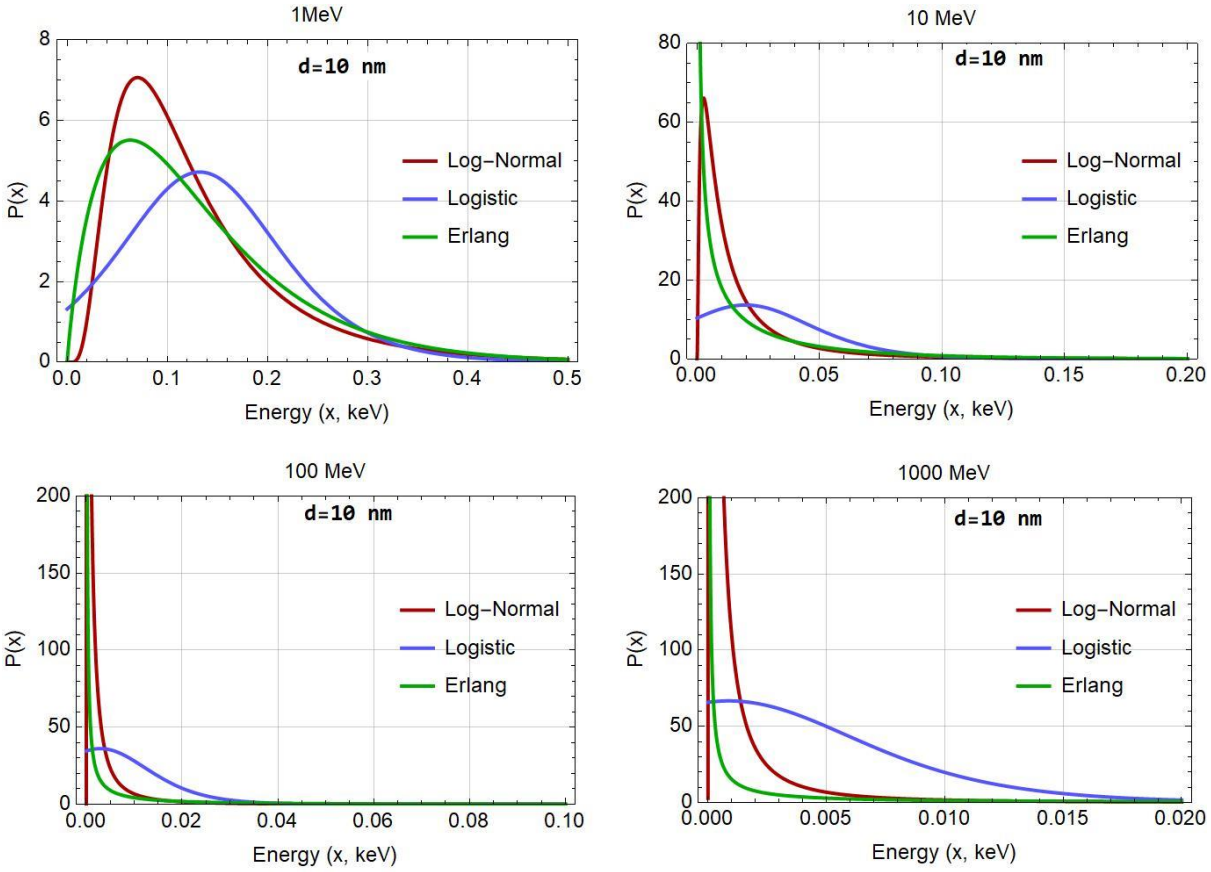


**Figure 21.** Energy-loss straggling distributions (Log-Normal, Erlang, Logistic) studied in this work, for 1, 10, 100 and 1000 MeV proton and three diameter spheres 1000 (panel a), 100 (panel b) and 10 nm (panel c).

Figure 22 depicts the $y_D$ for the proton energy range 1 MeV – 1 GeV and three liquid water spheres of different sizes (10, 100, and 1000 nm). The present calculations and the analytic models of Xapsos and co-workers are compared against MCTS simulations using PHITS (PHITS-KURBUC and PHITS t-sed), Geant4-DNA, and RITRACKS. Data from the quasi-deterministic model included in the MCDS are also shown in Figure 22. Note that the calculations of the $y_D$ by the present model are carried out using three different energy-loss straggling distributions (Log-normal, Erlang, Logistic). Also, the MCDS-based $y_F$ values were converted to an estimate of $y_D$ using the approximate formula $y_D = (9/8)y_F$ which holds for the idealized case where particles of constant LET traverse the target sphere by losing energy in a continuous manner(101).

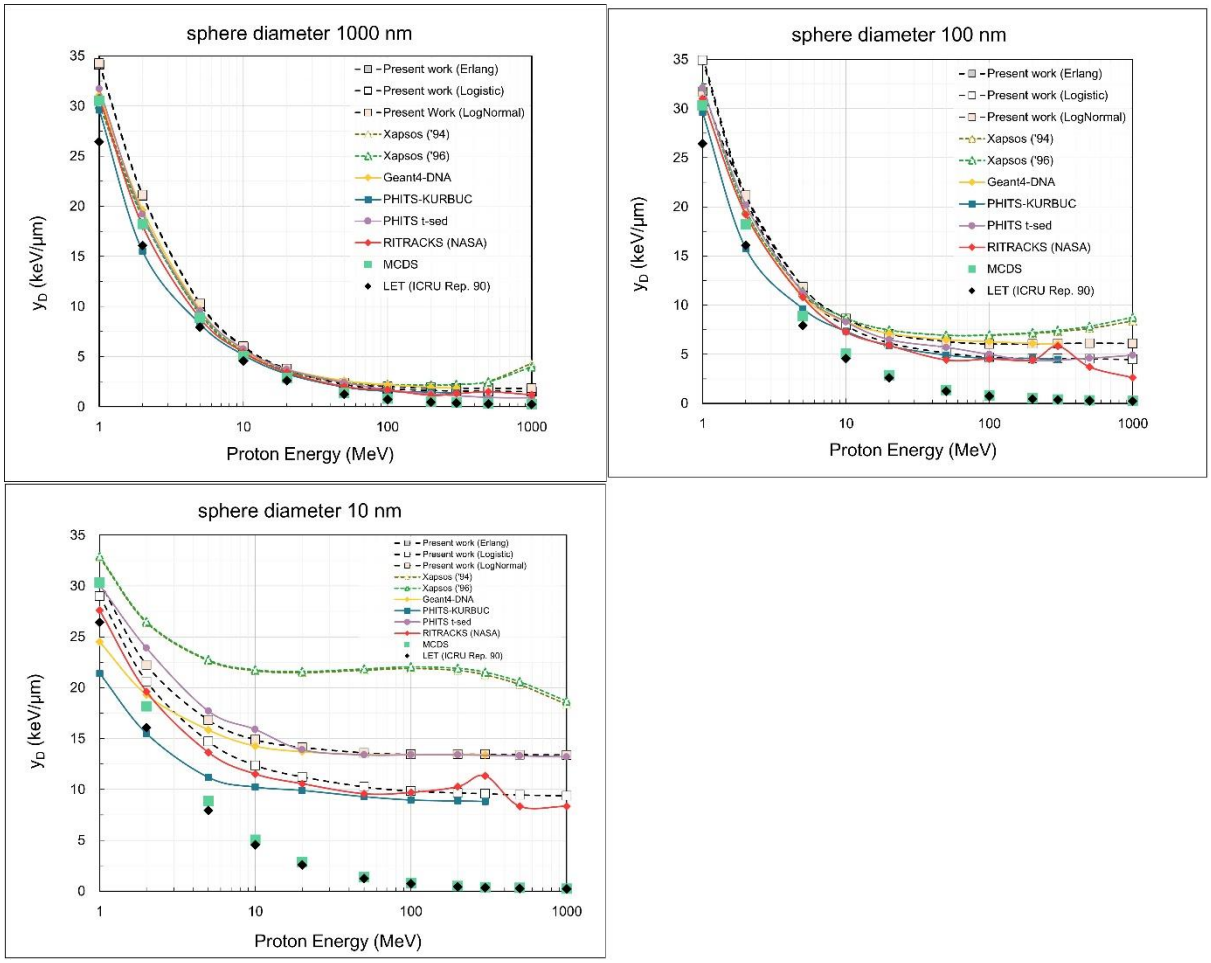


**Figure 22.** Dose-mean lineal energy ($y_D$) values for liquid water and various sphere diameters (10, 100, and 1000 nm) as a function of proton energy (1 MeV – 1 GeV), calculated by the microdosimetric models ("Present work" and Xapsos models), the MCTS codes (Geant4-DNA, PHITS-KURBUC, PHITS t-sed, and RITRACKS), and the MCDS. The LET values calculated from the ICRU Report 90 are also presented.

Figure 23 depicts, at each proton energy ($T_i$), the relative difference (RD) of the $y_D$ values of the analytic models and the MCDS algorithm against the arithmetic mean $y_D$ of the MCTS simulation data:

$$\mathrm{RD}\,(T_i) = \frac{y_D(T_i) - \overline{y_{D,\mathrm{MCTS}}(T_i)}}{\overline{y_{D,\mathrm{MCTS}}(T_i)}} \times 100\%, \qquad (66)$$

where $T_i$ is the i-th discrete energy value in the 1 MeV – 1 GeV interval and $\overline{y_{D,\mathrm{MCTS}}(T_i)}$ is the average $y_D$ of the MCTS codes at energy $T_i$. Note that the upper limit of application of Geant4-DNA and PHITS-KURBUC is 300 MeV, while for PHITS t-sed and RITRACKS, the upper limit is 1 GeV. Therefore, the value of $\overline{y_{D,\mathrm{MCTS}}(T_i)}$ for $T_i$<300 MeV is based on all four codes (Geant4-DNA, PHITS-KURBUC, PHITS t-sed, RITRACKS) whereas the value of $\overline{y_{D,\mathrm{MCTS}}(T_i)}$ for $T_i$>300 MeV is based only on data by RITRACKS and PHITS t-sed.

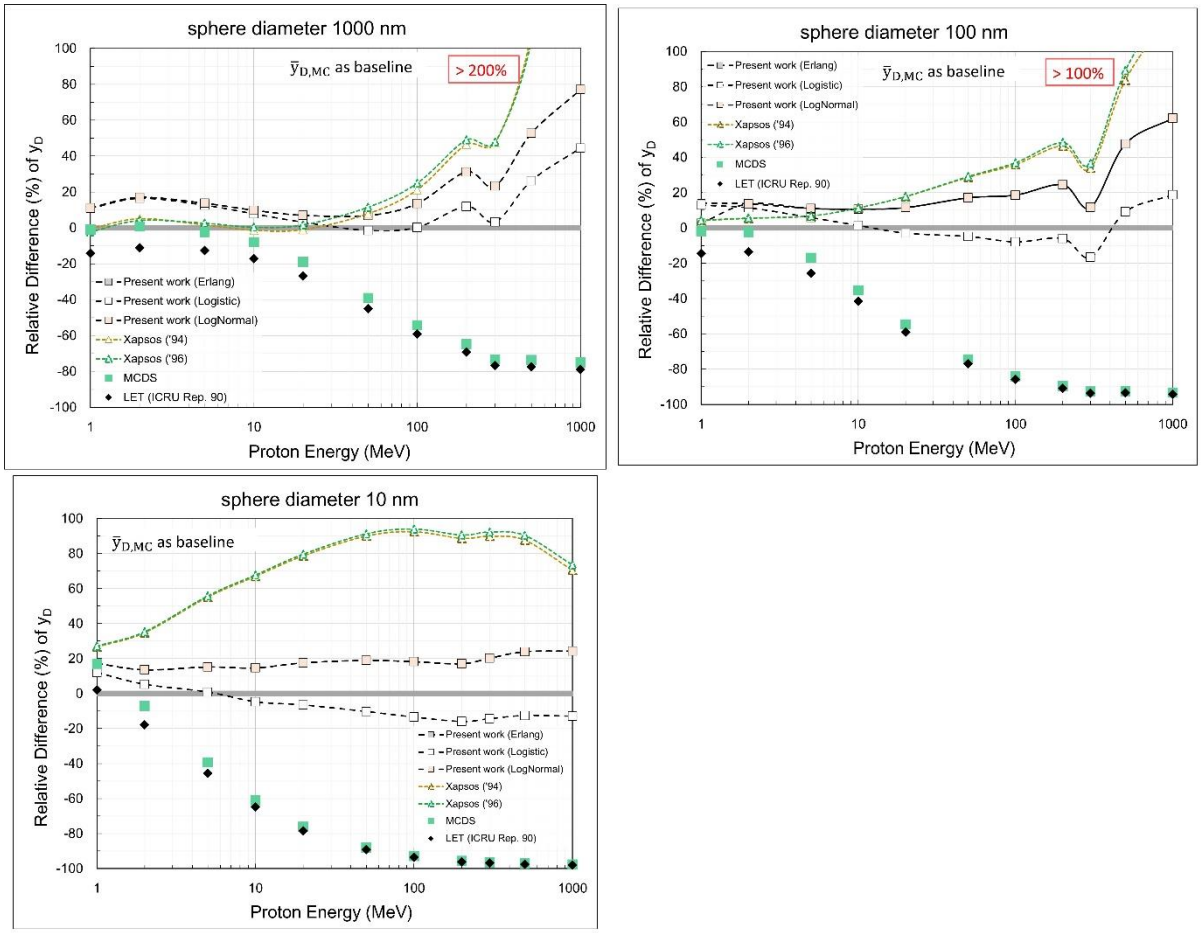


**Figure 23.** Relative difference (%) of the $y_D$ values of the analytic models and the MCDS algorithm against the mean $y_D$ of the MCTS codes for each proton energy (see Figure 22 and Eq. (66)).

To obtain a single-value indicator of the discrepancy among the various $y_D$ datasets, the RD is averaged over the proton energies and depicted in Figure 24 as the mean percentage deviation (MPD):

$$\mathrm{MPD} = \frac{1}{N}\sum_{i}^{N} \frac{|y_D(T_i) - \overline{y_{D,MCTS}(T_i)}|}{\overline{y_{D,MCTS}(T_i)}} \times 100\%, \qquad (67)$$

where $T_i$ is the *i*-th discrete energy value in the 1 MeV – 1 GeV interval, $\overline{y_{D,MCTS}(T_i)}$ is the average $y_D$ of the MCTS codes at energy $T_i$, and N is the total number of discrete energies ($T_i$) considered in this study.

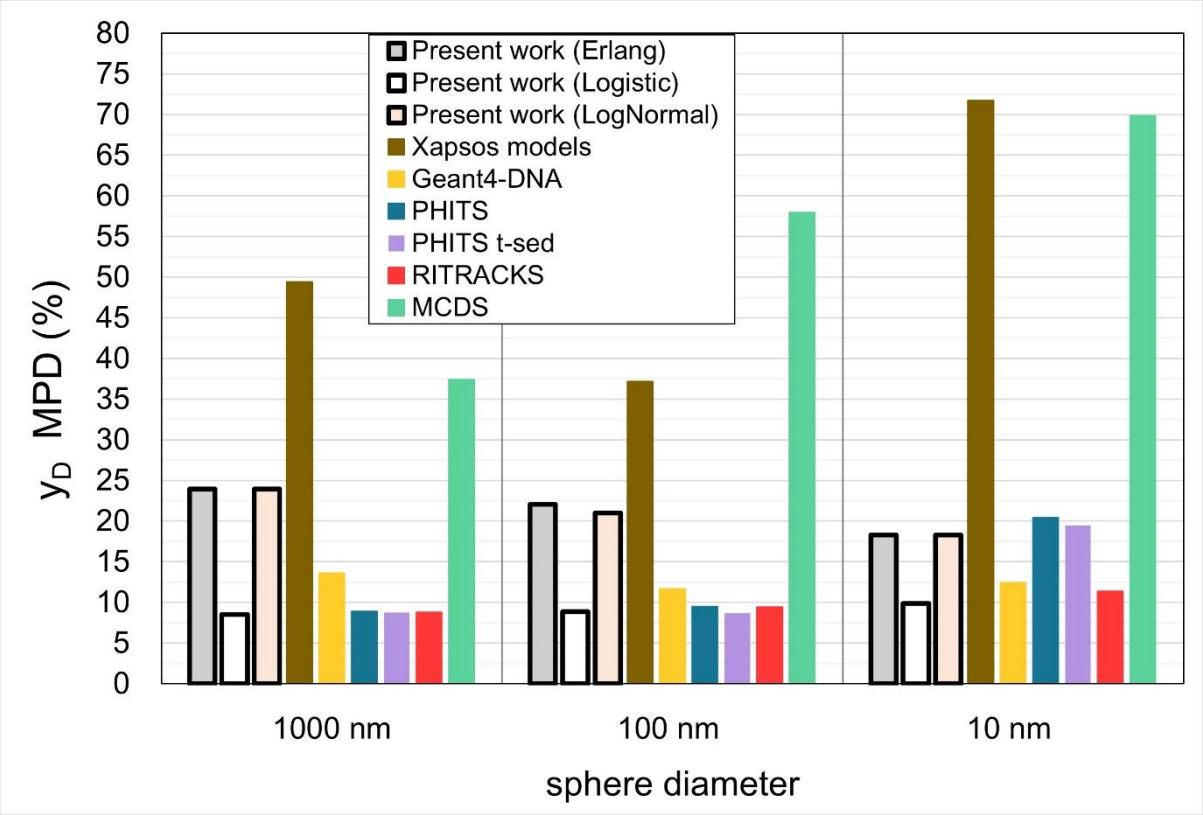


**Figure 24.** Mean percentage deviation (MPD) calculated by Eq. (67) for each $y_D$ dataset. The mean $y_D$ of the MCTS codes is used as baseline in the calculation of the MPD.

Figure 25 presents the weighted $(1 - f_{ion})$ indirect contribution ($y_{D,ind}$) to $y_D$ (see Eq. (26)) relative to the total $y_D$ for the present microdosimetric model and the three energy-straggling distributions (Erlang, Log-normal, and Logistic) used in this work, for the three sphere diameters (10, 100, and 1000 nm). Note that the Log-normal and the Erlang distribution yield very similar $y_D$ values.

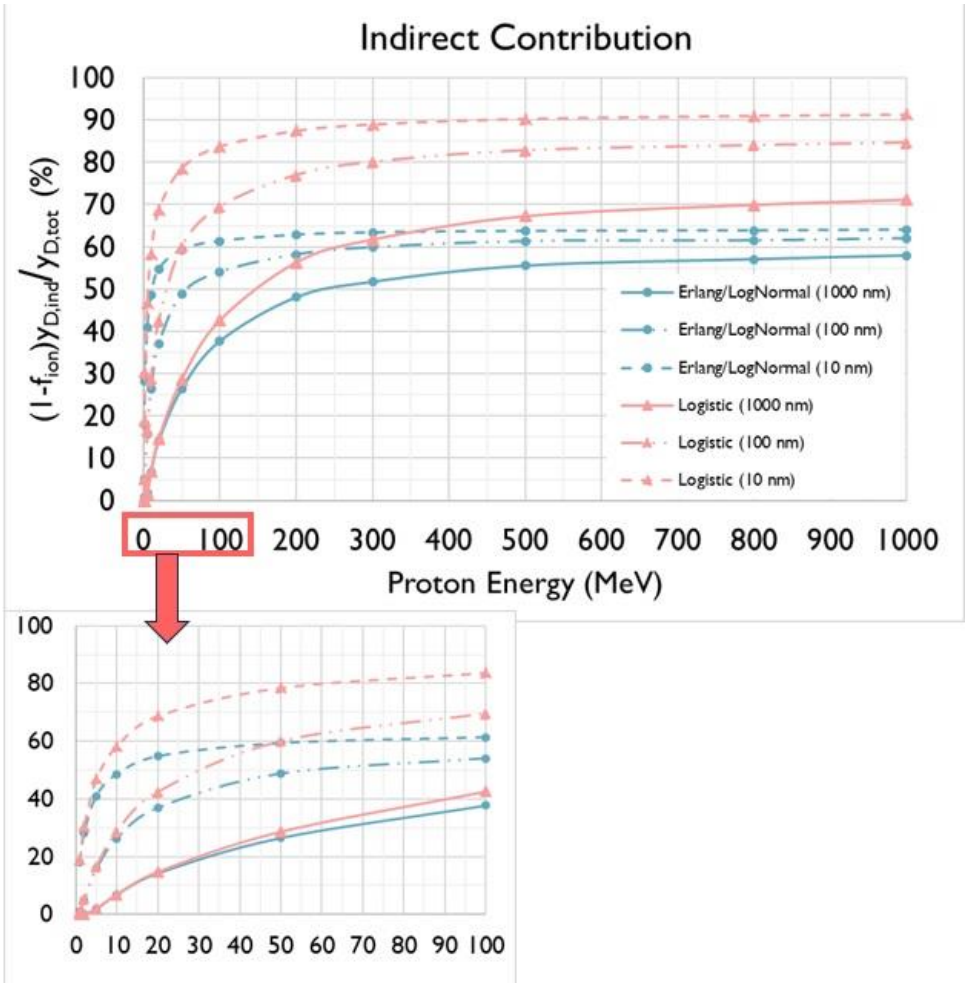


**Figure 25.** Contribution (%) of the indirect part of the dose-mean lineal energy ($y_{D,ind}$) relative to the total $y_D$ (see Eq. 26) for the three energy straggling distributions (Erlang/Log-Normal and Logistic) examined in the presented microdosimetric model and the three sphere diameters (1000, 100, and 10 nm). The results for the Erlang and Log-Normal distributions are practically identical.

The $y_D$ values obtained by the different approaches examined in this work (microdosimetric models, MCDS, and MCTS simulations) were used to calculate the variation of proton Q values over the energy range 1 MeV – 1 GeV based on the TDRA approach (Eq. (20)). The TDRA-based Q values are depicted in Figure 26.

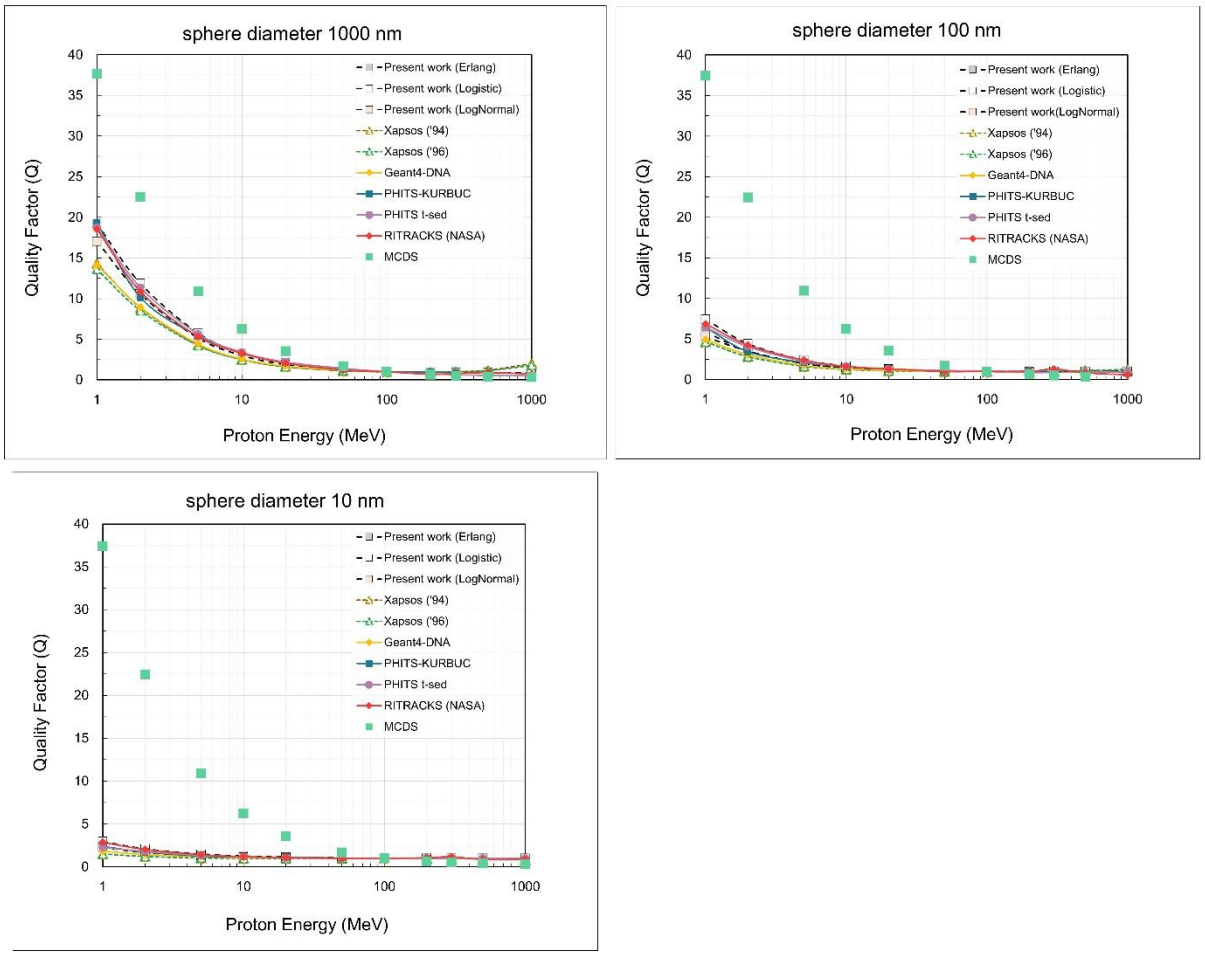


**Figure 26.** TDRA-based Q values for different liquid water spheres (diameters 10, 100, and 1000 nm) over the proton energy range 1 MeV – 1 GeV. The $y_D$ data used as input to TDRA are obtained from the analytic models, the MCDS and the MCTS simulations (see Fig. 22). The proton energy at 100 MeV was used for normalization (i.e., Q=1 at 100 MeV).

## Discussion

The aim of the present work is the development of an improved microdosimetry-based analytic model for the calculation of proton $y_D$ values in sub-micron target volumes over a broad energy range (1 MeV – 1 GeV) and the comparison with MCTS simulations. The dielectric formulation of the RPWBA has been used to determine the model parameters, like the energy-loss straggling factor ($\delta_2$) and the characteristics of the delta-ray spectrum. The RPWBA calculations have been benchmarked against the latest stopping power values for liquid water from ICRU Report 90 showing an agreement better than 10% over the whole energy range from 1 MeV to 1 GeV (see Figure 19).

As it is illustrated in Figure 20 (left panel), the straggling factor ($\delta_2$) calculated using Eq. (56) is almost independent of proton energy in the case of small spheres (10 nm and 100 nm) but exhibits a sizeable variation with proton energy for the 1000 nm sphere. A previous study (144) has shown that if the penetration range of the most energetic electrons ($E_{max}$) exceeds the target dimensions, then $\delta_2$ becomes a function of the sphere diameter (or cut-off energy $\Delta$ in this case) but does not depend (or slightly depends) on the ion energy. This is also confirmed in our study (see Figure 20). Thus, the use of an average $\delta_2$ value (as in our fitted equation; Figure 20 right panel) is well justified. However, the straggling factor ($\delta_2$) has a stronger effect on the energy-loss straggling variance ($V_\delta$) (and on $y_D$) for high-energy protons (>10 MeV) and smaller targets (<100 nm)(53,144). The $\delta_2$ values calculated in the present work using Eq.

(56) are smaller than those obtained by Kellerer's approach for all sphere diameters. This can be explained by the fact that the present approach is better suited to calculate the small energy transfers (leading to low-energy secondary electrons) as compared to Kellerer's $1/E^2$ approximation which only holds for high energy transfers.

The performance of the present analytic model for the calculation of proton $y_D$ values in sub-micron volumes of liquid water is examined in Figures 22 and 23 by comparing against the conventional Xapsos models, MCTS simulations (Geant4-DNA, PHITS, RITRACKS), and the MCDS code. At first, we should note that, despite the alternative methodologies (and irradiation geometry-specific factors) used to calculate y as well as the somewhat different interaction models adopted, the MCTS codes are in fair agreement, with differences being overall up to ~10–20% throughout the present energy range (1 MeV – 1 GeV) and target dimensions (10–1000 nm) studied. As expected, the largest discrepancies (~20%) among the MCTS codes are observed for the smallest volume of 10 nm, while the agreement improves (~5–10%) as the target volume increases to 100 and 1000 nm. On the other hand, the differences between the MCDS and the MCTS codes are increasing with proton energy (for all target volumes), becoming particularly large (~50–100%) for protons energies above several tens of MeV. These trends are consistent with the fact that the LET-based MCDS quasi-deterministic algorithm (mentioned above) neglects energy-loss straggling and delta-ray effects (i.e., delta-ray escape from the target, as well as delta-ray influx to the target from protons passing near the target) which become important with increasing proton energy.

The results of Figure 23 also reveal that, regardless of the energy-loss straggling distribution (Log-Normal, Erlang, Logistic), the $y_D$ values obtained by the new model are in much better agreement with the MCTS data as compared to the conventional Xapsos models. The latter tend to hugely overestimate (by more than 100%) the MCTS data above a few hundred MeV, even for the large target spheres. Importantly, the improved performance of the present model becomes more evident as the sphere diameter decreases, especially for the 10 nm sphere which may be considered biophysically most relevant. It can also be revealed from Figure 23 that an important improvement in the present model is caused by the replacement of the Log-Normal by the Logistic distribution to describe energy-loss straggling. The latter brings the present $y_D$ calculations consistently closer to the average $y_D$ of the MCTS data, as compared to the use of the Log-Normal (or the Erlang) distributions. The differences between the present model and the Xapsos models can be primarily attributed to the method used to calculate the $y_D$ for indirect events (and less so to the $\delta_2$ values) as can be seen from Figure 24 under the same energy-loss straggling distribution (i.e., Log-Normal). The strong influence of the indirect contribution ($y_{D,ind}$) to the total $y_D$ of Eq. (26), is illustrated in Figure 25.

A simple indicator of the overall performance of the different $y_D$ datasets is the MPD value calculated by Eq. (67) and presented in Figure 24. Note that the average $y_D$ of the MCTS data was used here as the baseline for the MPD calculations. Clearly, the new model yields a much lower MPD compared to the conventional Xapsos models, irrespective of the straggling distribution used. Specifically, the Xapsos models have an MPD between 37–72% whereas the present model has an MPD between 8–24%, with the exact value depending upon the straggling distribution used (Erlang, Logistic, or Log-Normal). Specifically, the Logistic distribution yields the lowest MPD (8–10%) whereas the Erlang and Log-Normal distributions yield a somewhat higher MPD (18–24%). Thus, it is recommended that the present model is being used with the Logistic distribution. The quasi-deterministic algorithm of MCDS has an MPD of 37–70%, comparable to the Xapsos models. Intriguingly, the MPDs of the MCTS codes are in the range 8–20%, i.e., they are comparable to the MPDs of the present model. In other words, the present analytic model with any of the three straggling distributions, performs (with respect

to $y_D$ calculations in the examined energy and target-size range) similarly to the examined MCTS codes. It is noteworthy that, especially for the 10 nm sphere which may be most relevant to the simulation of DNA damage, the present model with the Logistic distribution exhibits the lowest MPD from all $y_D$ datasets studied.

Using the $y_D$ datasets presented in Figure 22, it is straightforward to calculate TDRA-based Q values based on Eq. (20). The discrepancies of Q become gradually significant (especially for MCDS) below a few tens of MeV, for all spheres. At the intermediate energy range (~50–500 MeV) the resulting Q values are nearly insensitive to the $y_D$ dataset. Small (or moderate) discrepancies are also observed at the high energy end (~1 GeV). It is noteworthy that the Q values calculated by the present model fall within the range of Q values obtained by the MCTS codes.

In summary, both the $y_D$ and Q values calculated by the present model greatly reduce the discrepancy against the MCTS simulation data (bringing it down at the 10–20% level) compared to the existing Xapsos models, with the cost of a moderate increase of computational effort.

**Conclusion**

An improved microdosimetry-based analytic model is presented that allows the calculation of the dose-mean lineal energy ($y_D$) in sub-micron liquid water spheres over a broad range of proton energies (1 MeV – 1 GeV) in good overall agreement (at the ~10% level) with state-of-the-art MCTS codes (Geant4-DNA, PHITS, and RITRACKS). Results from the MCDS quasi-deterministic algorithm highlight the limitation of LET-based calculations for sub-micron volumes irradiated by MeV–GeV protons. TDRA-based calculations of the radiation protection quality factor (Q) are reported, highlighting its sensitivity to the size of the target volume as well as the $y_D$ dataset at low proton energies. It is envisioned that the present model might be used as a reliable alternative to time-intensive MCTS simulations for practical calculations of $y_D$ (and Q) in both medical and space applications with an accuracy comparable to state-of-the-art MCTS codes.

# Chapter 6

**Summary**[4]

To calculate the different cancer risk metrics of Risk of Exposure Induced-Cancer (REIC), Risk of Exposure Induced Death (REID) and Radiation Attributed Decrease of Survival (RADS) employed and proposed by space agencies of NASA and ESA, using the microdosimetric Q of Theory of Dual Radiation Action (TDRA) and an improved analytical model calculation of the $y_D$ values of space radiation ions. The OLTARIS platform was utilized to characterize the radiation environment in space for three space missions (to Mars and the Moon). The flux of GCR behind typical shielding of aluminium (20 g/cm$^2$) and 30 cm of water was registered for solar minimum and maximum conditions. Subsequently, an enhanced analytical microdosimetric model, considering energy-loss fluctuations and penetration depth of secondary electrons into the target, was employed to calculate the lineal energy spectrum, f(y), and $y_D$ values of ions from protons to iron, for energies spanning from 1 MeV to 1 GeV. The target was assumed to be a water sphere with dimensions of 1μm. The recorded flux and $y_D$ values were then used to compute the mean microdosimetric Q of each space mission, using the modified TDRA biophysical model. Additionally, risk metrics proposed by NASA and ESA, namely REIC (%), REID (%) and RADS (%), were computed, and their sensitivity to various parameters was examined.

[4] Chapter 6 is based on the paper (*to be submitted*) of Papadopoulos et al. Space radiation cancer risk assessment for astronauts using analytical model calculations for the microdosimetric radiation quality factor.

**REIC, REID and NASA's cancer risk methodology**

The general methodology for the calculation of the risk metrics Risk of Exposure Induced-Cancer (REIC) and Risk of Exposure Induced Death (REID) as first represented by Vaith and Pierce(206) includes the following steps:

- **Space radiation fluence spectrum.** The particle fluence spectrum for each particle, energy and organ is necessary in order to calculate the specific absorbed organ dose (D) and evaluate the risk metrics.
- Choose a **background survival curve** representative for an astronaut population. Life tables are needed for all-cause mortality data for a specific time period and a selective population, in order to calculate the survival curves. Generally, a non-smoking population is more representative for the astronauts since they are extremely healthy workers.
- **Background** population statistics for tissue specific **cancer incidence and mortality** and LSS cancer incidence rates. These data are necessary for the extrapolation of risk that is known in the LSS cohort to the astronauts of different nationality (Japanese to other country's population). Once again, a non-smoking cancer incidence/mortality background population is needed, although this is a difficult task (148). There are many tissues (pancreas, lungs, stomach, colon etc.) that are smoking-sensitive, so adjustments in incidence/mortality rates of the general background population must be done in these tissues to have a more realistic reference population for the astronauts.
- **Excess radiation induced-cancer risk models**. These models are based on human cohorts (mainly from atomic bomb survivors) that are exposed mostly to Low-LET radiation (and high LET neutrons) and estimate the excess cancer risk due to the irradiation of the individuals. These estimations are usually expressed in terms of the multiplicative and the additive excess risk models. The multiplicative model or excess relative risk model (ERR) estimates the increased cancer risk to the radiation exposure population relative to the unexposed background. It considers that the cancer risk of the exposed to radiation population increases proportionally to the background cancer rates. That means that ERR estimates are related to the background rates. The excess additive risk model or excess absolute risk model (EAR), unlike the ERR model, is not related to the background population rates and estimates the absolute increase of cancer cases, i.e., as the exposure increases, the risk is additively greater relative to the background(16,148,207,208).
- **Transfer weights** for additive and relative excess risk models. These weighting factors determine how many of the different cancer types contribute with a multiplicative (ERR model) or additive (EAR) model. For the ERR model the transfer weight is $\nu_T$, whereas for the EAR model the transfer weight is $1 - \nu_T$(207,209).
- **Radiation Quality factor** according to the LET approach of ICRP Report 60(24) or NASA model utilizing the track structure parameter $(Z/\beta)^2$ (15). In this work the microdosimetric quality factor according to the TDRA methodology has been utilized (see Eqs. (20-21)).
- **Dose and dose rate reduction factor (DDREF)**. The LSS population has been exposed to high dose rates and a scaling is required for the chronic low dose-rates for astronauts of space radiation exposure for the reduction of the excess cancer risk. A scaling to low from acute doses may also be made, as many missions will have less than 1 Gy-Equivalent, which was estimated from the LSS. Generally, excess cancer risks models (EAR or ERR) for solid cancers, assume a linear response to cancer risk, however an appropriate value of DDREF must be applied for low doses to decrease even more the

cancer risk, as it is not intrinsic in the EAR/ERR models. For leukemias, a linear-quadratic response model was utilized, but the linear part can adequately characterize the excess cancer risk in low doses. As a result, a DDREF value is only needed for solid cancers and not for leukemias. The most common exploited values for the DDREF are 1.5 by BEIR VII studies(209), 2 by ICRP Report 103 (99) and NCRP Report 132 or 2.5 by NCRP Report 98(2,8).

REIC and REID can be calculated by folding the survival curve for the background population adjusted for deaths caused by radiation with the excess cancer incidence or mortality rate of each tissue(208,210).

$$\mathrm{REIC} = \int_{a_E+l}^{a} \lambda_{I,t}(a_E, a, D, Q, \mathrm{DDREF}) \times S_{adj}(a_E, a), \tag{68}$$

$$\mathrm{REID} = \int_{a_E+l}^{a} \lambda_{m,t}(a_E, a, D, Q, \mathrm{DDREF}) \times S_{adj}(a_E, a). \tag{69}$$

Where t is the specific tissue, $a_E$ is the age at the time of exposure, a is the attained age, which is in this work is set to 100 years old, D is the absorbed dose, Q the quality factor, and $l$ is the latency period for the manifestation of each cancer type. Generally, the LSS data of the survivors indicated that for solid cancer types the latency period is 5 years, but for leukemia the period is 2 years(15,148).

$S_{adj}(a_E, a)$ is the background survival curve adjusted for the deaths caused by radiation exposure. It can be described by the conditional probability of surviving from age $a_E$ to attained age $a$ multiplied by a hazard term:

$$S_{adj}(a_E, a) = \frac{S_o(a)}{S_o(a_E)} e^{-\int_{a_E}^{a} \lambda_{m,t}(a_E, a', D, Q, \mathrm{DDREF})\, da'} . \tag{70}$$

Where $S_o$ is the representative unexposed background survival curve and $a'$ is a dummy variable. For this work, the background unexposed survival curve was retrieved for the average US population life timetables from Arias 2020 data(211).

For the background incidence and mortality cancer data for males and females, Centers for Disease Control (CDC) WONDER(212) has been utilized for the US population and for the period of 2010-2020. We have grouped the cancers in three types: solid cancers, lungs and leukemia. Although different tissues have different radiosensitivity, we have grouped these three categories, as all tissues were simulated with a liquid water sphere of 1μm for all tissues (see next section). For leukemias the exclusion of the DDREF value, and the EAR/ERR models which differ from solid cancers are enough to make the separation.

To analyse lung cancer incidence in the context of smoker and non-smoker populations, we delineated the methodology due to distinct REIC/REID calculations for each group. Recognizing the disparity between smokers and non-smokers, especially in the unique case of astronauts where a non-smoker profile is more relevant, we applied the NASA approach to estimate lung cancer incidence in the non-smoking demographic. The approach involved considering the population as a composite of former-smokers (FS), current smokers (CS), and non-smokers (NS), with prevalence data (f) sourced from Thun et al. 2013 [210]. Subsequently, the relative risk (RR) of lung cancer mortality among CS and FS was determined using the NS

population as the baseline. For incidence RR, we converted the mortality RR by utilizing a lethality factor of 0.89 (213). The lung cancer incidence rate for a mixed population of smoking status was calculated using the subsequent equation (213):

$$RR_{tot} = f_{CS}RR_{CS} + f_{FS}RR_{FS} + f_{NS}\,. \quad (71)$$

The calculation of the non-smoking attributable factor (NSAF) was conducted using the formula $NSAF = \frac{1}{RR_{total}}$. This factor was subsequently applied by multiplying it with the lung cancer incidence rates, resulting in adjusted rates specific to the non-smoking population for each gender and age group.

The cancer incidence rate was calculated using a mixture model (EAR and ERR excess cancer risk models) after applying an appropriate value for the transfer weight $\nu_T$ guided by BEIR VII Report, for the absorbed Dose (D), DDREF and the quality factor (Q). It can be described by [205,210]:

$$\lambda_{I,t}(a_E, a, D, Q, DDREF) = \frac{D \times Q}{DDREF} \times \left[\nu_T \times ERR(a_E, a) \times \lambda_{0,I,t}(a) + (1 - \nu_T) \times EAR(a_E, a)\right], \quad (72)$$

where $\lambda_{0,I,t}(a)$ is the tissue specific cancer incidence rate in the background population, $\nu_T$ is the tissue-specific transfer model weight, $ERR(a_E, a)$ is the excess relative cancer risk per 1 Sievert and $EAR(a_E, a)$ is the excess additive risk per 1 Sievert.

The functions of the ERR and EAR (per $10^4$ PY Gy) models for all solid cancers, as a function of age at exposure $a_E$ and attained age $a$ that were used for present calculations, were retrieved from Cucinotta et al. 2020 (207):

$$ERR(a_E, a) \text{ or } EAR(a_E, a) = \rho\left(\frac{a}{70}\right)^{\eta} e^{\gamma(a_E - 30)}\,. \quad (73)$$

The central values of the parameters for the ERR and EAR functions and both sexes are obtained from RERF 2007(207) with confidence level 90% and are given in Table 11 for all solid cancers and lungs.

**Table 11.** Parameter values of the ERR and EAR functions for both sexes, obtained from the RERF 2007 with 90% CL and Cucinotta et al. 2020 [210].

| **Parameter values** | **ERR function Solid Cancers** (males/females) | **EAR function Solid Cancers (per $10^4$ PY Gy)** (males/females) | **ERR function Lungs** (males/females) | **EAR function Lungs (per $10^4$ PY Gy)** (males/females) |
|---|---|---|---|---|
| $\rho$ | 0.35/0.58 | 43/60 | 1.2/0.42 | 2.3/3.4 |
| $\eta$ | −1.65/−1.65 | 2.38/2.38 | −2.5/−2.5 | 5.2/5.2 |

| | | | | |
|---|---|---|---|---|
| $\gamma$ | $-0.0186$ $/-0.0186$ | $-0.0274$ $/-0.0274$ | $-0.007/-0.007$ | $-0.41/-0.41$ |

For leukemia, the ERR and EAR (per $10^4$ *PY Gy*) functions were calculated by [210]:

$$\mathrm{ERR}(a_E, a, D) = 1.15(1 + 0.87 \times D)e^{-0.4\left(\frac{a_E-30}{10}\right)-0.48\,\mathrm{Log}\left(\frac{a-a_E}{25}\right)+0.42\left(\frac{a_E-30}{10}\right)\mathrm{Log}\left(\frac{a_E-30}{25}\right)}, \quad (74)$$

$$\mathrm{EAR}(a_E, a, D) = 1.25(1 + 0.88 \times D)e^{-0.29\left(\frac{a_E-30}{10}\right)+0.56\left(\frac{a_E-30}{10}\right)\mathrm{Log}\left(\frac{a-a_E}{25}\right)}. \quad (75)$$

The cancer mortality rate of each tissue was calculated for all cancers using the BEIR VII Report (209) that scales the incidence rate of the exposed population to the mortality/incidence of the population under study[213-215]:

$$\lambda_{m,t}(a_E, a, D, Q, \mathrm{DDREF}) = \frac{\lambda_{0,m,t}(a)}{\lambda_{0,I,t}(a)}\lambda_{I,t}(a_E, a, D, Q, \mathrm{DDREF}). \quad (76)$$

The transfer weight $\nu_T$ values for solid cancers and leukemia were 0.7, while for lung cancer the value of choice was 0.3 (148,207).

**RADS and ESA's radiation risk assessment**

ESA adheres to ICRP Report 60 recommendations without having developed a concluded cancer risk model, setting the career dose limits for astronauts the value of 1 Sv, resulting from a 20-year astronaut career and an upper limit of 50 mSv/year for radiation workers. Nevertheless, these dose limits need reassessment, as the International Commission on Radiological Protection (ICRP) recommendations established the limit of 20 mSv/year for radiation-exposed workers on Earth(99). It has also been proposed by research [212-213] to use the cumulative risk quantity of radiation attributed decrease of survival (RADS) as the main risk metric for ESA. Following the recommendations of the ESA Topical Team for space radiation, RADS, which is the basically the cumulative cancer risk, is an alternative to REIC which is free of the survival curves and its uncertainties and reduces the epidemiological requirements. The greatest uncertainty with the survival function is that the population statistics must be well selected to be accurate for a non-smoking population and can be projected in the future. However, background incidence cancer rates are mandatory for the calculation of RADS, as well as it does not consider the competing risks, which results in increasing RADS values with increasing attained age(213,217).

It can be calculated by the following equation [209,214]:

$$\mathrm{RADS}(a_E, a, D, Q) = 1 - e^{-\int_{a_{E+1}}^{a} \lambda_{I,t}(a_E, a', D, Q, \mathrm{DDREF})\,da'}, \quad (77)$$

where the exponential power term is the hazard function, $\lambda_{I,t}$ is the tissue specific incidence cancer rate, given by Eq. (72). The practical interpretation of RADS, is that it represents the relative decrease of the unknown survival curve at a certain attained age ($a$) after irradiation.

An additional parameter employed to quantify the deleterious impact of radiation exposure is the concept of "*Years of Life Lost*" (YLL), which delineates the diminished lifespan of an astronaut (or population). It is a practical concept that reflects to the effects of radiation exposure to humans. Its computation involves(213,217):

$$\mathrm{YLL} = \int_{a_E+1}^{a} \frac{S_o(a')}{S_o(a_E)} \left(1 - e^{-\int_{a_E+1}^{a} \lambda_{I,t}(a_E,a',D,Q,DDREF)da'}\right)da'. \quad (78)$$

**Mission parameters and mission quality factor (Q)**

To assess the space radiation environment resulting from Galactic Cosmic Rays (GCR) and its interaction with shielding, the OLTARIS online software, developed by NASA, was employed (161). Three mission scenarios were examined, each under typical solar maximum and minimum conditions. These scenarios included a swing-by mission to Mars lasting 600 days, a long-stay mission to Mars lasting 940 days, and a lunar mission lasting 90 days, as outlined in previous literature(218). In all these missions, a standard spherical aluminium shielding of 20 $\mathrm{g/cm^2}$ was taken into consideration. The GCR spectrum at free space (1 AU) spanning from $Z = 1$ to $Z = 26$ and energies ranging from 1 MeV to 10 GeV was calculated using the Badhwar-O'Neill 2020 model and was propagated through the aluminium shielding and an additional 30 cm of water. The recorded particle flux in the end of the water sphere were then used to calculate the mean quality factor (Q) for each mission scenario, as it will be described below.

The Q value mission was calculated by integrating the ion $Q_Z(E)$ across the complete energy spectrum and adjusting for their respective contributions to the overall dose. The computation involved summing up the values for all ion charges within the range of $Z = 1$ to $Z = 26$, as per the following equation:

$$\overline{Q}_{\mathrm{mission}} = \frac{\sum_Z \int_{E_{min}}^{E_{max}} Q_{TDRA,Z}(E)\, D_Z(E)\, dE}{\sum_Z \int_{E_{min}}^{E_{max}} D_Z(E)\, dE}, \quad (79)$$

where $Q_{TDRA,Z}(E)$ is the quality factor of an ion with charge Z and energy E calculated by TDRA and Eq. (21), $D_Z(E)$ is the corresponding absorbed dose of each ion with energy E, and the limits of integration are set at $E_{min} = 1$ MeV and $E_{max} = 1$ GeV.

The mean dose equivalent for each mission was then calculated by:

$$\overline{H} = D_{\mathrm{mission}} \times \overline{Q}_{\mathrm{mission}}. \quad (80)$$

Equation (80) was then implemented to Eqs. (68), (69) and (77) to calculate the risk metrics of REIC, REID and RADS.

**Results**

In this study, we computed the risk metrics of REIC, REID, and RADS for three distinct mission scenarios. The core metrics results, unless stated otherwise, were computed using the average microdosimetric quality factor $\overline{Q}_{\mathrm{mission}}$ of the TDRA approach for each mission, the mixture of the ERR/EAR functions in Table 11 for solid cancers, leukemia and lung cancer (adjusted to non-smokers), while the choice of the DDREF value was set to 2.

Table 12 presents the REIC (%) and REID (%) calculations for both sexes and two different ages at exposure (30, 40) during solar minimum conditions for the three missions. The calculations are presented with and without the lung adjustment to cancer rates. The values in parentheses represent the REIC and REID values without the adjustment.

Table 13 illustrates the sensitivity of REID (%) values for males and females across three mission scenarios under solar minimum conditions. Two models for excess risk rate, the mixture model (EAR and ERR model) and only the ERR model, as suggested by Cucinotta et al. [210], were employed for comparison.

**Table 12.** REIC (%) and REID (%) calculations for different mission scenarios and solar minimum conditions, for males and females at two exposure ages (30, 40 years old). The values in parenthesis refer to REIC and REID calculations without considering the lung adjustment in cancer incidence rates.

| **Missions (Solar Minimum)** | Males-REIC (%) | | Females-REIC (%) | | Males-REID (%) | | Females-REID (%) | |
|---|---|---|---|---|---|---|---|---|
| **Age at exposure** | **30** | **40** | **30** | **40** | **30** | **40** | **30** | **40** |
| Mars (940 d) | 8.86 (9.45) | 6.84 (7.89) | 14.42 (17.45) | 10.62 (13.52) | 3.07 (3.42) | 2.37 (2.99) | 4.43 (6.05) | 3.33 (5.18) |
| Mars (600 d) | 5.89 (6.37) | 4.53 (5.25) | 9.70 (11.82) | 7.10 (9.12) | 2.02 (2.30) | 1.55 (2.00) | 2.95 (4.08) | 2.20 (3.48) |
| Lunar (90 d) | 0.60 (0.66) | 0.46 (0.54) | 1.00 (1.24) | 0.73 (0.94) | 0.20 (0.24) | 0.15 (0.21) | 0.30 (0.42) | 0.22 (0.36) |

**Table 13.** REID (%) calculations for different mission scenarios in solar minimum conditions, using the mixture excess risk model (ERR and EAR) and only the ERR model for the cancer incidence rates. REID was calculated for males and females of 30 and 40 years old at first exposure.

| **Missions (Solar Minimum)** | Males-REID (%) EAR+ERR model | | Females-REID (%) EAR+ERR model | | Males-REID (%) Only ERR model | | Females-REID (%) Only ERR model | |
|---|---|---|---|---|---|---|---|---|
| **Age at exposure** | **30** | **40** | **30** | **40** | **30** | **40** | **30** | **40** |
| Mars (940 d) | 3.07 | 2.37 | 4.43 | 3.33 | 2.55 | 2.16 | 3.92 | 3.16 |
| Mars (600 d) | 2.02 | 1.55 | 2.95 | 2.20 | 1.72 | 1.45 | 2.65 | 2.13 |
| Lunar (90 d) | 0.20 | 0.15 | 0.30 | 0.22 | 0.18 | 0.15 | 0.28 | 0.22 |

Table 14 displays the Q values and average mission equivalent doses, for both solar minimum and maximum conditions across three space mission scenarios. The Q values are derived from microdosimetric TDRA Q and the NASA approach (retrieved from OLTARIS). These Q values are subsequently incorporated into Eq. (69) for the calculation of REID percentages during three space mission scenarios under solar minimum conditions. The analysis involves considerations for both sexes and two different ages at exposure (30, 40). The resulting REID (%) values are presented in Table 15.

**Table 14.** Q values and average mission equivalent doses for different mission scenarios at solar minimum conditions, using 20 g/cm$^2$ aluminium shielding for two distinct Q approaches: The microdosimetric TDRA (this work) and NASA model obtained from OLTARIS platform.

| Missions (Solar Minimum) | Q-microdosimetric (TDRA: This Work) | | Q-NASA (OLTARIS) | | Dose Equivalent (mSv) $(= D \times \overline{Q_{\mathrm{TDRA}}})$ | | Dose Equivalent (mSv) $(= D \times \overline{Q_{\mathrm{NASA}}})$ | |
|---|---|---|---|---|---|---|---|---|
| | Solar Min | Solar Max | Solar Min | Solar Max | Solar Min | Solar Max | Solar Min | Solar Max |
| Mars (940 d) | 2.66 | 2.81 | 2.34 | 2.35 | 885 | 573 | 779 | 479 |
| Mars (600 d) | 2.59 | 2.75 | 2.30 | 2.31 | 769 | 481 | 683 | 367 |
| Lunar (90 d) | 2.95 | 3.30 | 2.69 | 2.71 | 68 | 52 | 62 | 43 |

**Table 15.** REID (%) calculations using the microdosimetric TDRA Q and NASA's Q values for each space mission scenario, for solar minimum conditions, both sexes (males, females) and two ages at exposure (30, 40).

| Missions (Solar Minimum) | REID (%) TDRA | | | | REID (%) NASA | | | |
|---|---|---|---|---|---|---|---|---|
| | Males | | Females | | Males | | Females | |
| | 30 | 40 | 30 | 40 | 30 | 40 | 30 | 40 |
| Mars (940 d) | 3.07 | 2.37 | 4.43 | 3.33 | 2.72 | 2.1 | 3.93 | 2.95 |
| Mars (600 d) | 2.02 | 1.55 | 2.95 | 2.20 | 1.80 | 1.39 | 2.64 | 1.97 |
| Lunar (90 d) | 0.20 | 0.15 | 0.30 | 0.22 | 0.18 | 0.14 | 0.27 | 0.20 |

Table 16 displays the permissible mission duration for three space mission scenarios under both solar conditions. The upper limits considered are 600 mSv (NASA) and 1000 mSv (ESA). Tables 17 and 18 present the REID (%) values for males and females, respectively. These values are calculated for three different ages at exposure (30, 40, and 50) under both solar maximum and minimum conditions. Correspondingly, Tables 19 and 20 display the REIC (%) values for males and females, respectively.

**Table 16.** Safe days calculated with the microdosimetric quality factor of TDRA for two radiation exposure limits: NASA's and ESA's approach, for solar minimum and maximum conditions and three mission scenarios (Mars, Lunar space missions)

| Missions | Permissible Mission Duration (NASA: 600 mSv) | | Permissible Mission Duration (ESA: 1000 mSv) | |
|---|---|---|---|---|
| | **min** | **max** | **min** | **max** |
| Mars (940 d) | 605 | 938 | 1008 | 1564 |
| Mars (600 d) | 468 | 747 | 780 | 1246 |
| Lunar (90 d) | 556 | 797 | 927 | 1327 |

**Table 17.** Male REID (%) calculations using the microdosimetric TDRA Q values for each space mission scenario, for solar maximum and minimum conditions and three ages at initial exposure (30, 40, 50)

| REID (%)- Males | | | | | | |
|---|---|---|---|---|---|---|
| **Age at exposure** | **30** | | **40** | | **50** | |
| **Missions** | **Solar Min.** | **Solar Max.** | **Solar Min.** | **Solar Max.** | **Solar Min.** | **Solar Max.** |
| Mars (940 d) | 3.07 | 1.5 | 2.37 | 1.15 | 1.88 | 0.91 |
| Mars (600 d) | 2.02 | 1.26 | 1.55 | 0.96 | 1.23 | 0.76 |
| Lunar (90 d) | 0.20 | 0.13 | 0.15 | 0.10 | 0.12 | 0.08 |

**Table 18.** Female REID (%) calculations using the microdosimetric Q values for each space mission scenario, for solar maximum and minimum and three ages at exposure (30, 40, 50)

| REID (%)- Females | | | | | | |
|---|---|---|---|---|---|---|
| **Age at exposure** | **30** | | **40** | | **50** | |
| **Missions** | **Solar Min.** | **Solar Max.** | **Solar Min.** | **Solar Max.** | **Solar Min.** | **Solar Max.** |

| | | | | | | |
|---|---|---|---|---|---|---|
| Mars (940 d) | 4.43 | 2.22 | 3.33 | 1.65 | 2.58 | 1.27 |
| Mars (600 d) | 2.95 | 1.75 | 2.20 | 1.31 | 1.70 | 1.00 |
| Lunar (90 d) | 0.30 | 0.20 | 0.22 | 0.15 | 0.17 | 0.11 |

**Table 19.** Male REIC (%) calculations using the microdosimetric Q values for each space mission scenario, for solar maximum and minimum and three ages at exposure (30, 40, 50)

| REIC (%)- Males | | | | | | |
|---|---|---|---|---|---|---|
| **Age at exposure** | **30** | | **40** | | **50** | |
| **Missions** | **Solar Min.** | **Solar Max.** | **Solar Min.** | **Solar Max.** | **Solar Min.** | **Solar Max.** |
| Mars (940 d) | 8.86 | 4.42 | 6.84 | 3.39 | 5.24 | 2.59 |
| Mars (600 d) | 5.89 | 3.71 | 4.53 | 2.84 | 3.46 | 2.17 |
| Lunar (90 d) | 0.60 | 0.40 | 0.46 | 0.30 | 0.35 | 0.23 |

**Table 20.** Female REIC (%) calculations using the microdosimetric Q values for each space mission scenario, for solar maximum and minimum and three ages (30, 40, 50)

| REIC (%)- Females | | | | | | |
|---|---|---|---|---|---|---|
| **Age at exposure** | **30** | | **40** | | **50** | |
| **Missions** | **Solar Min.** | **Solar Max.** | **Solar Min.** | **Solar Max.** | **Solar Min.** | **Solar Max.** |
| Mars (940 d) | 14.42 | 7.32 | 10.63 | 5.35 | 7.51 | 3.75 |
| Mars (600 d) | 9.70 | 6.16 | 7.10 | 4.49 | 4.99 | 7.10 |

| | | | | | | |
|---|---|---|---|---|---|---|
| Lunar (90 d) | 1.00 | 0.68 | 0.73 | 0.49 | 0.51 | 0.34 |

Finally, a comparative analysis was conducted between the REIC (%) and RADS (%) for males (Table 21) and females (Table 22). The assessment focused on a 30-year-old astronaut exposed to solar minimum conditions during the three distinct missions. The calculations were performed for three different attained ages: 60, 70, and 80 years old.

**Table 21.** RADS (%) and REIC (%) calculations for a 30-year-old (age at first exposure) and different attained ages (60, 70, 80) for three different missions' scenarios (Mars, Lunar missions) at solar minimum conditions using the microdosimetric quality factor

| **Males-Attained Age** | **60** | | **70** | | **80** | |
|---|---|---|---|---|---|---|
| **Missions (Solar Minimum)** | **RADS (%)** | **REIC (%)** | **RADS (%)** | **REIC (%)** | **RADS (%)** | **REIC (%)** |
| Mars (940 d) | 2.74 | 2.50 | 5.23 | 4.37 | 8.26 | 5.96 |
| Mars (600 d) | 2.40 | 2.19 | 4.59 | 3.83 | 7.26 | 5.22 |
| Lunar (90 d) | 0.24 | 0.21 | 0.46 | 0.38 | 0.73 | 0.52 |

**Table 22.** RADS (%) and REIC (%) calculations for a 30-year-old woman and different attained ages (60, 70, 80) for three different missions' scenarios (Mars, Lunar missions) in solar minimum using the microdosimetric quality factor

| **Females- Attained Age** | **60** | | **70** | | **80** | |
|---|---|---|---|---|---|---|
| **Missions (Solar Minimum)** | **RADS (%)** | **REIC (%)** | **RADS (%)** | **REIC (%)** | **RADS (%)** | **REIC (%)** |
| Mars (940 d) | 4.89 | 4.74 | 7.84 | 7.30 | 11.11 | 9.54 |
| Mars (600 d) | 4.3 | 4.16 | 6.90 | 6.40 | 9.80 | 8.37 |

| | | | | | | |
|---|---|---|---|---|---|---|
| Lunar (90 d) | 0.43 | 0.41 | 0.71 | 0.64 | 1.01 | 0.84 |

To translate the results into practical implications for astronauts and space agencies, Table 23 presents the findings on the years of life lost due to exposure to space radiation for astronauts. Calculations were made for three different space missions (Mars and Moon) under solar minimum conditions. The calculations consider both genders (males and females) and various ages at the time of initial radiation exposure (30, 40, 50 years).

**Table 23.** Years of Life Lost (YLL) for three mision scenarios at solar minimum conditions and three ages at exposure (30, 40, 50) for both sexes (males, females)

| Missions (Solar Minimum) | **Years of Life Lost (YLL)** | | | | | |
|---|---|---|---|---|---|---|
| | Males | | | Females | | |
| | **30** | **40** | **50** | **30** | **40** | **50** |
| Mars (940 d) | 6.7 | 4.1 | 2.4 | 9.2 | 5.4 | 3.1 |
| Mars (600 d) | 5.9 | 3.5 | 2.1 | 8.1 | 4.8 | 2.7 |
| Lunar (90 d) | 0.9 | 0.3 | 0.2 | 0.7 | 0.4 | 0.3 |

To explore the impact of age, DDREF, Q, and solar conditions on the sensitivity of risk metrics across the three missions, we present the trends derived from our calculations. Figures 27 and 28 showcase the REIC (%) and REID (%) values, respectively, as functions of age at exposure. These trends are presented for both solar maximum and minimum conditions, covering both sexes and the Mars and Moon mission scenarios.

In Figure 29, we illustrate the RADS (%) and REIC (%) values as functions of age at exposure, considering an attained age of 70 years old. This figure accounts for both sexes (males, females) under solar minimum conditions for all three mission scenarios. Figure 30 extends the analysis to depict the same metrics as functions of attained age, considering an astronaut of 30 years old at first exposure. The presentation refers both sexes and solar minimum conditions for the three space mission scenarios.

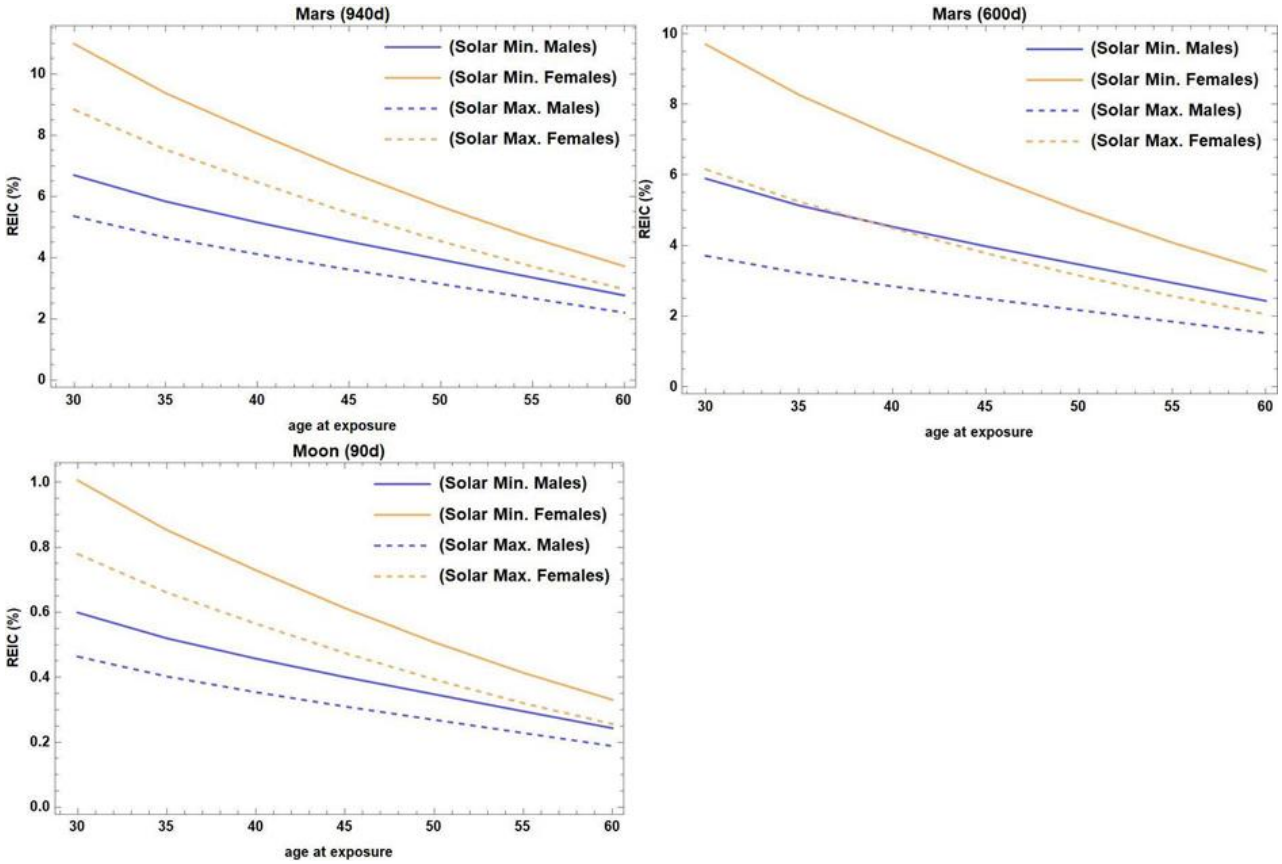


**Figure 27.** REIC (%) calculations as a function of age at exposure for different mission scenarios (Mars long and short stay and Lunar mission) in solar minimum and maximum conditions, for males and females.

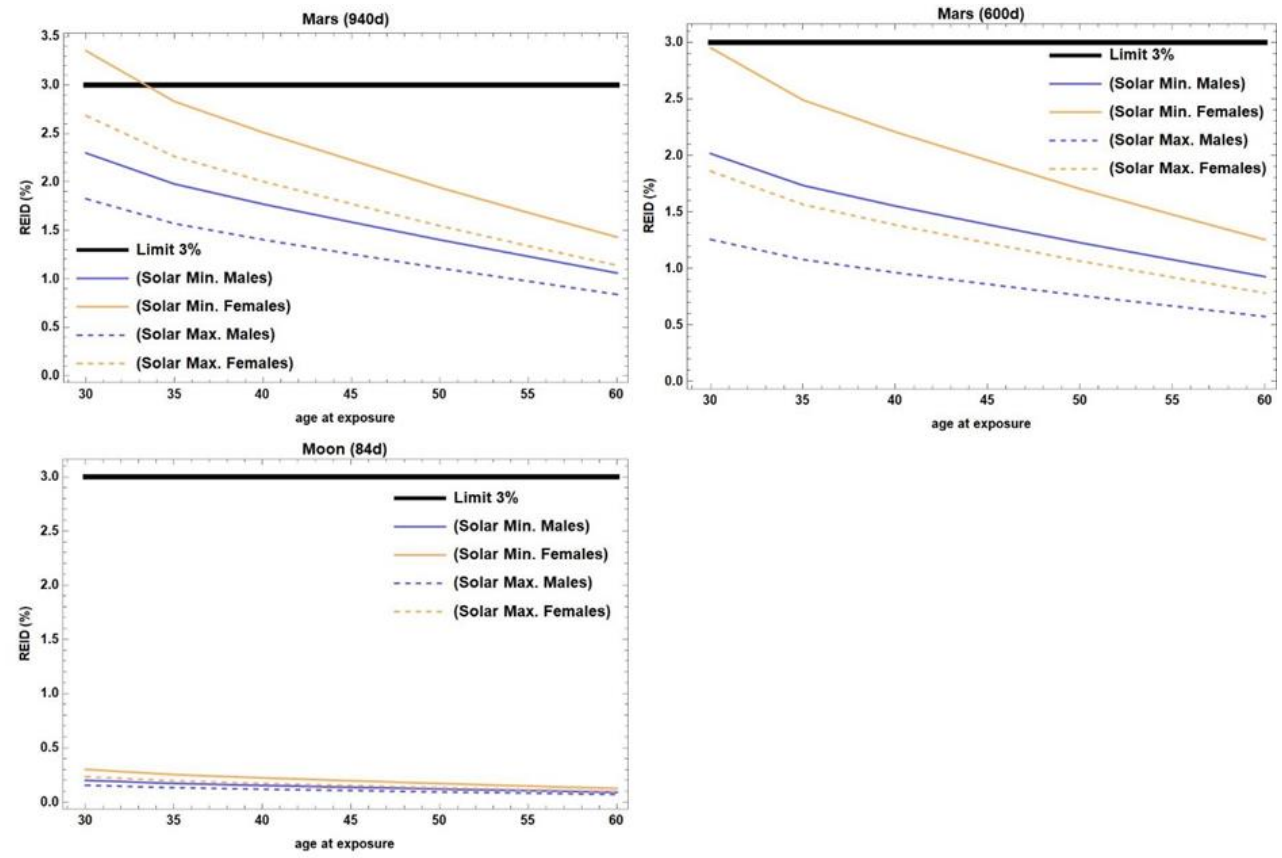

**Figure 28.** REID (%) calculations as a function of age at exposure for different mission scenarios (Mars long and short stay and Lunar mission) in solar minimum and maximum conditions, for males and females.

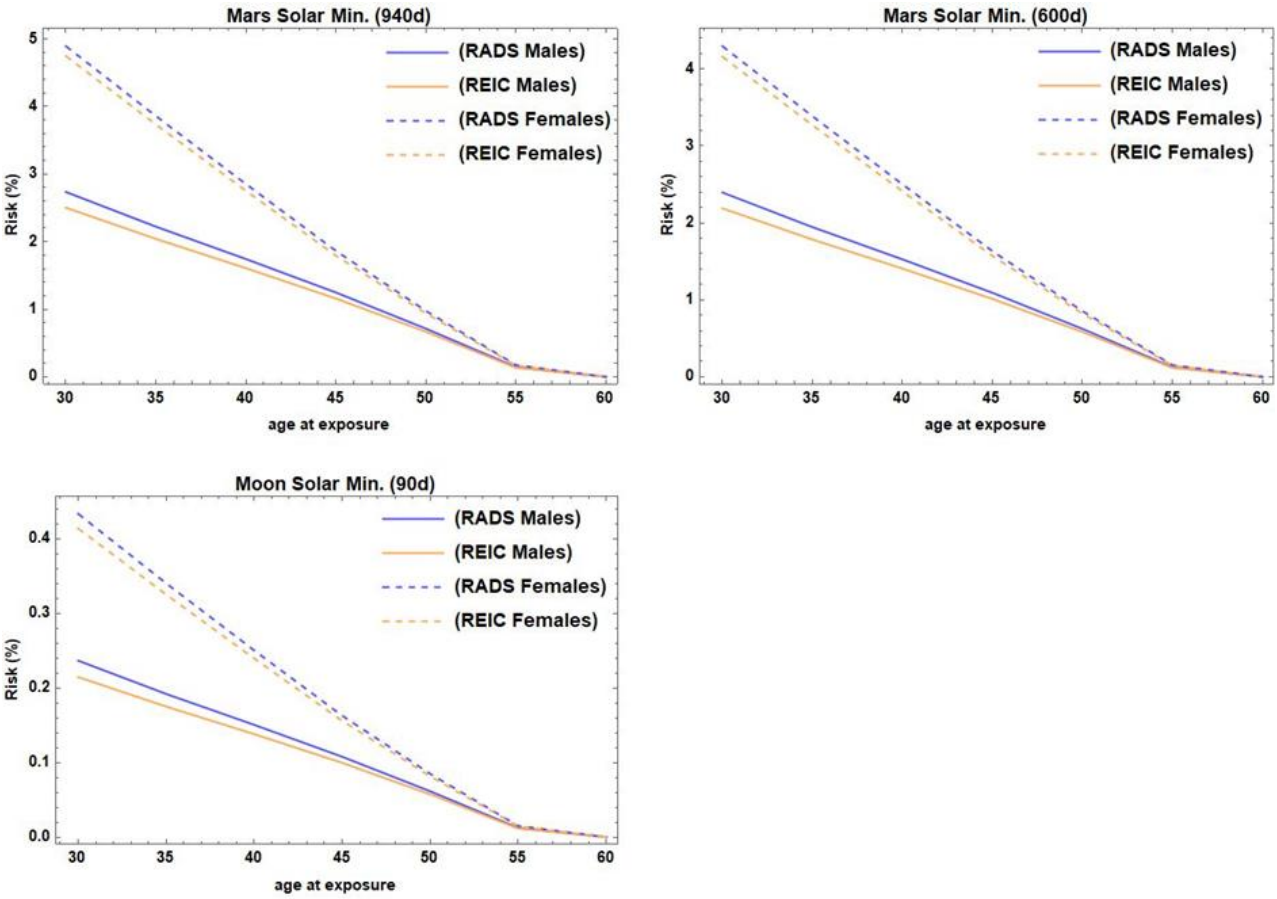


**Figure 29.** REIC (%) and RADS (%) calculations as a function of age at exposure for different mission scenarios (Mars long and short stay and Lunar mission) in solar minimum conditions, for males and females. The results were calculated for a 70-year-old male or female at attained age.

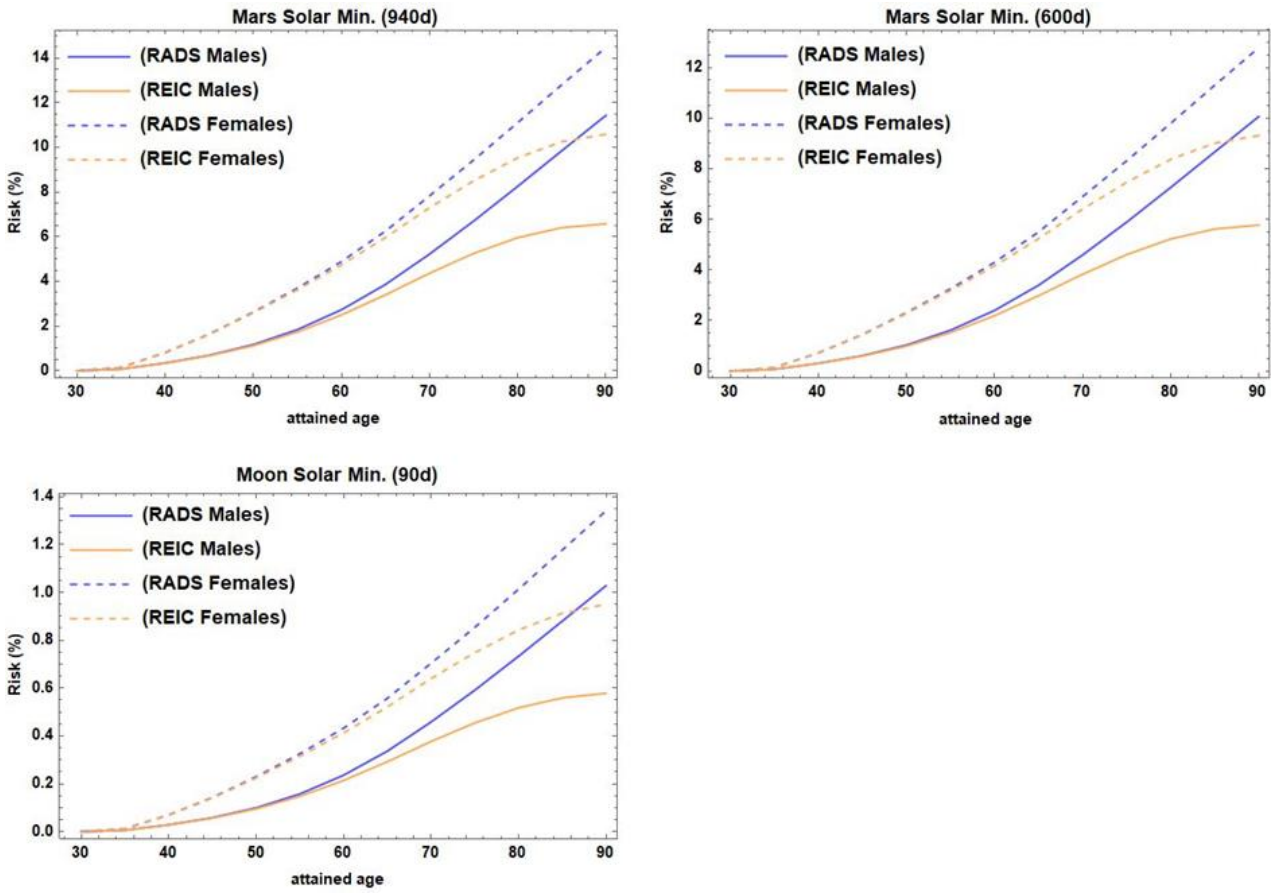


**Figure 30.** REIC (%) and RADS (%) calculations as a function of attained age for a 30-year-old male or female at first exposure, for different mission scenarios (Mars long and short stay and Lunar mission) in solar minimum conditions.

To examine the sensitivity of the REID (%) metric with Dose and Dose Rate Effectiveness Factor (DDREF) for various ages at first exposure, Figures 31, 32, and 33 are presented. These figures focus on the Mars swing-by, Mars long stay, and Lunar mission scenarios, respectively. The investigation involves both solar minimum and maximum conditions and encompasses both sexes (males, females) in the calculations.

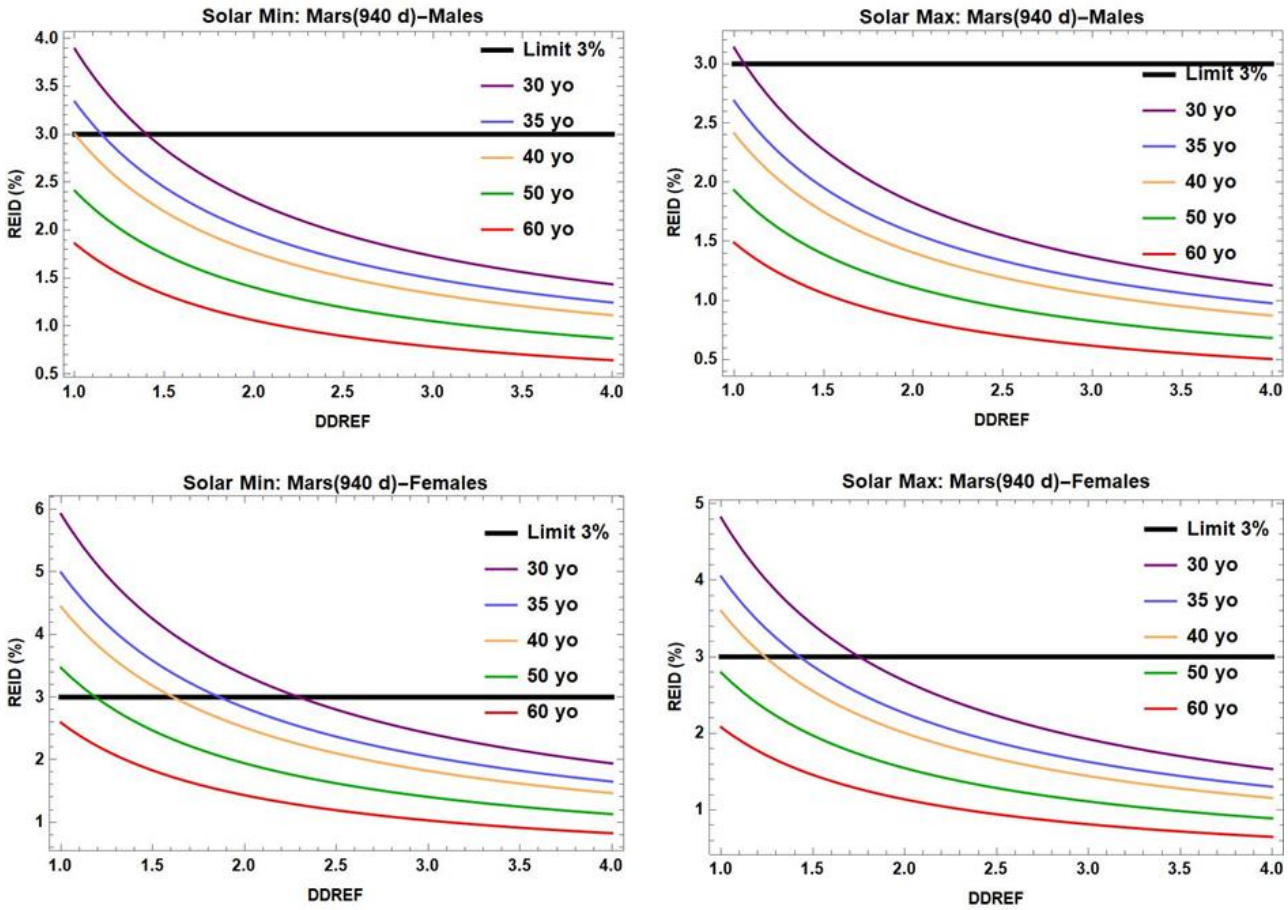


**Figure 31.** REID (%) calculations as a function of DDREF for Mars Long stay (940 days), in solar minimum and maximum conditions, for males and females at different ages at exposure.

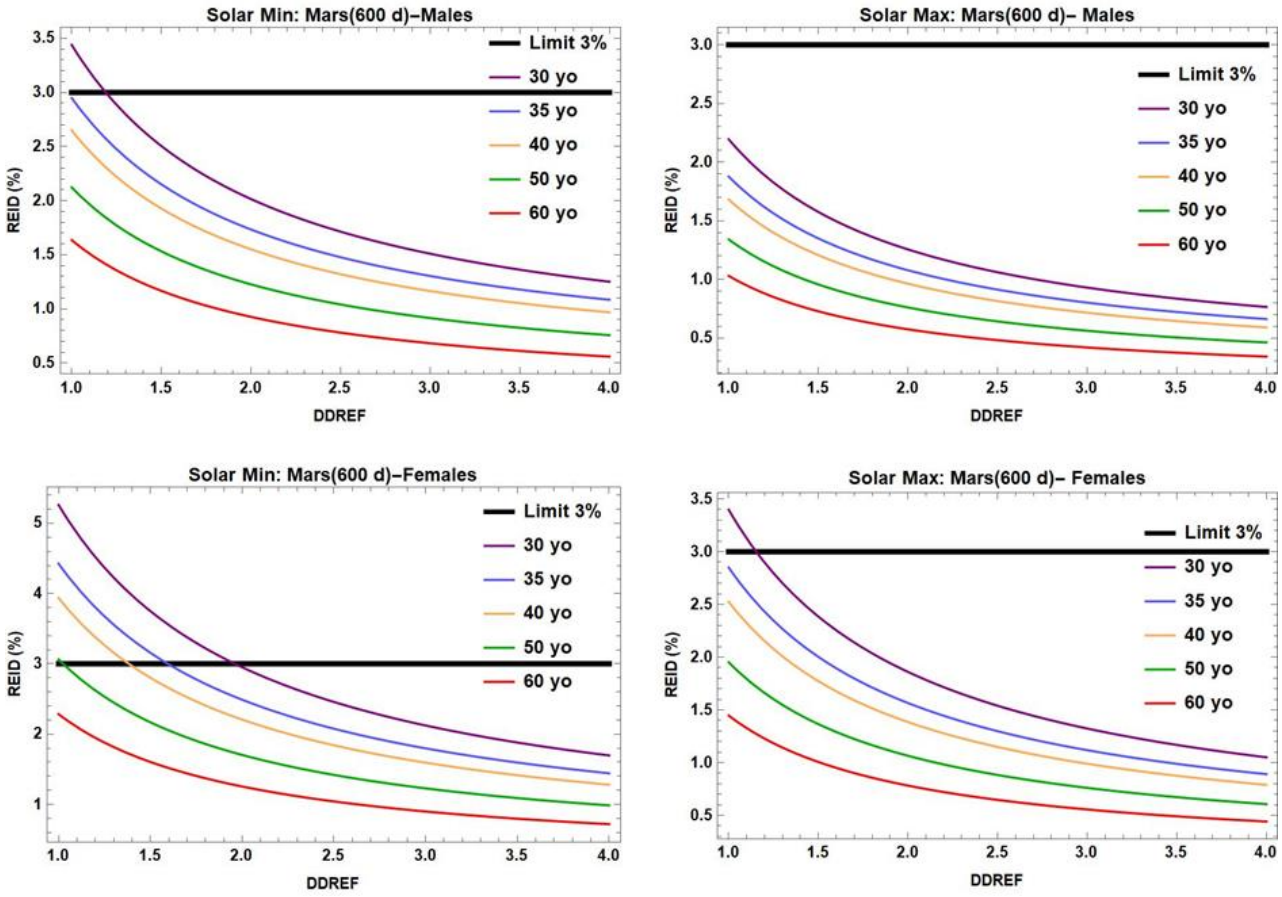


**Figure 32.** REID (%) calculations as a function of DDREF for a Mars short stay (600 days) mission, in solar minimum and maximum conditions, for males and females for different ages at exposure.

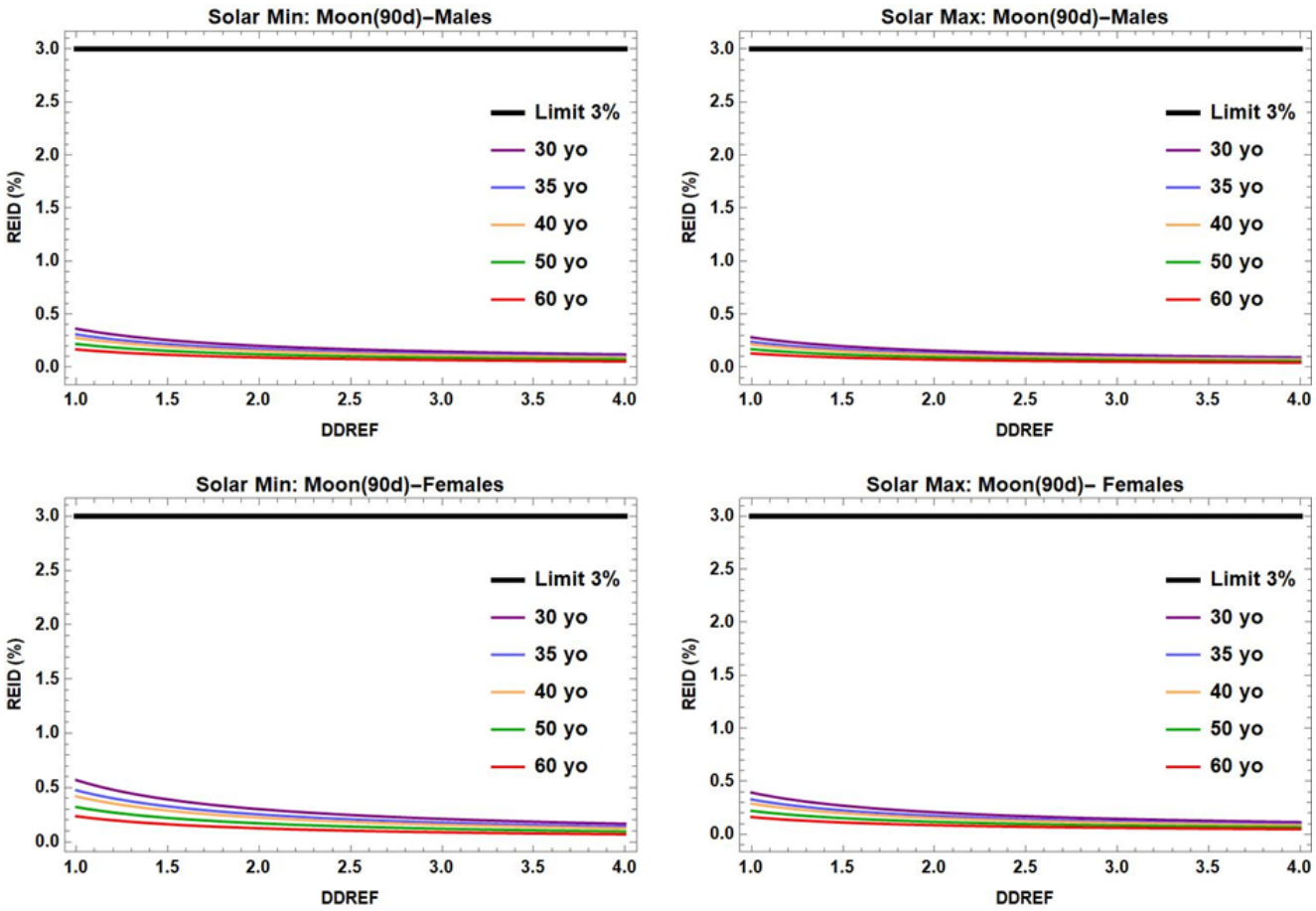


**Figure 33.** REID (%) calculations as a function of DDREF for a Lunar mission (90 days), in solar minimum and maximum conditions, for males and females for different ages at exposure.

The corresponding sensitivity of REID (%) with the microdosimetric Q is showed in Figures 34, 35 and 36 for Mars swing-by, long-stay and lunar mission respectively, at different ages at first exposure (30, 35, 40, 50, 60 years old). Both sexes and solar minimum and maximum conditions are accounted for calculations.

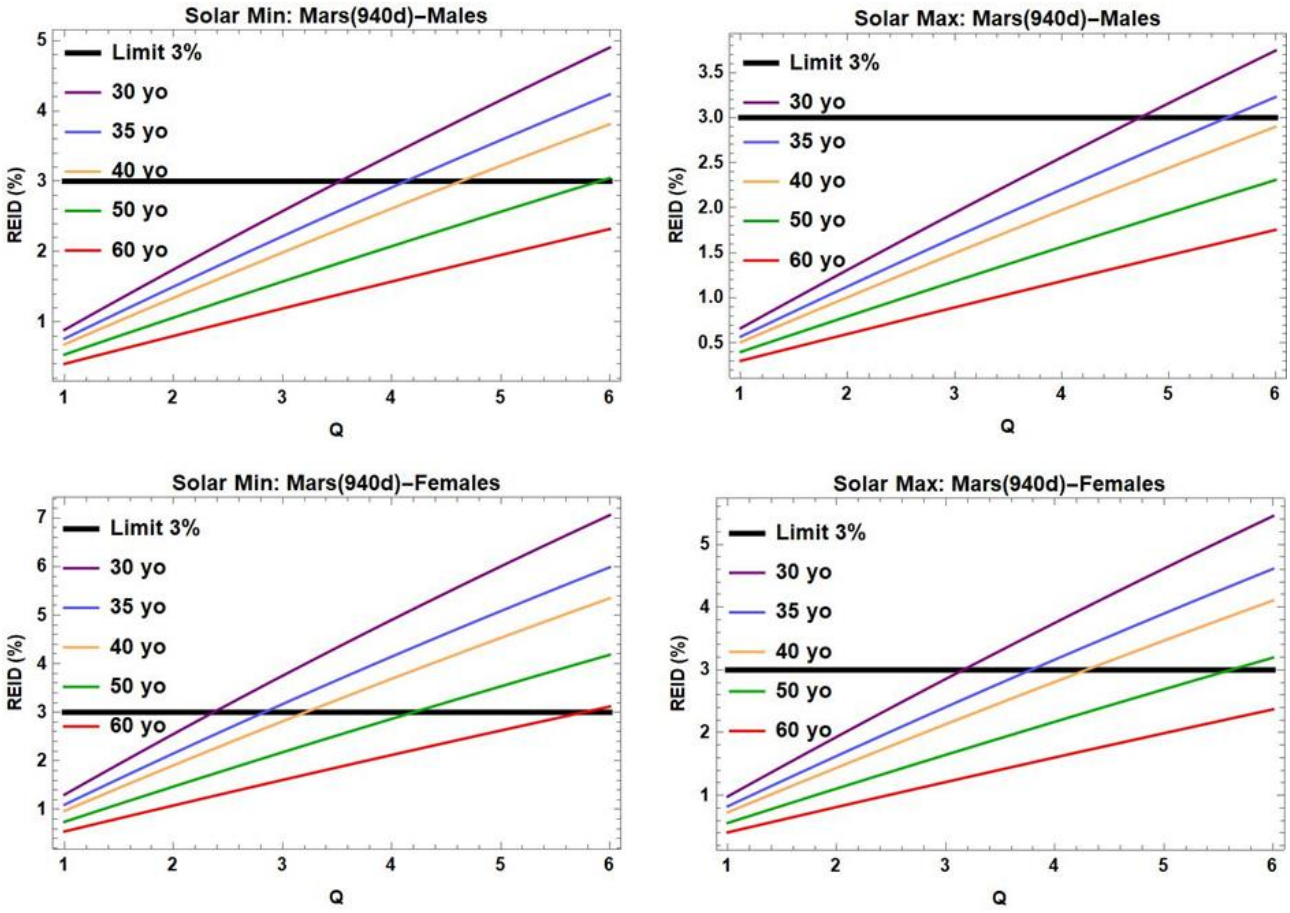


**Figure 34.** REID (%) calculations as a function of TDRA Q, for Mars Long stay (940 days), in solar minimum and maximum conditions, for males and females at different ages at exposure.

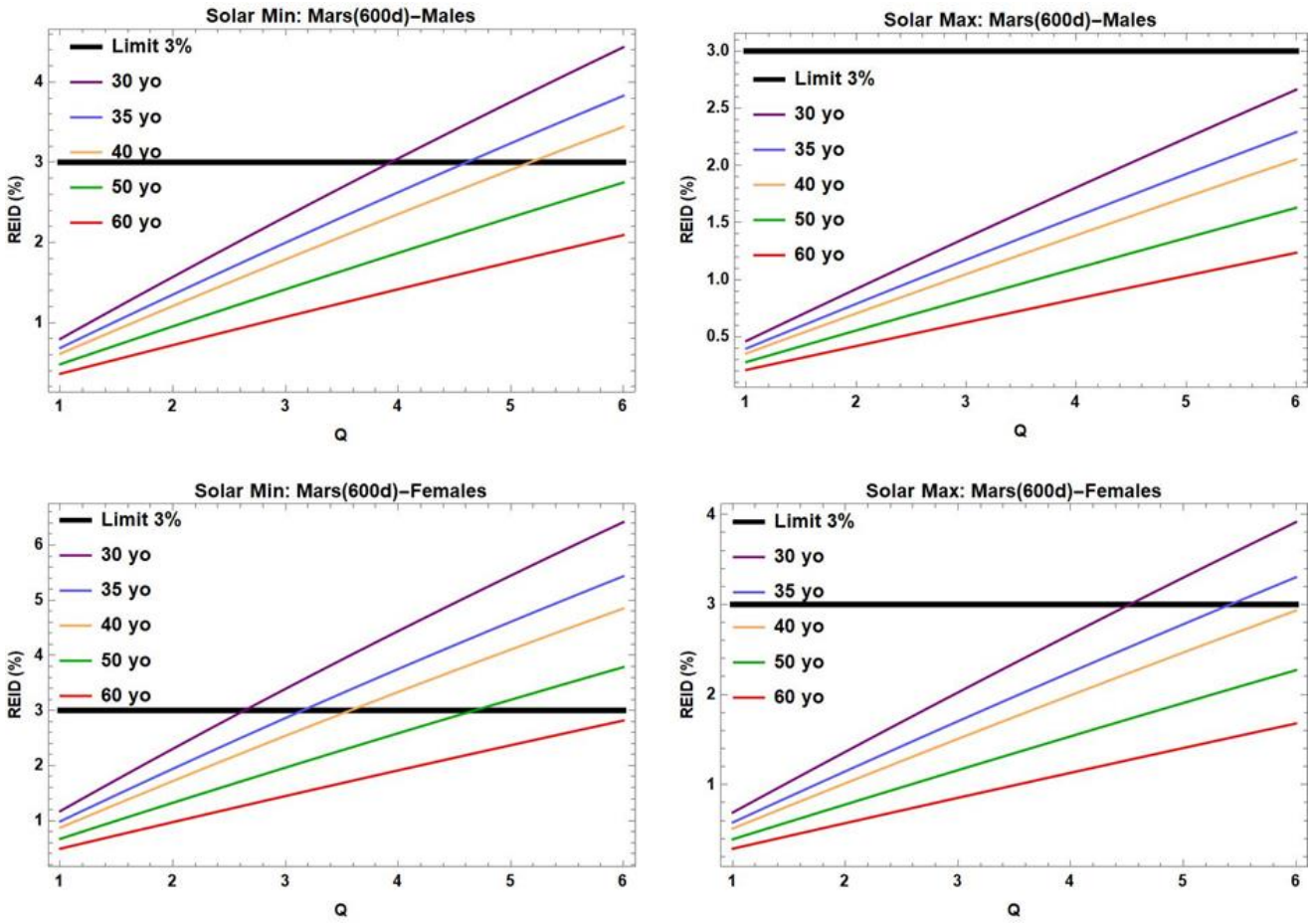


**Figure 35.** REID (%) calculations as a function of TDRA Q, for Mars short stay (600 days), in solar minimum and maximum conditions, for males and females at different ages at exposure.

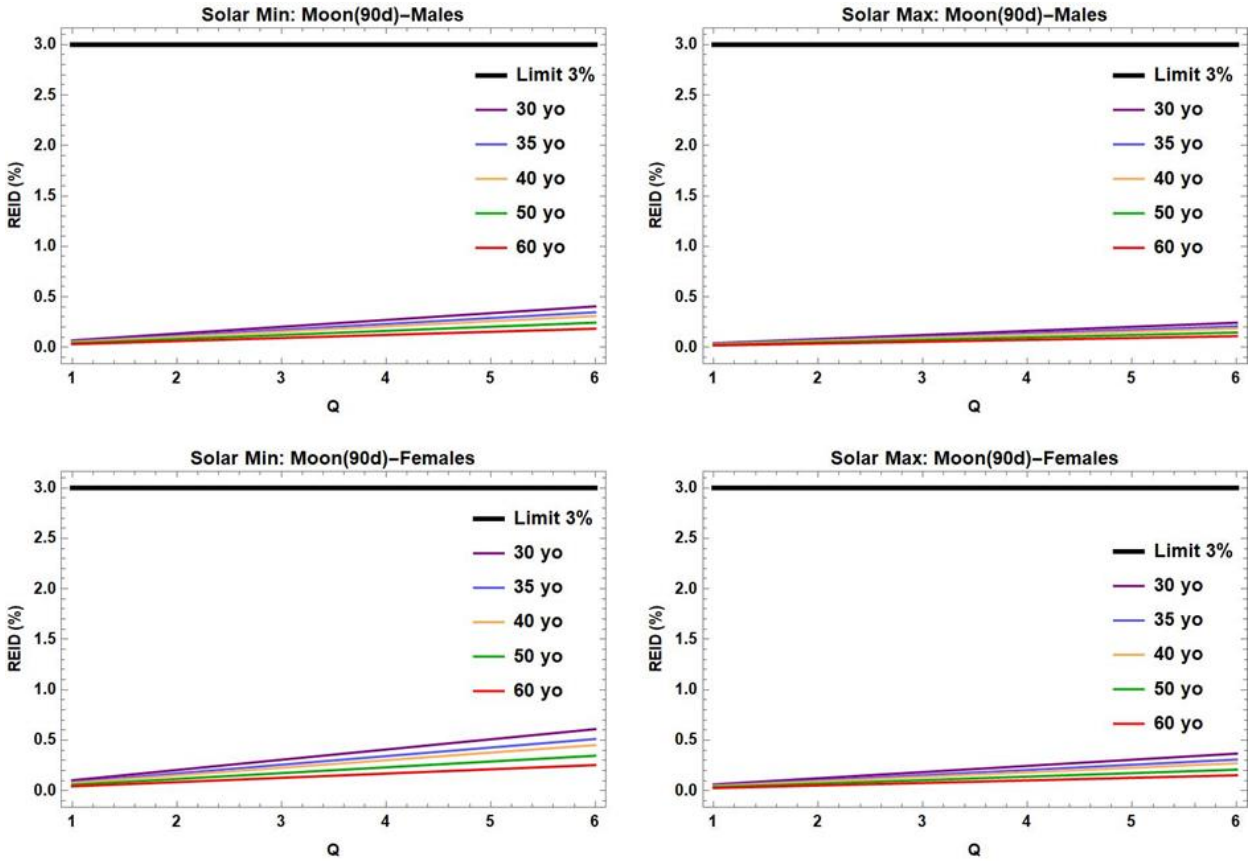


**Figure 36.** REID (%) calculations as a function of TDRA Q, for a Lunar mission (90 days), in solar minimum and maximum conditions, for males and females at different ages at exposure.

## Discussion

An analytical model was developed and employed for the calculation of dose-mean lineal energy ($y_D$) and the resulting values were subsequently exploited for the determination of a microdosimetric quality factor according to the TDRA methodology, and the REIC, REID and RADS metrics, for three space mission Mars and Lunar scenarios. The influence of the lung adjustment in the cancer incidence rates that were subsequently used for the REIC (%) and REID (%) calculations, is profound from Table 12. It tends to lower the REIC (%) and REID (%) values in contrast to no-lung adjustment. Specifically, for all three missions and males (30, 40 years old at first exposure) the relative difference (%) between the adjustment and no-adjustment is in between 7-18% for REIC (%) and in between 11-30% for REID (%) values. The lung adjustment is more significant for females where the relative difference is in between 11-27% for REIC (%) values and up to 60% for REID (%) values. These values mark the significance of a non-smoking astronaut profile and the need for cancer incidence rates in a non-smoking population.

The choice of a mixture model (EAR+ERR) or only ERR model seems to play no role for the Lunar mission (90 days) or yields a relative difference up to 20% to REID (%) values for men and women for the two Mars space missions, according to Table 13.

The choice of a microdosimetric quality factor according to the TDRA methodology or the NASA model yields a relative difference in male and female REID (%) values up to 13%. The relative difference between the microdosimetric quality factor in this work and the

corresponding Q values from NASA's model is up to 13% for the solar minimum conditions and the three space mission scenarios, whereas for the lunar mission and solar maximum conditions, the difference is up to 20%. Generally, in solar maximum conditions there is a shift to lower energy protons and the corresponding $y_D$ values obtained from our model have higher Q values. Overall, the differences between the two methods and methodologies seemed to be modest.

Generally, it is evident from the tables and graphs that the values of REIC (%) and REID (%) decrease as the age of first exposure to radiation increases, thereby reducing the years of exposure and consequently the probability of developing carcinogenesis. Additionally, during solar minimum, where the equivalent dose exceeds the solar maximum, it results in an increase in values for both genders and all three missions. Among males and females under the same solar conditions, age, and mission, females exhibit higher sensitivity. Maximum limits cannot be exceeded for a lunar mission lasting 90 days, regardless of solar conditions and gender, whereas they can be surpassed for a long-duration mission to Mars if calculations are made for a female aged 30-35 years. Generally, ages 30-40, according to the above calculations, are close to the upper limit, which could influence the astronaut's subsequent career in space missions. Attention must also be paid to cases where astronauts have been already in space and have been irradiated before.

Furthermore, these values for REIC (%) and REID (%) have been extracted for specific simulation and shielding conditions, which may change when the shielding is different and not uniform everywhere. Additionally, effective dose from solar particle events during the journey, with a higher likelihood during the declining phase of solar maximum, should be added to the results. Finally, the parameters with the greatest uncertainty and significance in the calculations of REIC and REID metrics are the quality factor (Q) and DDREF factor, as shown in the graphs. The selection of these values plays a crucial role in the outcome of REIC and REID. This means that upper limits can be exceeded or lie at the threshold at older ages beyond 35 years old.

A fundamental drawback of this work is that it considers only central values and does not perform statistical analysis with confidence intervals for the results. However, our main aim was to demonstrate that the application of microdosimetry with the theory of TDRA in the space radiation environment can yield significant results, as it employs physical quantities such as lineal energy, which are physically suited for studying energy deposition in cellular and subcellular targets, and that rapid and practical calculations can be made with acceptable uncertainty using an analytical model. This is evident in Table 14 and the differences between the quality factor of the TDRA and NASA, as well as in Table 15 with the values of REID (%). The selection of a microdosimetric quality factor can be applied to any metric (either REIC/REID or RADS) and offers a practical solution since it can be measured by detectors for the spectrum of particles.

According to the graphs, the values of REIC (%) and RADS (%) (incidence) exhibit similar values when calculations are made for a male or female up to the age of 60-65 years, as the upper calculation limit of RADS (%) does not consider competing risks. The choice of RADS might be easier and more practical in that it can be communicated more easily to astronauts as the relative decrease in their survival until a certain age, as demographic data, which can introduce greater uncertainties, are not needed.

Overall, there are many uncertainties in various parts of the risk metric calculations, with the primary uncertainty being the quality factor (Q) and DDREF. The selection of an analytical model for calculating microdosimetric quantities and the framework of the dual theory can be robust for calculating cancer risk for astronauts.

## Conclusions

The uncertainty in the quality factor (Q) for radiation-induced carcinogenesis due to Galactic Cosmic Rays (GCR) is the greatest challenge for calculating the cancer risk for astronauts on long-term space missions in deep space, on the Moon, and Mars. We have presented a semi-analytical microdosimetric model that calculates dose-weighted lineal energy ($y_D$) for all space ions (from protons to iron), over an energy range of 1 MeV to 1 GeV, and for spherical liquid water targets ranging from 10 nm to 1000 nm. These dimensions represent critical subcellular and cellular targets (DNA segments, chromatin, chromosomes) of interest for space radiation protection and ion beam radiotherapy. The model includes energy-loss straggling, the range of secondary electrons within the target, and two types of interactions: direct and indirect events. In the latter (indirect events), Monte Carlo simulations with Geant4-DNA were used to calculate the $y_D$ of secondary electrons. The results of the semi-analytical model were benchmarked against the most validated Monte Carlo codes (Geant4-DNA, PHITS, RITRACKS, MCDS) and showed very good agreement, thus supporting its use. Subsequently, the $y_D$ values were used to calculate the microdosimetric quality factor Q using the theory of dual radiation action (TDRA) and were applied to space missions within the Earth's magnetosphere and in deep space. The results for the microdosimetric quality factor showed excellent agreement with the NASA model and very small differences compared to the Q factor from the ICRP Report 60 recommendations, which is calculated using LET, as well as with experimental Q measurements in low Earth orbit on the International Space Station, space shuttles, and with MSL RAD in deep space. Additionally, the semi-analytical calculations of Q were used to calculate various metrics such as REIC, REID, RADS for typical aluminium shielding, different solar conditions, space missions, and various ages and both genders.

This model is recommended for the calculation of the quality factor (Q) in space missions, as it is based on the physical appropriate radiation-matter interaction quantity, lineal energy (y), and offers practicality and ease of calculation, in contrast to the more time-consuming Monte Carlo codes. This effort to develop the microdosimetric model and calculate Q via TDRA aims to facilitate the computation of the quality factor and reduce uncertainty in its calculation through microdosimetry, with the ultimate goal of establishing safe radiation-induced limits for astronauts, who will spend considerable time in space in the coming years.

## Abstract

**Background:** Space radiation poses the foremost health risk for astronauts, with the potential for carcinogenesis from Galactic Cosmic Rays (GCR) being the main constraint for long-duration missions beyond low Earth orbit (BLEO). Estimating the cancer risk is challenging due to limited astronaut epidemiological data. The reference radiation studies stem from the atomic bomb survivors (LSS), which aren't ideal reference population, as they involved high dose rates and low-LET radiation, while astronauts face mainly low dose rates and a broader LET spectrum in space.

Until recently, all missions have been in Low-Earth Orbit (LEO), so the differences in cancer risk assessment among space agencies did not pose issues for mission planning. However, for Beyond-LEO (BLEO) missions, where doses are higher and encounters with heavy ions are more frequent, uncertainties in estimating the cancer risk are notable. The greatest uncertainty in risk estimation is in calculating the quality factor (Q) of space radiation. Currently, there is no consensus among space agencies regarding the theoretical calculation of Q, while experimental data for the heavy ions from GCR is limited.

NASA diverged from the LET-based method (recommended by ICRP Report 60), which was previously used to calculate Q in LEO missions. Instead, NASA estimates Q as a function of the track-structure parameter $(Z/\beta)^2$. Meanwhile, other space agencies, such as ESA, JAXA and RSA continue to use the LET-based method. However, the LET approach has significant limitations in predicting the quality of space radiation. It simplifies the interaction of radiation with living matter and presents inaccuracies for the diverge space radiation. In addition, it is not a directly measurable quantity, as well as it predicts that ions with the same LET have the same biological effectiveness, which is incorrect due to variations in their different track structure.

**Purpose:** The study aims to apply the microdosimetric Q from the well-established Theory of Dual Radiation Action (TDRA) for space radiation and manned space missions, as well as established cancer risk metrics and safe days for astronauts. We developed a semi-analytic method for calculating the required microdosimetric quantity lineal energy (y), which is a better descriptor of radiation quality than LET and it is also measurable by TEPC (tissue-equivalent proportional counter) detectors, as used in space shuttle missions and the ISS.

**Methodology:** During the doctoral project, we have modified the US Naval Research Laboratory (NRL) microdosimetric model (developed by Xapsos and co-workers) for application to the space radiation environment, by extending its application to heavy ions (up to iron) and up to few GeV/u, extending its reliability to nanometer target sizes and combining direct (ion) and indirect (δ-ray) events using Geant4-DNA simulations and models. Our new microdosimetric model was benchmarked against proton Monte Carlo track-structure simulation data from PHITS, RITRACKs and Geant4-DNA for target-spheres from 10-1000 nm.

**Results:** Our microdosimetric calculations were in very good agreement (within 10%) with the MCTS data for all spheres. The extended-NRL model was used to calculate TDRA-based average quality factors (Q) for the GCR spectrum in two simple mission scenarios, i.e., at ISS and at 1 AU in deep space. Our quality factor predictions were in excellent agreement (within 1-3%) with the latest NASA model. Our quality factor predictions were in excellent agreement

(within experimental uncertainties) with TEPC measurements at ISS and at the MSL RAD (deep space). Additionally, the values of the quality factor (Q) were used to calculate radiation-induced cancer risk for space mission scenarios to the Moon and Mars. The cancer risk assessments indicated that, for a mission to Mars, women under the age of 35–40 are the most radiosensitive group and therefore exceed or are at risk of exceeding the maximum radiation dose limits set by the space agencies of ESA and NASA, respectively. In contrast, missions to the Moon remain within dose limits, provided they last less than approximately 2 years.

**Conclusions:** The proposed semi-analytic microdosimetric model with TDRA quality factor estimations, is expected to be both practical and reliable for the assessment of cancer risk for astronauts in deep space missions, where no space agency has yet established specific radiation risk limits.

# Περίληψη

**Υπόβαθρο:** Η διαστημική ακτινοβολία αποτελεί τον κυριότερο παράγοντα κινδύνου για την υγεία των αστροναυτών, με την πιθανότητα καρκινογένεσης από τις Γαλαξιακές Κοσμικές Ακτίνες (GCR) να αποτελεί το μεγαλύτερο τροχοπέδι για τις μελλοντικές μακροχρόνιες διαστημικές αποστολές πέρα από το μαγνητικό πεδίο της Γης (BLEO). Η εκτίμηση του ακτινοπροκλητού ρίσκου καρκινογένεσης είναι ιδιαίτερα δύσκολη, καθώς τα επιδημιολογικά δεδομένα των αστροναυτών είναι πολύ περιορισμένα. Οι βασικές επιδημιολογικές μελέτες προέρχονται από τους επιζώντες της ατομικής βόμβας (LSS), οι οποίοι όμως δεν αποτελούν ιδανικό πληθυσμό αναφοράς, αφού η έκθεσή τους προέρχεται κυρίως από υψηλούς ρυθμούς δόσεις και ακτινοβολία χαμηλού LET, ενώ στο διάστημα οι αστροναύτες εκτίθενται κυρίως σε χαμηλούς ρυθμούς δόσεις και σε όλο το φάσμα του LET. Μέχρι πρόσφατα, όλες οι διαστημικές αποστολές εκτελούνταν σε χαμηλή τροχιά κοντά στη Γη (LEO), με αποτέλεσμα οι διαφορές στις προβλέψεις του ακτινικού ρίσκου καρκινογένεσης μεταξύ των διαστημικών οργανισμών να μην επηρεάζουν τον σχεδιασμό των αποστολών. Ωστόσο, στις αποστολές Beyond-LEO (π.χ. Σελήνη, Άρης), όπου οι δόσεις είναι μεγαλύτερες και οι αλληλεπιδράσεις με βαριά ιόντα των GCR γίνονται συχνότερες, οι αβεβαιότητες στην εκτίμηση της ακτινοπροκλιτής καρκινογένεσης παίζουν κυρίαρχο ρόλο. Η σημαντικότερη αβεβαιότητα αφορά τον υπολογισμό του παράγοντα ποιότητας (Q) της διαστημικής ακτινοβολίας. Προς το παρόν δεν υπάρχει συμφωνία μεταξύ των διαστημικών οργανισμών όσον αφορά τη θεωρητική προσέγγιση του Q, ενώ τα πειραματικά δεδομένα για τα βαριά ιόντα των GCR είναι περιορισμένα. Η NASA αποκλίνει από τη μέθοδο που χρησιμοποιείται για ακτινοπροστασία στη Γη και στον Διεθνή Διαστημικό Σταθμό, η οποία θεωρεί το Q ως συνάρτηση του LET (όπως προτείνεται από τις συστάσεις της ICRP), και υπολογίζει πλέον το Q ως συνάρτηση της παραμέτρου δομής-τροχιάς $Z/\beta^2$. Αντίθετα, άλλοι οργανισμοί, όπως η ESA, η JAXA και η RSA, συνεχίζουν να υπολογίζουν το Q με βάσει το LET της ακτινοβολίας. Ωστόσο, η μέθοδος αυτη παρουσιάζει σημαντικούς περιορισμούς: απλοποιεί υπέρμετρα την αλληλεπίδραση της ακτινοβολίας με τη βιολογική ύλη, δεν αποτελεί άμεσα μετρήσιμη ποσότητα από τους ανιχνευτές στο διάστημα και τέλος, υποθέτει λανθασμενα ότι τα ιόντα με ίδιο LET έχουν και την ίδια βιολογική αποτελεσματικότητα.

**Σκοπός:** Η παρούσα μελέτη αποσκοπεί στον υπολογισμό και την εφαρμογή του παράγοντα ποιότητας (Q) της διαστημικής ακτινοβολίας σύμφωνα με τη μικροδοσιμετρική θεωρία της διπλής ακτινικής δράσης (TDRA). Οι υπολογισμοί του παράγοντα Q θα εφαρμοστούν για διάφορα σενάρια επανδρωμένων αποστολών και θα χρησιμοποιηθούν για τον υπολογισμό του ακτινοπροκλητού ρίσκου καρκινογένεσης και των ασφαλών ημερών στο διάστημα για τους αστροναύτες. Για τους παραπάνω λόγους, αναπτύχθηκε μια ημι-αναλυτική μέθοδος υπολογισμού της μικροδοσιμετρικής γραμμικής ενέργειας (y), η οποία περιγράφει με μεγαλύτερη ακρίβεια την ποιότητα της ακτινοβολίας και τον παράγοντα Q σε σχέση με το LET, ενώ δύναται να μετρηθεί με ανιχνευτές θαλάμων ιονισμού (TEPC), όπως αυτοί που χρησιμοποιήθηκαν σε αποστολές του διαστημικού λεωφορείου και στον ΔΔΣ.

**Μεθοδολογία:** Κατά τη διάρκεια του διδακτορικού έργου, τροποποιήσαμε το μικροδοσιμετρικό μοντέλο του US Naval Research Laboratory (NRL) που αναπτύχθηκε από τους Xapsos και συνεργάτες για το διαστημικό περιβάλλον, επεκτείνοντας την εφαρμογή του σε βαριά ιόντα (έως σίδηρο) και σε ενέργειες έως μερικά GeV/u. Η αξιοπιστία του μοντέλου εξετάστηκε σε μικρομετρικές και νανομετρικές διαστάσεις σφαιρικών στόχων για το μικροδοσιμετρικό μέγεθος της γραμμιώδους ενέργειας (y) και της σταθμισμένης ως προς τη δόση γραμμιώδους ενέργειας ($y_D$), συνδυάζοντας τα άμεσα (ιόντα) και έμμεσα (δ-ηλεκτρόνια)

γεγονότα μέσω των προσομοιώσεων του λογισμικού Geant4-DNA. Στη συνέχεια, το νέο μοντέλο συγκρίθηκε με υπολογισμούς για το μέγεθος y από κώδικες Monte Carlo δομής-τροχιάς (MCTS) για τα πρωτόνια, σε σφαιρικούς στόχους διαμέτρου 10-1000nm και ενεργειακό εύρος 1MeV- 1GeV.

**Αποτελέσματα:** Οι υπολογισμοί της σταθμισμένης ως προς τη δόση γραμμιώδους ενέργειας ($y_D$) που πραγματοποιήθηκαν με το νέο τροποποιημένο μικροδοσιμετρικό μοντέλο παρουσιάζουν πολύ καλή συμφωνία (εντός 10 %) με τα δεδομένα από τους κώδικες MCTS για όλες τις σφαίρες και όλο το ενεργειακό εύρος των πρωτονίων. Οι τιμές αυτές χρησιμοποιήθηκαν στη συνέχεια για να υπολογιστεί ο παράγοντας ποιότητας Q σύμφωνα με το TDRA για το φάσμα των GCR και για δύο σενάρια αποστολών, στον ΔΔΣ και στο βαθύ διάστημα σε απόσταση 1 αστρονομικής μονάδας (AU). Οι προβλέψεις μας για το Q συμφωνούν εξαιρετικά (εντός 1–3 %) με το πιο πρόσφατο μοντέλο της NASA και βρίσκονται εντός των πειραματικών αβεβαιοτήτων, με τις μετρήσεις που πραγματοποιήθηκαν με ανιχνευτές TEPC στον ISS και το RAD του MSL στο βαθύ διάστημα. Επίσης, οι τιμές του Q χρησιμοποιήθηκαν για τον υπολογισμό του ακτινικού καρκινικού ρίσκου για σενάρια διαστημικών αποστολών στη Σελήνη και τον Άρη. Οι υπολογισμοί του ρίσκου καρκινογένεσης έδειξαν ότι, για ένα ταξίδι στον Άρη, οι γυναίκες ηλικίας κάτω των ~35-40 ετών είναι η πιο ακτινοευαίσθητη ομάδα και συνεπώς ξεπερνάνε ή κινδυνεύουν να ξεπεράσουν τα ανώτατα όρια που έχουν τεθεί από τους διαστημικούς οργανισμούς της ΕΣΑ και ΝΑΣΑ αντίστοιχα. Αντίθετα, οι αποστολές στη Σελήνη βρίσκονται εντός ορίων δόσεων, εφόσον αυτές διαρκούν λιγότερο από ~2 χρόνια.

**Συμπεράσματα:** Το προτεινόμενο ημι-αναλυτικό μικροδοσιμετρικό μοντέλο για τον υπολογισμό του $y_D$ και του Q με βάση το TDRA για τη διαστημική ακτινοβολία, αναμένεται να είναι πρακτικό και αξιόπιστο για την πρόβλεψη του ρίσκου καρκινογένεσης των αστροναυτών σε αποστολές στο βαθύ διάστημα, όπου καμία διαστημική υπηρεσία δεν έχει ακόμη θεσπίσει όρια ακτινικών δόσεων.

## References

1. Vassiliev ON, Peterson CB, Cao W, Grosshans DR, Mohan R. Systematic microdosimetric data for protons of therapeutic energies calculated with Geant4-DNA. Phys Med Biol. 2019 Nov 4;64(21):215018.

2. National Council on Radiation Protection and Measurements, editor. Information needed to make radiation protection recommendations for space missions beyond low-earth orbit. Bethesda, MD: National Council on Radiation Protection and Measurements; 2006. 427 p. (NCRP report).

3. National Council on Radiation Protection and Measurements, editor. Radiation protection guidance for activities in low-earth orbit: recommendations of the Nattional Council on Radiation Protection and Measurements. Bethesda, Md: National Council on Radiation Protection and Measurements; 2000. 210 p. (NCRP report).

4. Dietze G, Bartlett D, Cool D, Cucinotta F, Jia X, McAulay I, et al. Icrp publication 123: Assessment of radiation exposure of astronauts in space. Ann ICRP. 2013;42(4):1–339.

5. Hellweg CE, Berger T, Matthiä D, Baumstark-Khan C. Radiation in Space: Relevance and Risk for Human Missions [Internet]. Cham: Springer International Publishing; 2020 [cited 2022 Jan 27]. (SpringerBriefs in Space Life Sciences). Available from: http://link.springer.com/10.1007/978-3-030-46744-9

6. Mitchell A, Pimenta D, Gill J, Ahmad H, Bogle R. Cardiovascular effects of space radiation: implications for future human deep space exploration. Eur J Prev Cardiol. 2019 Nov;26(16):1707–14.

7. Cucinotta FA. RADIATION RISK ACCEPTABILITY AND LIMITATIONS. :13.

8. National Research Council. Radiation hazards to crews of interplanetary missions: biological issues and research strategies. 1997.

9. Pelton JN, Allahdadi F, editors. Handbook of Cosmic Hazards and Planetary Defense [Internet]. Cham: Springer International Publishing; 2015 [cited 2024 Jun 25]. Available from: https://link.springer.com/10.1007/978-3-319-03952-7

10. Reitz G. Characteristic of the radiation field in low earth orbit and in deep space. Z Für Med Phys. 2008 Dec;18(4):233–43.

11. Durante M. Space radiation protection: Destination Mars. Life Sci Space Res. 2014 Apr;1:2–9.

12. Xapsos M. A Brief History of Space Climatology: From the Big Bang to the Present. IEEE Trans Nucl Sci. 2019 Jan;66(1):17–37.

13. Reitz G, Hellweg CE. Space Radiation and Its Biological Effects. In: Bolton PR, Parodi K, Schreiber J, editors. Applications of Laser-Driven Particle Acceleration [Internet]. 1st ed. Boca Raton, FL : CRC Press, Taylor & Francis Group, [2018]: CRC Press; 2018 [cited 2022 Jan 27]. p. 217–36. Available from: https://www.taylorfrancis.com/books/9780429817106/chapters/10.1201/9780429445101-16

14. Durante M. Heavy ion radiobiology for hadrontherapy and space radiation protection. Radiother Oncol. 2004 Dec;73:S158–60.

15. Cucinotta F, Cacao E, Saganti P. NASA Space Cancer Risk (NSCR) Model 2020. 2020.

16. Cucinotta F, Kim MY, Chappell L. Space radiation cancer risk projections and uncertainties. NASA TP. 2011 Jan 1;2011–216155.

17. Council NR. Technical Evaluation of the NASA Model for Cancer Risk to Astronauts Due to Space Radiation [Internet]. 2012 [cited 2022 Nov 16]. Available from: https://nap.nationalacademies.org/catalog/13343/technical-evaluation-of-the-nasa-model-for-cancer-risk-to-astronauts-due-to-space-radiation

18. Walsh L, Schneider U, Fogtman A, Kausch C, McKenna-Lawlor S, Narici L, et al. Research plans in Europe for radiation health hazard assessment in exploratory space missions. Life Sci Space Res. 2019 May;21:73–82.

19. Shavers M, Semones E, Tomi L, Chen J, Straube U, Komiyama T, et al. Space agency-specific standards for crew dose and risk assessment of ionising radiation exposures for the International Space Station. Z Für Med Phys. 2024 Feb;34(1):14–30.

20. Anon. Microdosimetry ICRU report 36. 1983;

21. Lindborg L, Waker A. Microdosimetry: experimental methods and applications in radiation therapy and radiation protection. 2020.

22. Rossi HH, Zaider M. Microdosimetry and its applications. Berlin: Springer-Verlag Berlin; 2012.

23. Kellerer AM. Fundamentals of microdosimetry. In Universitätsbibliothek der Ludwig-Maximilians-Universität München; 1985 [cited 2022 Apr 27]. Available from: https://epub.ub.uni-muenchen.de/id/eprint/8822

24. International Commission on Radiological Protection. 1990 recommendations of the International Commission on Radiological Protection. 1. ed. Oxford: Pergamon Press; 1991. 201 p. (ICRP publication Radiation protection).

25. International Commission on Radiological Protection, editor. RBE for deterministic effects: a report of a task group of Committee 1 of the International Commission on Radiological Protection. Oxford Frankfurt a.M.: Pergamon Press; 1990. 57 p. (ICRP publication Radiation protection).

26. Lindborg L, Hultqvist M, Carlsson Tedgren Å, Nikjoo H. Lineal energy and radiation quality in radiation therapy: model calculations and comparison with experiment. Phys Med Biol. 2013 May 21;58(10):3089–105.

27. Lindborg L, Lillhök J, Kyriakou I, Emfietzoglou D. Dose-mean lineal energy values for electrons by different Monte Carlo codes: Consequences for estimates of radiation quality in photon beams. Med Phys. 2022 Feb;49(2):1286–96.

28. Nikjoo H, Emfietzoglou D, Liamsuwan T, Taleei R, Liljequist D, Uehara S. Radiation track, DNA damage and response—a review. Rep Prog Phys. 2016 Nov 1;79(11):116601.

29. Joint Task Group on Radiation Protection Quantities, International Commission on Radiological Protection, International Commission on Radiation Units and Measurements, editors. The quality factor in radiation protection: report of a joint task group of the ICRP and the ICRU to the ICRP and the ICRU. Bethesda, Md., U.S.A: International Commission on Radiation Units and Measurements; 1986. 32 p. (ICRU report).

30. International Commission on Radiation Units and Measurements, editor. Microdosimetry. Bethesda, Md., U.S.A: International Commission on Radiation Units and Measurements; 1983. 118 p. (ICRU report).

31. Hawkins RB. A microdosimetric-kinetic theory of the dependence of the RBE for cell death on LET. Med Phys. 1998 Jul;25(7):1157–70.

32. Carabe A, Moteabbed M, Depauw N, Schuemann J, Paganetti H. Range uncertainty in proton therapy due to variable biological effectiveness. Phys Med Biol. 2012 Mar 7;57(5):1159–72.

33. Paganetti H, Blakely E, Carabe-Fernandez A, Carlson DJ, Das IJ, Dong L, et al. Report of the AAPM TG-256 on the relative biological effectiveness of proton beams in radiation therapy. Med Phys. 2019 Mar;46(3):e53–78.

34. McNamara AL, Schuemann J, Paganetti H. A phenomenological relative biological effectiveness (RBE) model for proton therapy based on all published *in vitro* cell survival data. Phys Med Biol. 2015 Nov 7;60(21):8399–416.

35. Kellerer AM, Rossi HH. A Generalized Formulation of Dual Radiation Action. Radiat Res. 1978 Sep;75(3):471.

36. Kyriakou I, Tremi I, Georgakilas AG, Emfietzoglou D. Microdosimetric investigation of the radiation quality of low-medium energy electrons using Geant4-DNA. Appl Radiat Isot. 2021 Jun;172:109654.

37. Cucinotta FA, Cacao E, Alp M. Space Radiation Quality Factors and the Delta Ray Dose and Dose-Rate Reduction Effectiveness Factor. Health Phys. 2016 Mar;110(3):262–6.

38. Durante M, Cucinotta FA. Physical basis of radiation protection in space travel. Rev Mod Phys. 2011 Nov 8;83(4):1245–81.

39. Incerti S, Kyriakou I, Bernal MA, Bordage MC, Francis Z, Guatelli S, et al. Geant4-DNA example applications for track structure simulations in liquid water: A report from the Geant4-DNA Project. Med Phys [Internet]. 2018 Aug [cited 2023 Oct 4];45(8). Available from: https://aapm.onlinelibrary.wiley.com/doi/10.1002/mp.13048

40. Incerti S, Baldacchino G, Bernal M, Capra R, Champion C, Francis Z, et al. THE GEANT4-DNA PROJECT. Int J Model Simul Sci Comput. 2010 Jun;01(02):157–78.

41. Bernal MA, Bordage MC, Brown JMC, Davídková M, Delage E, El Bitar Z, et al. Track structure modeling in liquid water: A review of the Geant4-DNA very low energy extension of the Geant4 Monte Carlo simulation toolkit. Phys Med. 2015 Dec;31(8):861–74.

42. Tran HN, Archer J, Baldacchino G, Brown JMC, Chappuis F, Cirrone GAP, et al. Review of chemical models and applications in Geant4-DNA: Report from the ESA BioRad III Project. Med Phys. 2024 Sep;51(9):5873–89.

43. Incerti S, Ivanchenko A, Karamitros M, Mantero A, Moretto P, Tran HN, et al. Comparison of GEANT4 very low energy cross section models with experimental data in water. Med Phys. 2010 Sep;37(9):4692–708.

44. Uehara S, Nikjoo H, Goodhead DT. Cross-sections for water vapour for the Monte Carlo electron track structure code from 10 eV to the MeV region. Phys Med Biol. 1993 Dec 1;38(12):1841–58.

45. Uehara S, Toburen LH, Nikjoo H. Development of a Monte Carlo track structure code for low-energy protons in water. Int J Radiat Biol. 2001 Jan;77(2):139–54.

46. Matsuya Y, Kai T, Sato T, Liamsuwan T, Sasaki K, Nikjoo H. Verification of KURBUC-based ion track structure mode for proton and carbon ions in the PHITS code. Phys Med Biol. 2021 Mar 21;66(6):06NT02.

47. Friedland W, Dingfelder M, Kundrát P, Jacob P. Track structures, DNA targets and radiation effects in the biophysical Monte Carlo simulation code PARTRAC. Mutat Res Mol Mech Mutagen. 2011 Jun;711(1–2):28–40.

48. Plante I, A. F. Monte-Carlo Simulation of Ionizing Radiation Tracks. In: Mode CJ, editor. Applications of Monte Carlo Methods in Biology, Medicine and Other Fields of Science [Internet]. InTech; 2011 [cited 2023 Oct 4]. Available from: http://www.intechopen.com/books/applications-of-monte-carlo-methods-in-biology-medicine-and-other-fields-of-science/monte-carlo-simulation-of-ionizing-radiation-tracks

49. Sato T, Iwamoto Y, Hashimoto S, Ogawa T, Furuta T, Abe SI, et al. Recent improvements of the particle and heavy ion transport code system – PHITS version 3.33. J Nucl Sci Technol. 2023 Oct 31;1–9.

50. Matsuya Y, Kai T, Sato T, Ogawa T, Hirata Y, Yoshii Y, et al. Track-structure modes in particle and heavy ion transport code system (PHITS): application to radiobiological research. Int J Radiat Biol. 2022 Feb 1;98(2):148–57.

51. Braby LA, Conte V, Dingfelder M, Goodhead DT, Pinsky LS, Rosenfeld AB, et al. ICRU Report 98, Stochastic Nature of Radiation Interactions: Microdosimetry. J ICRU. 2023 Dec;23(1):1–168.

52. Xapsos MA, Burke EA, Shapiro P, Summers GP. Energy Deposition and Ionization Fluctuations Induced by Ions in Small Sites: An Analytical Approach. Radiat Res. 1994 Feb;137(2):152.

53. Xapsos MA, Burke EA, Shapiro P, Summers GP. Probability distributions of energy deposition and ionization in sub-micrometer sites of condensed media. Radiat Meas. 1996 Jan;26(1):1–9.

54. Olko P, Booz J. Energy deposition by protons and alpha particles in spherical sites of nanometer to micrometer diameter. Radiat Environ Biophys. 1990 Mar;29(1):1–17.

55. Czopyk L, Olko P. An analytical model for calculating microdosimetric distributions from heavy ions in nanometer site targets. Radiat Prot Dosimetry. 2006 Dec 1;122(1–4):36–40.

56. George JS, Lave KA, Wiedenbeck ME, Binns WR, Cummings AC, Davis AJ, et al. ELEMENTAL COMPOSITION AND ENERGY SPECTRA OF GALACTIC COSMIC RAYS DURING SOLAR CYCLE 23. Astrophys J. 2009 Jun 20;698(2):1666–81.

57. Blasi P. The origin of galactic cosmic rays. Astron Astrophys Rev. 2013 Nov;21(1):70.

58. Mewaldt RA. The elemental and isotopic composition of galactic cosmic ray nuclei. Rev Geophys. 1983 Mar;21(2):295–305.

59. Gosse JC, Phillips FM. Terrestrial in situ cosmogenic nuclides: theory and application. Quat Sci Rev. 2001 Aug;20(14):1475–560.

60. Mrigakshi AI, Matthiä D, Berger T, Reitz G, Wimmer-Schweingruber RF. How Galactic Cosmic Ray models affect the estimation of radiation exposure in space. Adv Space Res. 2013 Mar;51(5):825–34.

61. Tjus JB, Merten L. Closing in on the origin of Galactic cosmic rays using multimessenger information [Internet]. arXiv; 2020 [cited 2024 Jun 26]. Available from: https://arxiv.org/abs/2002.00964

62. Swenberg CE, Horneck G, Stassinopoulos EG, editors. Biological Effects and Physics of Solar and Galactic Cosmic Radiation: Part A [Internet]. Boston, MA: Springer US; 1993 [cited 2024 Jun 25]. Available from: http://link.springer.com/10.1007/978-1-4615-2918-7

63. Townsend LW, Adams JH, Blattnig SR, Clowdsley MS, Fry DJ, Jun I, et al. Solar particle event storm shelter requirements for missions beyond low Earth orbit. Life Sci Space Res. 2018 May;17:32–9.

64. Townsend LW. Effects of Space Radiation on Humans in Space Flight. In: Coster AJ, Erickson PJ, Lanzerotti LJ, Zhang Y, Paxton LJ, editors. Geophysical Monograph Series [Internet]. 1st ed. Wiley; 2021 [cited 2022 Mar 2]. p. 63–78. Available from: https://onlinelibrary.wiley.com/doi/10.1002/9781119815570.ch3

65. Atwell W, Tylka A, Dietrich W, Badavi F, Rojdev K. Spectral Analyses and Radiation Exposures from Several Ground-Level Enhancement (GLE) Solar Proton Events: A Comparison of Methodologies. In: 41st International Conference on Environmental Systems [Internet]. Portland, Oregon: American Institute of Aeronautics and Astronautics; 2011 [cited 2024 Jun 26]. Available from: https://arc.aiaa.org/doi/10.2514/6.2011-5253

66. Townsend LW, Stephens DL, Hoff JL, Zapp EN, Moussa HM, Miller TM, et al. The Carrington event: Possible doses to crews in space from a comparable event. Adv Space Res. 2006 Jan;38(2):226–31.

67. Trovati S, Ballarini F, Battistoni G, Cerutti F, Fassò A, Ferrari A, et al. Human exposure to space radiation: role of primary and secondary particles. Radiat Prot Dosimetry. 2006 Dec 1;122(1–4):362–6.

68. Kim MHY, Hayat MJ, Feiveson AH, Cucinotta FA. PREDICTION OF FREQUENCY AND EXPOSURE LEVEL OF SOLAR PARTICLE EVENTS. Health Phys. 2009 Jul;97(1):68–81.

69. Reitz G, Beaujean R, Benton E, Burmeister S, Dachev T, Deme S, et al. Space radiation measurements on-board ISS--the DOSMAP experiment. Radiat Prot Dosimetry. 2005;116(1-4 Pt 2):374–9.

70. Badhwar GD. The radiation environment in low-Earth orbit. Radiat Res. 1997 Nov;148(5 Suppl):S3-10.

71. Badhwar GD. Radiation Measurements in Low Earth Orbit: U.S. and Russian Results: Health Phys. 2000 Nov;79(5):507–14.

72. Badhwar GD. Shuttle Radiation Dose Measurements in the International Space Station Orbits [1]. Radiat Res. 2002 Jan;157(1):69–75.

73. Badhwar GD. Radiation dose rates in Space Shuttle as a function of atmospheric density. Radiat Meas. 1999 Jun;30(3):401–14.

74. Badhwar GD, Patel JU, Konradi A, Cucinotta FA, Kern JW. Trapped particle energy spectrum in shuttle middeck. Adv Space Res. 1996 Jan;18(12):149–57.

75. Badhwar GD, Atwell W, Benton EV, Frank AL, Keegan RP, Dudkin VE, et al. A study of the radiation environment on board the Space Shuttle flight STS-57. Radiat Meas. 1995 Jul;24(3):283–9.

76. Badhwar GD, Atwell W, Cash B, Petrov VM, Akatov YuA, Tchernykh IV, et al. Radiation environment on the Mir orbital station during solar minimum. Adv Space Res. 1998 Jan;22(4):501–10.

77. Badhwar GD, Braby LA, Cucinotta FA, Atwell W. Dose rate, dose-equivalent rate, and quality factor in SLS-1. Int J Radiat Appl Instrum Part Nucl Tracks Radiat Meas. 1992 Jul;20(3):447–51.

78. Badhwar GD, Cucinotta FA. Depth Dependence of Absorbed Dose, Dose Equivalent and Linear Energy Transfer Spectra of Galactic and Trapped Particles in Polyethylene and Comparison with Calculations of Models. Radiat Res. 1998 Mar;149(3):209.

79. Goodhead D. Track structure and the quality factor for space radiation cancer risk https://three.jsc.nasa.gov/articles/Track_QF_Goodhead.pdf. 2018 Aug 28;

80. Denisov AN, Kuznetsov NV, Nymmik RA, Panasyuk MI, Sobolevsky NM. Assessment of the radiation environment on the Moon. Acta Astronaut. 2011 May;68(9–10):1440–7.

81. Naito M, Hasebe N, Shikishima M, Amano Y, Haruyama J, Matias-Lopes JA, et al. Radiation dose and its protection in the Moon from galactic cosmic rays and solar energetic particles: at the lunar surface and in a lava tube. J Radiol Prot. 2020 Dec;40(4):947–61.

82. Reitz G, Berger T, Matthiae D. Radiation exposure in the moon environment. Planet Space Sci. 2012 Dec;74(1):78–83.

83. Akisheva Y, Gourinat Y. Utilisation of Moon Regolith for Radiation Protection and Thermal Insulation in Permanent Lunar Habitats. Appl Sci. 2021 Apr 24;11(9):3853.

84. Tripathi RK, Wilson JW, Badavi FF, De Angelis G. A characterization of the moon radiation environment for radiation analysis. Adv Space Res. 2006 Jan;37(9):1749–58.

85. Dachev TP, Tomov BT, Matviichuk YuN, Dimitrov PS, Vadawale SV, Goswami JN, et al. An overview of RADOM results for earth and moon radiation environment on Chandrayaan-1 satellite. Adv Space Res. 2011 Sep;48(5):779–91.

86. Lund M, Jevremovic T. Enhanced GEANT4 Monte Carlo simulations of the space radiation effects on the International Space Station and Apollo missions using high-performance computing environment. Acta Astronaut. 2019 Dec;165:219–28.

87. Zhang S, Wimmer-Schweingruber RF, Yu J, Wang C, Fu Q, Zou Y, et al. First measurements of the radiation dose on the lunar surface. Sci Adv. 2020 Sep 25;6(39):eaaz1334.

88. Adamczyk A, Clowdsley M, Qualls G, Blattnig S, Lee K, Fry D, et al. Full mission astronaut radiation exposure assessments for long duration lunar surface missions. In: 2011 Aerospace Conference [Internet]. Big Sky, USA: IEEE; 2011 [cited 2024 Jun 26]. p. 1–15. Available from: http://ieeexplore.ieee.org/document/5747250/

89. Tripathi RK, Nealy JE. Lunar Radiation Risk Assessment and Shielding Design for Ionizing Space Radiation. In: 2008 IEEE Aerospace Conference [Internet]. Big Sky, MT, USA: IEEE; 2008 [cited 2024 Jun 26]. p. 1–11. Available from: http://ieeexplore.ieee.org/document/4526267/

90. Adams JH, Bhattacharya M, Lin ZW, Pendleton G, Watts JW. The ionizing radiation environment on the moon. Adv Space Res. 2007 Jan;40(3):338–41.

91. Townsend LW, Adamczyk AM, Werneth CM, Moussa HM, Townsend JP. Estimates of extreme solar particle event radiation exposures on Mars. Prog Nucl Sci Technol. 2014;4:793–7.

92. Zeitlin C, Hassler DM, Cucinotta FA, Ehresmann B, Wimmer-Schweingruber RF, Brinza DE, et al. Measurements of Energetic Particle Radiation in Transit to Mars on the Mars Science Laboratory. Science. 2013 May 31;340(6136):1080–4.

93. Zaman FA, Townsend LW, Burahmah NT. Radiation Risks in a Mission to Mars for a Solar Particle Event Similar to the AD 993/4 Event. Aerospace. 2021 May 20;8(5):143.

94. Perminov VG. The difficult road to Mars: a brief history of Mars exploration in the Soviet Union. Washington, D.C: National Aeronautics and Space Administration Headquarters; 1999. 79 p. (Monographs in aerospace history).

95. Matthiä D, Ehresmann B, Lohf H, Köhler J, Zeitlin C, Appel J, et al. The Martian surface radiation environment – a comparison of models and MSL/RAD measurements. J Space Weather Space Clim. 2016;6:A13.

96. Matthiä D, Hassler DM, De Wet W, Ehresmann B, Firan A, Flores-McLaughlin J, et al. The radiation environment on the surface of Mars - Summary of model calculations and comparison to RAD data. Life Sci Space Res. 2017 Aug;14:18–28.

97. Matthiä D, Berger T. The radiation environment on the surface of Mars – Numerical calculations of the galactic component with GEANT4/PLANETOCOSMICS. Life Sci Space Res. 2017 Aug;14:57–63.

98. Townsend LW, PourArsalan M, Cucinotta FA, Kim MY, Schwadron NA. Transmission of galactic cosmic rays through Mars atmosphere. Space Weather. 2011 Jun;9(6):2009SW000564.

99. Charles MW. ICRP Publication 103: Recommendations of the ICRP. Radiat Prot Dosimetry. 2007 Oct 19;129(4):500–7.

100. United Nations, editor. Sources and effects of ionizing radiation: United Nations Scientific Committee on the Effects of Atomic Radiation: UNSCEAR 2008 report to the General Assembly, with scientific annexes. New York: United Nations; 2010. 2 p.

101. International Commission on Radiation Units and Measurements. J ICRU. 2014 Apr;14(1):NP.1-NP.

102. Goodhead DT. An Assessment of the Role of Microdosimetry in Radiobiology. Radiat Res. 1982 Jul;91(1):45.

103. Valentin J, International Commission on Radiological Protection, editors. The 2007 recommendations of the International Commission on Radiological Protection. Oxford: Elsevier; 2007. 332 p. (ICRP publication).

104. Maalouf M, Durante M, Foray N. Biological Effects of Space Radiation on Human Cells: History, Advances and Outcomes. J Radiat Res (Tokyo). 2011;52(2):126–46.

105. Hu S, Kim MHY, McClellan GE, Cucinotta FA. MODELING THE ACUTE HEALTH EFFECTS OF ASTRONAUTS FROM EXPOSURE TO LARGE SOLAR PARTICLE EVENTS. Health Phys. 2009 Apr;96(4):465–76.

106. Chancellor J, Scott G, Sutton J. Space Radiation: The Number One Risk to Astronaut Health beyond Low Earth Orbit. Life. 2014 Sep 11;4(3):491–510.

107. Petrie G, Criscuoli S, Bertello L. Solar Magnetism and Radiation. In: Raouafi NE, Vourlidas A, Zhang Y, Paxton LJ, editors. Geophysical Monograph Series [Internet]. 1st ed. Wiley; 2021 [cited 2024 Jun 25]. p. 83–132. Available from: https://agupubs.onlinelibrary.wiley.com/doi/10.1002/9781119815600.ch3

108. Furukawa S, Nagamatsu A, Nenoi M, Fujimori A, Kakinuma S, Katsube T, et al. Space Radiation Biology for “Living in Space.” BioMed Res Int. 2020 Apr 8;2020:1–25.

109. Brinckmann E. Biology in space and life on Earth: effects of spaceflight on biological systems. Weinheim: Wiley-VCH; 2007.

110. Kennedy AR. Biological effects of space radiation and development of effective countermeasures. Life Sci Space Res. 2014 Apr;1:10–43.

111. Cucinotta FA. A New Approach to Reduce Uncertainties in Space Radiation Cancer Risk Predictions. Janssen PJ, editor. PLOS ONE. 2015 Mar 19;10(3):e0120717.

112. Cucinotta FA. Flying without a Net: Space Radiation Cancer Risk Predictions without a Gamma-ray Basis. Int J Mol Sci. 2022 Apr 13;23(8):4324.

113. Cucinotta FA, Durante M. Cancer risk from exposure to galactic cosmic rays: implications for space exploration by human beings. Lancet Oncol. 2006 May;7(5):431–5.

114. Cucinotta FA, Kim MHY, Ren L. Evaluating shielding effectiveness for reducing space radiation cancer risks. Radiat Meas. 2006 Oct;41(9–10):1173–85.

115. Britten RA, Limoli CL. New Radiobiological Principles for the CNS Arising from Space Radiation Research. Life. 2023 May 31;13(6):1293.

116. Tinganelli W, Luoni F, Durante M. What can space radiation protection learn from radiation oncology? Life Sci Space Res. 2021 Aug;30:82–95.

117. Little MP, Azizova TV, Richardson DB, Tapio S, Bernier MO, Kreuzer M, et al. Ionising radiation and cardiovascular disease: systematic review and meta-analysis. BMJ. 2023 Mar 8;e072924.

118. Hughson RL, Helm A, Durante M. Heart in space: effect of the extraterrestrial environment on the cardiovascular system. Nat Rev Cardiol. 2018 Mar;15(3):167–80.

119. Reynolds RJ, Day SM. Mortality Due to Cardiovascular Disease Among Apollo Lunar Astronauts. Aerosp Med Hum Perform. 2017 May 1;88(5):492–6.

120. Meerman M, Bracco Gartner TCL, Buikema JW, Wu SM, Siddiqi S, Bouten CVC, et al. Myocardial Disease and Long-Distance Space Travel: Solving the Radiation Problem. Front Cardiovasc Med. 2021 Feb 12;8:631985.

121. Elgart SR, Little MP, Chappell LJ, Milder CM, Shavers MR, Huff JL, et al. Radiation Exposure and Mortality from Cardiovascular Disease and Cancer in Early NASA Astronauts. Sci Rep. 2018 May 31;8(1):8480.

122. Little MP, Azizova TV, Bazyka D, Bouffler SD, Cardis E, Chekin S, et al. Systematic Review and Meta-analysis of Circulatory Disease from Exposure to Low-Level Ionizing Radiation and Estimates of Potential Population Mortality Risks. Environ Health Perspect. 2012 Nov;120(11):1503–11.

123. Committee on Assessment of Strategies for Managing Cancer Risks Associated with Radiation Exposure During Crewed Space Missions, Board on Health Sciences Policy, Board on Health Care Services, Nuclear and Radiation Studies Board, Health and Medicine Division, Division on Earth and Life Studies, et al. Space Radiation and Astronaut Health: Managing and Communicating Cancer Risks [Internet]. Washington, D.C.: National Academies Press; 2021 [cited 2024 Jun 26]. Available from: https://www.nap.edu/catalog/26155

124. Boscolo D, Durante M. Dose Limits and Countermeasures for Mitigating Radiation Risk in Moon and Mars Exploration. Physics. 2022 Feb 9;4(1):172–84.

125. Santa Cruz GA. Microdosimetry: Principles and applications. Rep Pract Oncol Radiother. 2016 Mar;21(2):135–9.

126. M. Kellerer A. Microdosimetry: Reflections on Harald Rossi. Radiat Prot Dosimetry. 2002 Jun 1;99(1):17–22.

127. Kellerer AM. A survey of microdosimetric quantities and concepts. Ultramicroscopy. 1984 Jan;14(3):169–74.

128. Kellerer AM, Chmelevsky D. Criteria for the Applicability of LET. Radiat Res. 1975 Aug;63(2):226.

129. Kellerer AM. Chord-Length Distributions and Related Quantities for Spheroids. Radiat Res. 1984 Jun;98(3):425.

130. Incerti S, Kyriakou I, Bernal MA, Bordage MC, Francis Z, Guatelli S, et al. Geant4-DNA example applications for track structure simulations in liquid water: A report from the Geant4-DNA Project. Med Phys [Internet]. 2018 Aug [cited 2023 Oct 4];45(8). Available from: https://aapm.onlinelibrary.wiley.com/doi/10.1002/mp.13048

131. Agostinelli S, Allison J, Amako K, Apostolakis J, Araujo H, Arce P, et al. Geant4—a simulation toolkit. Nucl Instrum Methods Phys Res Sect Accel Spectrometers Detect Assoc Equip. 2003 Jul;506(3):250–303.

132. Allison J, Amako K, Apostolakis J, Arce P, Asai M, Aso T, et al. Recent developments in Geant4. Nucl Instrum Methods Phys Res Sect Accel Spectrometers Detect Assoc Equip. 2016 Nov;835:186–225.

133. Allison J, Amako K, Apostolakis J, Araujo H, Arce Dubois P, Asai M, et al. Geant4 developments and applications. IEEE Trans Nucl Sci. 2006 Feb;53(1):270–8.

134. Rising M, Armstrong J, Bolding S, Brown F, Bull J, Burke T, et al. MCNP® Code V.6.3.0 Release Notes [Internet]. 2023 Jan [cited 2023 Oct 16] p. LA-UR-22-33103, 1909545. Report No.: LA-UR-22-33103, 1909545. Available from: https://www.osti.gov/servlets/purl/1909545/

135. Ferrari A, Sala PR, Fasso A, Ranft J. FLUKA: A Multi-Particle Transport Code [Internet]. 2005 Dec [cited 2023 Oct 16] p. SLAC-R-773, 877507. Report No.: SLAC-R-773, 877507. Available from: http://www.osti.gov/servlets/purl/877507-sC9S9L/

136. Battistoni G, Bauer J, Boehlen TT, Cerutti F, Chin MPW, Dos Santos Augusto R, et al. The FLUKA Code: An Accurate Simulation Tool for Particle Therapy. Front Oncol [Internet]. 2016 May 11 [cited 2023 Oct 4];6. Available from: http://journal.frontiersin.org/Article/10.3389/fonc.2016.00116/abstract

137. Salvat F, Fernandez-Varea JM, Sempau J. PENELOPE-2006: a code system for Monte Carlo simulation of electron and photon transport : workshop proceedings, Barcelona, Spain, 4-7 July 2006. Paris: Nuclear Energy Agency, Organisation for Economic Co-operation and Development; 2006.

138. Stewart RD, Wilson WE, McDonald JC, Strom DJ. Microdosimetric properties of ionizing electrons in water: a test of the PENELOPE code system. Phys Med Biol. 2002 Jan 1;47(1):79–88.

139. Fernández-Varea JM, González-Muñoz G, Galassi ME, Wiklund K, Lind BK, Ahnesjö A, et al. Limitations (and merits) of PENELOPE as a track-structure code. Int J Radiat Biol. 2012 Jan;88(1–2):66–70.

140. Goorley JT, James MR, Booth TE, Bull JS, Cox LJ, Durkee JWJr, et al. Initial MCNP6 Release Overview - MCNP6 version 1.0 [Internet]. 2013 Jun [cited 2023 Oct 16] p. LA-UR-13-22934, 1086758. Report No.: LA-UR-13-22934, 1086758. Available from: http://www.osti.gov/servlets/purl/1086758/

141. Matsuya Y, Kai T, Sato T, Liamsuwan T, Sasaki K, Nikjoo H. Verification of KURBUC-based ion track structure mode for proton and carbon ions in the PHITS code. Phys Med Biol. 2021 Mar 21;66(6):06NT02.

142. Stewart RD, Streitmatter SW, Argento DC, Kirkby C, Goorley JT, Moffitt G, et al. Rapid MCNP simulation of DNA double strand break (DSB) relative biological effectiveness (RBE) for photons, neutrons, and light ions. Phys Med Biol. 2015 Nov 7;60(21):8249–74.

143. Wilson WE, Metting NF, Paretzke HG. Microdosimetric Aspects of 0.3- to 20-MeV Proton Tracks: I. Crossers. Radiat Res. 1988 Sep;115(3):389.

144. Xapsos MA, Burke EA, Shapiro P, Summers GP. Energy Deposition and Ionization Fluctuations Induced by Ions in Small Sites: An Analytical Approach. Radiat Res. 1994 Feb;137(2):152.

145. Wilson WE, Paretzke HG. A Stochastic Model of Ion Track Structure. Radiat Prot Dosimetry. 1994 Apr 1;52(1–4):249–53.

146. Czopyk L, Olko P. An analytical model for calculating microdosimetric distributions from heavy ions in nanometer site targets. Radiat Prot Dosimetry. 2006 Dec 1;122(1–4):36–40.

147. Simonsen και Slaba - Ensemble Methodologies for Astronaut Cancer Risk A.pdf [Internet]. [cited 2024 Jun 26]. Available from: https://spaceradiation.larc.nasa.gov/nasapapers/2020/5008710.pdf

148. Chappell LJ, Milder CM, Elgart SR. NASA Space Cancer Risk Model: 2020 Operational Implementation [Internet]. 2021 May [cited 2024 Jun 26]. Available from: https://ntrs.nasa.gov/citations/20210013314

149. Papadopoulos A, Kyriakou I, Matsuya Y, Incerti S, Daglis IA, Emfietzoglou D. Microdosimetry Study of Proton Quality Factor Using Analytic Model Calculations. Appl Sci. 2022 Sep 6;12(18):8950.

150. Katz R, Ackerson B, Homayoonfar M, Sharma SC. Inactivation of Cells by Heavy Ion Bombardment. Radiat Res. 1971 Aug 1;47(2):402–25.

151. Badavi FF, Xapsos MA, Wilson JW. An analytical model for the prediction of a micro-dosimeter response function. Adv Space Res. 2009 Jul;44(2):190–201.

152. Badhwar GD, Atwell W, Badavi FF, Yang TC, Cleghorn TF. Space Radiation Absorbed Dose Distribution in a Human Phantom. Radiat Res. 2002 Jan;157(1):76–91.

153. Badavi F, Stewart-Sloan C, Xapsos M, Shinn J, Wilson J. NASA/TP-2007-214886 Description of a Generalized Analytical Model for the Micro-dosimeter Response. 2008 Dec 30;

154. Badhwar GD, Golightly MJ, Konradi A, Atwell W, Kern JW, Cash B, et al. In-flight radiation measurements on STS-60. Radiat Meas. 1996 Jan;26(1):17–34.

155. Shuryak I, Slaba TC, Plante I, Poignant F, Blattnig SR, Brenner DJ. A practical approach for continuous in situ characterization of radiation quality factors in space. Sci Rep. 2022 Jan 27;12(1):1453.

156. Xapsos MA. A Spatially Restricted Linear Energy Transfer Equation. Radiat Res. 1992 Dec;132(3):282.

157. Kyriakou I, Šefl M, Nourry V, Incerti S. The impact of new Geant4-DNA cross section models on electron track structure simulations in liquid water. J Appl Phys. 2016 May 21;119(19):194902.

158. Emfietzoglou D, Kostarelos K, Hadjidoukas P, Bousis C, Fotopoulos A, Pathak A, et al. Subcellular S-factors for low-energy electrons: A comparison of Monte Carlo simulations and continuous-slowing-down calculations. Int J Radiat Biol. 2008 Jan;84(12):1034–44.

159. Scribd [Internet]. [cited 2024 Jun 26]. Icru 16 PDF | Download Free PDF | Dosimetry | Ionizing Radiation. Available from: https://www.scribd.com/document/348566223/170774815-ICRU-16-pdf

160. Shinn JL, Badhwar GD, Xapsos MA, Cucinotta FA, Wilson JW. An analysis of energy deposition in a tissue equivalent proportional counter onboard the space shuttle. Radiat Meas. 1999 Feb;30(1):19–28.

161. Singleterry RC, Blattnig SR, Clowdsley MS, Qualls GD, Sandridge CA, Simonsen LC, et al. OLTARIS: On-line tool for the assessment of radiation in space. Acta Astronaut. 2011 Apr;68(7–8):1086–97.

162. Slaba T, Whitman K. The Badhwar-O'Neill 2020 GCR Model. Space Weather. 2020 Jun 1;18.

163. Papadopoulos A, Kyriakou I, Matsuya Y, Incerti S, Daglis IA, Emfietzoglou D. Microdosimetry Study of Proton Quality Factor Using Analytic Model Calculations. Appl Sci. 2022 Sep 6;12(18):8950.

164. Beaujean R, Reitz G, Kopp J. Recent European measurements inside Biorack. Mutat Res Mol Mech Mutagen. 1999 Dec 6;430(2):183–9.

165. Doke T, Hayashi T, Borak TB. Comparisons of LET Distributions Measured in Low-Earth Orbit Using Tissue-Equivalent Proportional Counters and the Position-Sensitive Silicon-Detector Telescope (RRMD-III). Radiat Res. 2001 Sep;156(3):310–6.

166. On Orbit Status of the ISS Intravehicular Tissue Equivalent Proportional Counter (IV-TEPC). :31.

167. Hassler DM, Zeitlin C, Wimmer-Schweingruber RF, Ehresmann B, Rafkin S, Eigenbrode JL, et al. Mars' Surface Radiation Environment Measured with the Mars Science Laboratory's Curiosity Rover. Science. 2014 Jan 24;343(6169):1244797.

168. Simpson JA. Elemental and Isotopic Composition of the Galactic Cosmic Rays. Annu Rev Nucl Part Sci. 1983 Dec;33(1):323–82.

169. Straume T, Slaba TC, Bhattacharya S, Braby LA. Cosmic-ray interaction data for designing biological experiments in space. Life Sci Space Res. 2017 May;13:51–9.

170. Wilson J, Miller J, Konradi A, Cucinotta F. Shielding Strategies for Human Space Exploration. 1998 Apr 12;

171. Sager PH. Radiation shield requirements for manned nuclear propulsion space vehicles. In: AIP Conference Proceedings [Internet]. Albuquerque, New Mexico (USA): AIP; 1992 [cited 2023 Feb 16]. p. 1251–8. Available from: http://aip.scitation.org/doi/abs/10.1063/1.41746

172. Adams J, Hathaway D, Grugel R, Watts J, Parnell T, Gregory J, et al. Revolutionary Concepts of Radiation Shielding for Human Exploration of Space. 2005 Apr 1;

173. Naito M, Kodaira S, Ogawara R, Tobita K, Someya Y, Kusumoto T, et al. Investigation of shielding material properties for effective space radiation protection. Life Sci Space Res. 2020 Aug 1;26:69–76.

174. Gohel A, Makwana R. Multi-layered shielding materials for high energy space radiation. Radiat Phys Chem. 2022 Aug 1;197:110131.

175. Nikjoo H, Uehara S, Emfietzoglou D, Pinsky L. A database of frequency distributions of energy depositions in small-size targets by electrons and ions. Radiat Prot Dosimetry. 2011 Feb 1;143(2–4):145–51.

176. Xapsos MA. A spatially restricted linear energy transfer equation. Radiat Res. 1992 Dec;132(3):282–7.

177. Chancellor J, Nowadly C, Williams J, Aunon-Chancellor S, Chesal M, Looper J, et al. Everything you wanted to know about space radiation but were afraid to ask. J Environ Sci Health Part C. 2021 Apr 3;39(2):113–28.

178. Emfietzoglou D. Inelastic cross-sections for electron transport in liquid water: a comparison of dielectric models. Radiat Phys Chem. 2003 Apr;66(6):373–85.

179. Kyriakou I, Šefl M, Nourry V, Incerti S. The impact of new Geant4-DNA cross section models on electron track structure simulations in liquid water. J Appl Phys. 2016 May 21;119(19):194902.

180. Spencer LV, Attix FH. A Theory of Cavity Ionization. Radiat Res. 1955 Nov;3(3):239.

181. Salvat F. A generic algorithm for Monte Carlo simulation of proton transport. Nucl Instrum Methods Phys Res Sect B Beam Interact Mater At. 2013 Dec;316:144–59.

182. Ritchie RH. Energy losses by swift charged particles in the bulk and at the surface of condensed matter. Nucl Instrum Methods Phys Res. 1982 Jul;198(1):81–91.

183. Emfietzoglou D, Cucinotta FA, Nikjoo H. A Complete Dielectric Response Model for Liquid Water: A Solution of the Bethe Ridge Problem. Radiat Res. 2005 Aug;164(2):202–11.

184. Emfietzoglou D, Papamichael G, Nikjoo H. Monte Carlo Electron Track Structure Calculations in Liquid Water Using a New Model Dielectric Response Function. Radiat Res. 2017 Sep;188(3):355–68.

185. Nikjoo H, Uehara S, Emfietzoglou D. Interaction of Radiation with Matter [Internet]. 0 ed. CRC Press; 2016 [cited 2023 Oct 4]. Available from: https://www.taylorfrancis.com/books/9781466509603

186. Kyriakou I, Emfietzoglou D, Incerti S. Status and Extension of the Geant4-DNA Dielectric Models for Application to Electron Transport. Front Phys. 2022 Jan 13;9:711317.

187. Dingfelder M. Updated model for dielectric response function of liquid water. Appl Radiat Isot. 2014 Jan;83:142–7.

188. Garcia-Molina R, Abril I, Kyriakou I, Emfietzoglou D. Inelastic scattering and energy loss of swift electron beams in biologically relevant materials. Surf Interface Anal. 2017 Jan;49(1):11–7.

189. Fernández-Varea JM, Llovet X, Salvat F. Cross sections for electron interactions in condensed matter. Surf Interface Anal. 2005 Nov;37(11):824–32.

190. Incerti S, Ivanchenko A, Karamitros M, Mantero A, Moretto P, Tran HN, et al. Comparison of GEANT4 very low energy cross section models with experimental data in water. Med Phys. 2010 Sep;37(9):4692–708.

191. Baratto-Roldán A, Bertolet A, Baiocco G, Carabe A, Cortés-Giraldo MA. Microdosimetry and Dose-Averaged LET Calculations of Protons in Liquid Water: A Novel Geant4-DNA Application. Front Phys. 2021 Oct 27;9:726787.

192. Tabata T, Ito R, Okabe S. Generalized semiempirical equations for the extrapolated range of electrons. Nucl Instrum Methods. 1972 Aug;103(1):85–91.

193. Bertolet A, Baratto-Roldán A, Barbieri S, Baiocco G, Carabe A, Cortés-Giraldo MA. Dose-averaged LET calculation for proton track segments using microdosimetric Monte Carlo simulations. Med Phys. 2019 Sep;46(9):4184–92.

194. Domínguez-Muñoz AD, Gallardo MI, Bordage MC, Francis Z, Incerti S, Cortés-Giraldo MA. A model for Geant4-DNA to simulate ionization and excitation of liquid water by protons travelling above 100 MeV. Radiat Phys Chem. 2022 Oct;199:110363.

195. Sato T, Watanabe R, Niita K. Development of a calculation method for estimating specific energy distribution in complex radiation fields. Radiat Prot Dosimetry. 2006 Dec 1;122(1–4):41–5.

196. Sato T, Kase Y, Watanabe R, Niita K, Sihver L. Biological Dose Estimation for Charged-Particle Therapy Using an Improved PHITS Code Coupled with a Microdosimetric Kinetic Model. Radiat Res. 2009 Jan;171(1):107–17.

197. Tomita H, Kai M, Kusama T, Ito A. Monte Carlo simulation of physicochemical processes of liquid water radiolysis. Radiat Environ Biophys. 1997 Jul 30;36(2):105–16.

198. Plante I, Poignant F, Slaba T. Track Structure Components: Characterizing Energy Deposited in Spherical Cells from Direct and Peripheral HZE Ion Hits. Life. 2021 Oct 20;11(11):1112.

199. Plante I, Ponomarev A, Cucinotta FA. 3D visualisation of the stochastic patterns of the radial dose in nano-volumes by a Monte Carlo simulation of HZE ion track structure. Radiat Prot Dosimetry. 2011 Feb 1;143(2–4):156–61.

200. Plante I, Devroye L. Considerations for the independent reaction times and step-by-step methods for radiation chemistry simulations. Radiat Phys Chem. 2017 Oct;139:157–72.

201. Plante I, Slaba T, Shavers Z, Hada M. A Bi-Exponential Repair Algorithm for Radiation-Induced Double-Strand Breaks: Application to Simulation of Chromosome Aberrations. Genes. 2019 Nov 16;10(11):936.

202. Slaba TC, Plante I, Ponomarev A, Patel ZS, Hada M. Determination of Chromosome Aberrations in Human Fibroblasts Irradiated by Mixed Fields Generated with Shielding. Radiat Res. 2020 Jul 16;194(3):246.

203. Semenenko VA, Stewart RD. A Fast Monte Carlo Algorithm to Simulate the Spectrum of DNA Damages Formed by Ionizing Radiation. Radiat Res. 2004 Apr;161(4):451–7.

204. Semenenko VA, Stewart RD. Fast Monte Carlo simulation of DNA damage formed by electrons and light ions. Phys Med Biol. 2006 Apr 7;51(7):1693–706.

205. Stewart RD, Yu VK, Georgakilas AG, Koumenis C, Park JH, Carlson DJ. Effects of Radiation Quality and Oxygen on Clustered DNA Lesions and Cell Death. Radiat Res. 2011 Nov;176(5):587–602.

206. Vaeth M, Pierce DA. Calculating excess lifetime risk in relative risk models. Environ Health Perspect. 1990 Jul;87:83–94.

207. Cucinotta FA, Cacao E, Kim MHY, Saganti PB. Benchmarking risk predictions and uncertainties in the NSCR model of GCR cancer risks with revised low let risk coefficients. Life Sci Space Res. 2020 Nov;27:64–73.

208. Cucinotta FA, Saganti PB. Race and ethnic group dependent space radiation cancer risk predictions. Sci Rep. 2022 Feb 7;12(1):2028.

209. Health Risks from Exposure to Low Levels of Ionizing Radiation: BEIR VII Phase 2 [Internet]. Washington, D.C.: National Academies Press; 2006 [cited 2024 Jun 26]. Available from: http://www.nap.edu/catalog/11340

210. Cucinotta FA. Space Radiation Risks for Astronauts on Multiple International Space Station Missions. Janssen PJ, editor. PLoS ONE. 2014 Apr 23;9(4):e96099.

211. United States Life Tables, 2020 [Internet]. National Center for Health Statistics (U.S.); 2022 Aug [cited 2024 Jun 26]. Available from: https://stacks.cdc.gov/view/cdc/118055

212. CDC WONDER [Internet]. [cited 2024 Jun 26]. Available from: https://wonder.cdc.gov/

213. Walsh L, Hafner L, Berger T, Matthiä D, Schneider U, Straube U. European astronaut radiation related cancer risk assessment using dosimetric calculations of organ dose equivalents. Z Für Med Phys. 2023 Nov;S0939388923001198.

214. Cucinotta FA, Chappell LJ, Kim MHY, Wang M. Radiation Carcinogenesis Risk Assessments for Never-smokers. Health Phys. 2012 Nov;103(5):643–51.

215. Cucinotta FA. Biophysics of NASA radiation quality factors. Radiat Prot Dosimetry. 2015 Sep;166(1–4):282–9.

216. Cucinotta FA, Chappell LJ. Updates to Astronaut Radiation Limits: Radiation Risks for Never-Smokers. Radiat Res. 2011 Jul;176(1):102–14.

217. Ulanowski A, Ban N, Ozasa K, Rühm W, Semones E, Shavers M, et al. Time-integrated radiation risk metrics and interpopulation variability of survival. Z Für Med Phys. 2024 Feb;34(1):64–82.

218. Managing Lunar and Mars Mission Radiation Risks - NASA Technical Reports Server (NTRS) [Internet]. [cited 2024 Jun 26]. Available from: https://ntrs.nasa.gov/citations/20050196720

# Appendix A

We present the $y_D$ and TDRA Q values of our work, for liquid water spheres of 1 μm, 100 nm and 10 nm. The calculated $y_D$ values were obtained from the extended Xapsos models (X94, Xcom), using the methodology outlined in chapters and 3 and 4, and from our new microdosimetric model (denoted as 'New Model') with two distinct energy-loss straggling distributions (Erlang and Logistic). The calculated $y_D$ values from our upgraded microdosimetric model are referenced in the methodology of chapter 5.

**Table A1**. $y_D$ values calculated for 1 μm, 100 nm and 10 nm liquid water sphere targets, using three different model, X94, Xcom (chapters 3 and 4) and New Model (Logistic and Erlang distributions, chapter 5), for the proton energy range of 1 MeV- 1000 MeV.

| T (MeV) | X94 (1μm) | Xcom (1μm) | New Model (Logistic) (1μm) | New Model (Erlang) (1μm) |
|---|---|---|---|---|
| **1** | 30,64 | 30,11 | 34,14 | 34,26 |
| **2** | 18,99 | 18,83 | 21,05 | 21,15 |
| **5** | 9,23 | 9,31 | 10,22 | 10,32 |
| **10** | 5,42 | 5,52 | 5,93 | 6,04 |
| **20** | 3,50 | 3,60 | 3,65 | 3,79 |
| **50** | 2,42 | 2,51 | 2,21 | 2,40 |
| **100** | 2,14 | 2,21 | 1,77 | 2,01 |
| **200** | 2,12 | 2,16 | 1,62 | 1,90 |
| **300** | 2,21 | 2,22 | 1,55 | 1,85 |
| **500** | 2,54 | 2,48 | 1,53 | 1,85 |
| **1000** | 4,33 | 3,97 | 1,50 | 1,84 |

| T (MeV) | X94 (100nm) | Xcom (100nm) | New Model (Logistic) (100nm) | New Model (Erlang) (100nm) |
|---|---|---|---|---|
| **1** | 32,20 | 32,28 | 34,92 | 35,27 |
| **2** | 19,62 | 19,66 | 20,75 | 21,16 |
| **5** | 11,39 | 11,40 | 11,30 | 11,85 |
| **10** | 8,69 | 8,69 | 7,92 | 8,63 |
| **20** | 7,46 | 7,46 | 6,15 | 7,06 |
| **50** | 6,92 | 6,95 | 5,12 | 6,30 |
| **100** | 6,92 | 6,98 | 4,69 | 6,04 |

| | | | | |
|---|---|---|---|---|
| **200** | 7,12 | 7,22 | 4,57 | 6,05 |
| **300** | 7,30 | 7,44 | 4,55 | 6,09 |
| **500** | 7,62 | 7,85 | 4,53 | 6,12 |
| **1000** | 8,37 | 8,78 | 4,46 | 6,09 |

| T (MeV) | X94 (10nm) | Xcom (10nm) | New Model (Logistic) (10nm) | New Model (Erlang) (10nm) |
|---|---|---|---|---|
| **1** | 32,80 | 32,93 | 29,00 | 30,38 |
| **2** | 26,39 | 26,49 | 20,61 | 22,24 |
| **5** | 22,64 | 22,73 | 14,72 | 16,81 |
| **10** | 21,67 | 21,77 | 12,37 | 14,89 |
| **20** | 21,48 | 21,58 | 11,24 | 14,13 |
| **50** | 21,72 | 21,85 | 10,26 | 13,60 |
| **100** | 21,89 | 22,06 | 9,84 | 13,45 |
| **200** | 21,70 | 21,91 | 9,66 | 13,46 |
| **300** | 21,26 | 21,52 | 9,58 | 13,46 |
| **500** | 20,30 | 20,59 | 9,46 | 13,41 |
| **1000** | 18,36 | 18,68 | 9,38 | 13,39 |

**Table A2**. TDRA-based Q values calculated for 1 μm, 100 nm and 10 nm liquid water sphere targets, using three different model, X94, Xcom and New Model (incorporating the Logistic and Erlang distributions), across the proton energy range of 1 MeV- 1000 MeV. The $y_D$ values required for the calculation of the Q values are obtained from table A1 of the Appendix.

| T (MeV) | X94 (1μm) | Xcom (1μm) | New Model (Logistic) (1μm) | New Model (Erlang) (1μm) |
|---|---|---|---|---|
| **1** | 14,28 | 13,62 | 19,23 | 17,04 |
| **2** | 8,85 | 8,51 | 11,86 | 10,52 |
| **5** | 4,30 | 4,21 | 5,76 | 5,14 |
| **10** | 2,53 | 2,50 | 3,34 | 3,00 |
| **20** | 1,63 | 1,63 | 2,06 | 1,88 |
| **50** | 1,13 | 1,13 | 1,25 | 1,20 |

| | | | | |
|---|---|---|---|---|
| **100** | 1,00 | 1,00 | 1,00 | 1,00 |
| **200** | 0,99 | 0,98 | 0,91 | 0,94 |
| **300** | 1,03 | 1,01 | 0,87 | 0,92 |
| **500** | 1,18 | 1,12 | 0,86 | 0,92 |
| **1000** | 2,02 | 1,80 | 0,85 | 0,91 |

| T (MeV) | X94 (100nm) | Xcom (100nm) | New Model (Logistic) (100nm) | New Model (Erlang) (100nm) |
|---|---|---|---|---|
| **1** | 4,65 | 4,63 | 7,44 | 5,84 |
| **2** | 2,83 | 2,82 | 4,42 | 3,50 |
| **5** | 1,65 | 1,63 | 2,41 | 1,96 |
| **10** | 1,26 | 1,25 | 1,69 | 1,43 |
| **20** | 1,08 | 1,07 | 1,31 | 1,17 |
| **50** | 1,00 | 1,00 | 1,09 | 1,04 |
| **100** | 1,00 | 1,00 | 1,00 | 1,00 |
| **200** | 1,03 | 1,03 | 0,97 | 1,00 |
| **300** | 1,05 | 1,07 | 0,97 | 1,01 |
| **500** | 1,10 | 1,13 | 0,97 | 1,01 |
| **1000** | 1,21 | 1,26 | 0,95 | 1,01 |

| T (MeV) | X94 (10nm) | Xcom (10nm) | New Model (Logistic) (10nm) | New Model (Erlang) (10nm) |
|---|---|---|---|---|
| **1** | 1,50 | 1,49 | 2,95 | 2,26 |
| **2** | 1,21 | 1,20 | 2,09 | 1,65 |
| **5** | 1,03 | 1,03 | 1,50 | 1,25 |
| **10** | 0,99 | 0,99 | 1,26 | 1,11 |
| **20** | 0,98 | 0,98 | 1,14 | 1,05 |
| **50** | 0,99 | 0,99 | 1,04 | 1,01 |

| | | | | |
|---|---|---|---|---|
| **100** | 1,00 | 1,00 | 1,00 | 1,00 |
| **200** | 0,99 | 0,99 | 0,98 | 1,00 |
| **300** | 0,97 | 0,98 | 0,97 | 1,00 |
| **500** | 0,93 | 0,93 | 0,96 | 1,00 |
| **1000** | 0,84 | 0,85 | 0,95 | 1,00 |